

High Temperature Electron-Phonon and Magnon-Phonon Interactions

Thesis by
Fred Chae-Reem Yang

In Partial Fulfillment of the Requirements for the
Degree of
Doctor of Philosophy

The logo for the California Institute of Technology (Caltech), featuring the word "Caltech" in a bold, orange, sans-serif font.

CALIFORNIA INSTITUTE OF TECHNOLOGY
Pasadena, California

2019
Defended March 25, 2019

© 2019

Fred Chae-Reem Yang
ORCID: 0000-0002-5615-5170

All rights reserved

To my loving parents.

ACKNOWLEDGEMENTS

My time at Caltech has been a difficult yet satisfying period of professional and personal growth. I would not have been able to make it past the obstacles and emerge a better person without the positive support I had received from many people over the course of my graduate studies.

First, I would like to express my gratitude to my advisor, Professor Brent Fultz, for giving me the opportunity to work with him over the past few years. He had allowed me to explore topics and projects that I found interesting while grounding me in reality when needed, sometimes seeing the big picture when I would be missing the forest for the trees. I appreciated his guidance and accessibility as he helped me develop into an independent scientist.

I would like to thank the members of my thesis committee, Professors Austin Minnich, Keith Schwab, and Marco Bernardi, for their guidance and support. I look forward to thoughtful discussions yet to come.

I would like to thank the former and current members of the Fultz group. I have had the great pleasure of collaborating with Jorge Muñoz. His mentorship helped me navigate the start of my graduate studies, and I appreciated his many research insights and his career advice. I owe my heartfelt thanks to Matthew Lucas for his help and insight with the FeTi project and for his expertise that allowed the Pd₃Fe beamtime experiment to come into fruition. Olle Hellman allowed me to make the jump into computational materials science, helping me tackle research problems I would not have been able to explore otherwise. I appreciated his patience as he answered my many questions. I have learned a lot about neutron scattering and running experiments from Hillary Smith, and it was always an immense pleasure to work with her. I want to give her my heartfelt thanks for always providing assistance with my experiments without any sense of hesitation.

I have enjoyed going to beamtime experiments with Claire Saunders, Nick Weadock, Jane Herriman, and my officemates Dennis Kim and Yang Shen. I have enjoyed our conversations and learning from you all. I want to extend my thanks to group members Channing, Jiao, Tian, Lisa, Sally, Hongjin, Heng, Max, Bryce, Peter, Camille, Stefan, and Cullen and beamtime collaborators Chen, Andrew, Tabitha, Sarah, and Xiao. Everyone I met in the group helped motivate me to always better myself.

This research would not have been possible without the generous support from the Capital-DOE Alliance Center (CDAC) and the dedication of Dr. Russell Hemley and Dr. Steve Gramsch. I would also like to thank the staff scientists I worked with, including Yuming Xiao and Paul Chow at Argonne National Laboratory; Doug Abernathy and Matt Stone at Oak Ridge National Laboratory; and Nick Butch, Terry Udovic, and Juscelino Leao at the NIST Center for Neutron Research.

I want to thank many people outside of the group. This would include everyone I had met in my class and the APhMS programs (special thanks to Stephen for our collaborations on our problem sets and for his research insights), the Steuben house, people I had met from our graduate student orientation, the Global Troopers softball team, and several Caltech staff who have always gone the extra mile to provide assistance and make sure I was welcome at Caltech.

I want to thank a few of my off-campus friends who have kept in touch with me after Berkeley. Dara helped me stay sane throughout the past few years and provided crucial career advice. Jeremy also kept me sane, provided alternate perspectives that I needed, and helped me explore LA and its culture when I would have otherwise been stuck in Pasadena.

Finally, I want to give special thanks to my parents. I would not have made it this far without their unconditional love. My mother Anna has been my rock, giving me encouragement and emotional support all throughout these years. I want to give special thanks to my father Dr. Woo Sun Yang for being my biggest inspiration for going into science, and for always taking the time out of his busy schedule to fuel my interest in research. I hope you will be glad that there may soon be another Ph.D. in the family.

ABSTRACT

Computational materials discovery and design has emerged in order to meet the surge in demand for new materials for applications ranging from clean alternative energy to human welfare. This acceleration of materials discovery is exhilarating, but the applications of new advanced materials can be limited by their thermodynamic stability. Accurate calculations of the Gibbs free energy, a measure of thermodynamic stability, require a deep understanding of atomic vibrations, a main source of entropy in materials. This deep understanding of atomic vibrations requires us to treat phonons (quantized lattice vibrations) beyond the harmonic model by considering their interactions with various excitations. In this thesis, I present the effects of high temperature interactions of phonons with electrons and magnetic excitations on the thermodynamics of FeTi, vanadium, and Pd₃Fe.

A combination of *ab initio* calculations, inelastic neutron scattering (INS), and nuclear resonant inelastic x-ray scattering (NRIXS) showed an anomalous thermal softening of the M_5^- phonon mode in B2-ordered FeTi and a thermal stiffening of the longitudinal acoustic N phonon mode in body-centered-cubic vanadium. Computational investigations involving electronic band unfolding were performed to identify the nesting features on Fermi surfaces crucial to high temperature electron-phonon interactions in FeTi and vanadium. These investigations showed that the Fermi surface of FeTi undergoes a novel thermally driven electronic topological transition (ETT), in which new features of the Fermi surface arise at elevated temperatures. This ETT was also observed in vanadium, but the effects were overtaken by the thermal smearing of the Fermi surface that decreased the rate of electron-phonon scattering.

Iron phonon partial densities of states of Pd₃Fe were measured with NRIXS from room temperature through the Curie transition at 500 K. The experimental results were compared to *ab initio* spin-polarized calculations that modeled the finite-temperature thermodynamic properties of Pd₃Fe with magnetic special quasirandom structures (SQSs) of magnetic moments. The scattering measurements and first-principles calculations showed that the iron partial vibrational entropy is close to what is predicted by the quasiharmonic approximation owing to a cancellation of effects: phonon-phonon and magnon-phonon interactions approximately cancel a ferromagnetic optical phonon stiffening.

PUBLISHED CONTENT AND CONTRIBUTIONS

- [1] F. C. Yang, J. A. Muñoz, O. Hellman, L. Mauger, M. S. Lucas, S. J. Tracy, M. B. Stone, D. L. Abernathy, Y. Xiao, and B. Fultz. “Thermally Driven Electronic Topological Transition in FeTi”. *Physical Review Letters* **117**, 076402 (2016). DOI: 10.1103/PhysRevLett.117.076402.
F.C.Y analyzed the data, performed the computational analysis, and conducted the writing of the manuscript.
- [2] H. L. Smith, C. W. Li, A. Hoff, G. R. Garrett, D. S. Kim, F. C. Yang, M. S. Lucas, T. Swan-Wood, J. Y. Y. Lin, M. B. Stone, D. L. Abernathy, M. D. Demetriou, and B. Fultz. “Separating the configurational and vibrational entropy contributions in metallic glasses”. *Nature Physics* **13**, 900 (2017). DOI: 10.1038/nphys4142.
F.C.Y participated in the experiment and commented on the manuscript.
- [3] F. C. Yang, O. Hellman, M. S. Lucas, H. L. Smith, C. N. Saunders, Y. Xiao, P. Chow, and B. Fultz. “Temperature dependence of phonons in Pd₃Fe through the Curie temperature”. *Physical Review B* **98**, 024301 (2018). DOI: 10.1103/PhysRevB.98.024301.
F.C.Y conceptualized the project, prepared the sample and conducted the experiment, reduced and analyzed the data, performed all calculations, and conducted the writing of the manuscript.
- [4] H. L. Smith, Y. Shen, D. S. Kim, F. C. Yang, C. P. Adams, C. W. Li, D. L. Abernathy, M. B. Stone, and B. Fultz. “Temperature dependence of phonons in FeGe₂”. *Physical Review Materials* **2**, 103602 (2018). DOI: 10.1103/PhysRevMaterials.2.103602.
F.C.Y performed one of the measurements, reduced the data, and commented on the manuscript.
- [5] F. C. Yang, O. Hellman, and B. Fultz. “Thermal Evolution of Electron-Phonon Interactions in Vanadium”. *In Preparation*.
F.C.Y conceptualized the project, performed all calculations, and conducted the writing of the manuscript.

TABLE OF CONTENTS

Acknowledgements	iv
Abstract	vi
Published Content and Contributions	vii
Table of Contents	viii
List of Illustrations	ix
List of Tables	xvi
Chapter I: Introduction	1
1.1 Overview	1
1.2 Harmonic Lattice Dynamics	2
1.3 Electron-Phonon Interactions	6
1.4 Magnon-Phonon Interactions	9
Chapter II: Thermally Driven Electronic Topological Transition in FeTi . . .	12
2.1 Main Text	12
2.2 Supporting Information	19
Chapter III: Thermal Evolution of Electron-Phonon Interactions in Vanadium	27
3.1 Introduction	27
3.2 Computation	28
3.3 Results	33
3.4 Discussion	38
3.5 Conclusions	46
Chapter IV: Temperature Dependence of Phonons in Pd ₃ Fe Through the Curie	
Temperature	47
4.1 Introduction	47
4.2 Methods	48
4.3 Results	53
4.4 Discussion	62
4.5 Conclusions	65
4.6 Supporting Information	67
Chapter V: Concluding Remarks and Future Directions	75
5.1 Electron-Phonon Interactions	75
5.2 Magnon-Phonon Interactions	77
Appendix A: Harmonic Model	80
A.1 Einstein and Debye Models	80
A.2 Born von Kármán Model	80
Bibliography	82

LIST OF ILLUSTRATIONS

<i>Number</i>	<i>Page</i>
1.1 (Left) The harmonic S_h , quasiharmonic S_{qh} , and measured vibrational entropy S_{vib} of α -iron compared with the total entropy from the SGTE database [6]. Vibrational entropies calculated and measured by Mauger <i>et al.</i> [7]. (Right) The harmonic, quasiharmonic, and measured vibrational entropy of vanadium [10] compared with the total entropy from the SGTE database [6] and laser-flash calorimetry measurements by Takahashi <i>et al.</i> [9].	4
1.2 The effects of temperature (from bottom to top) on phonons (left) and electrons (right), and the effects of the adiabatic electron-phonon interaction (EPI) when phonons alter the electronic band structure in the presence of electron excitations. Also shown are illustrations of the quasiharmonic approximation and phonon-phonon interactions (PPI). Increasing width of light shading indicates increasing thermal energy spreads. From Ref. [4].	5
1.3 (Left) Phonon densities of states (DOS) of vanadium from 10 to 1273 K, as measured by Delaire <i>et al.</i> [10]. (Right) Electronic DOS (eDOS) of vanadium at 0 and 1000 K. The 0 K eDOS was calculated with a static density functional theory (DFT) calculation. The 1000 K eDOS was calculated from a convolution of the 0 K eDOS with a Lorentzian with a full-width-at-half-maximum (FWHM) of 380 meV [10].	8
1.4 Trends in the temperature dependence of phonon energies ω on adiabatic electron-phonon interactions for different electronic densities of states $N(E)$, as summarized by Delaire, <i>et al.</i> [26]. The dotted line represents quasiharmonic (QH) behavior.	9

- 1.5 (Left) The nonharmonic vibrational entropy ΔS_{nh} from phonon DOS spectra measured by Mauger *et al.* compared to the magnetization of bcc Fe [29] and the magnetic vibrational entropy S_{mag} , obtained by subtracting S_{vib} and S_{el} [32] from the SGTE total entropy [6]. From Ref. [7]. (Right) Average Fe phonon energies of cementite from NRIXS measurements (points). The dashed lines are quasiharmonic energies from experiment (“QH γ_T Model”) and computation (“QH DFT”). From Ref. [31]. 10
- 2.1 Calculated FeTi phonon dispersions at temperatures from 300 to 1500 K. Also shown are phonon DOS curves for the motions of all atoms (total) and iron atoms (Fe partial). 13
- 2.2 Temperature dependence of the M_5^- phonon energy calculated from TDEP (squares). The colors of the squares are identical to those shown in Fig. 2.1. The green and blue markers are mean phonon energies obtained from Lorentzian fits to the Fe NRIXS DOS and the INS DOS, respectively. The dashed line is the thermal softening of the M_5^- phonon from quasiharmonicity alone. The inset shows the agreement in the slopes of the experimental and computational phonon energies without quasiharmonic contributions. For convenience in showing the slopes, the NRIXS data were offset by -0.76 meV and the INS by -0.35 meV. 14
- 2.3 Experimental FeTi phonon DOS curves. The neutron-weighted DOS curves were obtained from INS measurements and the Fe partial DOS curves from NRIXS measurements. Error bars are from counting statistics. 15
- 2.4 (a)-(c) Approximated finite-temperature Fermi surfaces in the Brillouin zone. The dark blue surfaces are the unshifted 0 K Fermi surfaces, and the lighter blue surfaces are at energies shifted from the Fermi energy by factors of $1.8 k_B T$. (d)-(f) Finite-temperature band structures from supercell AIMD calculations, produced by BandUP. The Fermi surface and band structure at 523 K resemble those at 0 K without any broadening. 16

2.5	Histogram of spanning vectors that couple the new states at one of the R symmetry points with the rest of the Fermi surface along the $[\xi\xi0]$ and $[\frac{1}{2}\xi0]$ directions at 1035 K, displayed together with the changes in energies of the TA and LA branches from 300 K to 1035 K along the same directions.	17
2.6	A view of the displacement pattern of the M_5^- phonon, in which Fe (orange) and Ti (blue) atoms move along the $[1\bar{1}0]$ directions. The dashed lines are the 1nn Fe–Ti interactions, and the solid lines are the 2nn Fe–Fe interactions.	18
2.7	Neutron scattering function $S(Q, E)$ spectrum of FeTi at 300 K. . . .	20
2.8	Phonon DOS curves for FeTi at elevated temperatures. The neutron-weighted DOS curves were obtained from INS measurements and the Fe partial DOS curves from NRIXS measurements. The two data sets were combined to obtain neutron-weight-corrected DOS curves and Ti partial DOS curves. Error bars from counting statistics.	21
2.9	FeTi phonon dispersions calculated in the quasiharmonic model. . . .	23
2.10	Calculated 0 K electron-phonon linewidths displayed over the 0 K FeTi phonon dispersion.	24
2.11	Electronic DOS for FeTi from 0 to 1035 K. Obtained from AIMD and static DFT calculations.	24
2.12	FeTi phonon dispersions calculated after individually exchanging the (a) Fe–Fe 2nn longitudinal and (b) Fe–Ti 1nn transverse force constants at 300 K with those at 1500 K.	26
3.1	(a) The phonon DOS curves of vanadium calculated with the s-TDEP method at temperatures from 0 (dark purple) to 1650 K (orange). (b) Average phonon energies of vanadium calculated with the s-TDEP method (identical colors to those shown in (a)), shown together with average phonon energies from inelastic neutron scattering measurements (Refs. [10, 84, 98]). The dashed red curve corresponds to quasiharmonic (QH) behavior as calculated from first-principles. . . .	34
3.2	The 300 K spectral function calculated with s-TDEP along the high-symmetry directions, plotted together with measurements from thermal diffuse x-ray scattering (crosses) [116] and inelastic x-ray scattering (dots) [117].	35

3.3	Phonon dispersion curves of vanadium calculated with the s-TDEP method at temperatures from 0 (dark purple) to 1650 K (orange). Vector coordinates are written in simple cubic lattice coordinates.	35
3.4	Unfolded electronic bands at 1100 K, compared with 0 K electronic bands in dark red. The Fermi level is represented as a spread in energies.	36
3.5	The {100} cross sections of the Fermi surface of vanadium at (a) 0 K and (b) 1100 K (cross section indices are expressed in simple cubic coordinates).	38
3.6	(Top) 0 K electron-phonon coupling strengths of phonon modes calculated with Quantum ESPRESSO displayed over the 0 K vanadium phonon dispersion calculated with s-TDEP. (Bottom) Autocorrelation of the Fermi surface at 0 and 1100 K.	39
3.7	{100} cross sections of the Fermi surface nesting strengths of vanadium for the transverse phonon mode at $\mathbf{q} = [0.24, 0, 0]$ at (a) 0 K and (b) 1100 K, the longitudinal N phonon mode at (c) 0 K and (d) 1100 K, and the H phonon mode at (e) 0 K and (f) 1100 K. Sample $[0.24, 0, 0]$ and $[0.5, 0.5, 0]$ spanning vectors are shown in (a) and (c).	42
3.8	The electrical resistivities of bcc transition metals relative to their 300 K values. The plotted data are from measurements on high-purity samples.	44
4.1	(a) Schematic of supercells with Fe atoms (dark blue) stochastically displaced from their ideal positions (light blue) in the 0 K ferromagnetic calculations, where the magnetic moments (red arrows) are aligned in the same direction. (b) Supercells with randomly oriented magnetic moments and stochastically displaced Fe atoms in the 800 K paramagnetic calculations. Each set of randomly oriented magnetic moments is a magnetic special quasirandom structure (SQS). Pd atoms are not shown for this illustration.	52
4.2	The ^{57}Fe nuclear forward scattering spectra from $L1_2$ -ordered Pd_3Fe at several temperatures. The fits (black curves) overlay experimental data (points). The spectra are displayed using a log scale, and offset for clarity.	54

4.3	The magnetization curve of Pd ₃ Fe obtained from an empirical fit of a magnetic shape function [172] to hyperfine magnetic fields obtained from the NFS spectra in this study (green) and Mössbauer data from a study by Longworth [154] (orange). The shaded region indicates the temperature range where Pd ₃ Fe exhibits ferromagnetic order. . . .	55
4.4	The normalized ⁵⁷ Fe pDOS extracted from NRIXS measurements at various temperatures. The spectra from measurements above 298 K are offset and compared with the 298 K pDOS (black curve). Error bars are from counting statistics.	56
4.5	Average energies of the Fe pDOS from NRIXS measurements (blue points) plotted with the average Fe phonon energies from the Grüneisen parameter model (green line) and the QH DFT model (red line). . . .	57
4.6	Total, Pd partial, and Fe partial phonon DOS curves of Pd ₃ Fe calculated with the s-TDEP method from 0 to 800 K.	58
4.7	(a) NRIXS ⁵⁷ Fe pDOS curves compared at 298 and 786 K. (b) s-TDEP Fe pDOS curves compared at 300 and 800 K. Phonon difference spectra are shown for both NRIXS and s-TDEP.	59
4.8	(a) The Fe partial vibrational entropy from the NRIXS measurements compared with the entropy from the Grüneisen parameter model (QH γ_T) and the QH DFT model. (b) The s-TDEP Fe partial vibrational entropy calculated for Pd ₃ Fe with changing magnetic order (blue), ferromagnetic order (green), and the absence of phonon-phonon interactions (orange). The red line is the entropy from the QH DFT model. The insets in (a) and (b) show the nonharmonic contributions to the vibrational entropy.	60
4.9	Calculated phonon dispersions for the ferromagnetic and paramagnetic states at 800 K. The dispersions displayed do not include effects from phonon-phonon interactions. Displacement patterns are shown for two high-energy optical phonon modes that soften with decreasing magnetization. The orange and green spheres represent Fe and Pd atoms, respectively. The Fe partial phonon DOS curves of Pd ₃ Fe calculated with the s-TDEP method for the ferromagnetic and paramagnetic states at 800 K are shown in the lower left.	62

4.10	Pd ₃ Fe spectral functions (logarithmic intensity scale) calculated with s-TDEP along the high-symmetry directions at 0, 300, and 800 K. Measurements of the 80 K phonon dispersion by inelastic neutron scattering [176] are shown on top of the 0 K spectral function.	64
4.11	Pd ₃ Fe phonon lineshapes at the X high symmetry point at 800 K. The orange and green peaks are the optical modes that shift with changing magnetic order. The black dashed peak is the lineshape of the optical mode after the Pd–Pd 1NN cubic force constant is set to zero.	64
4.12	X-ray diffraction patterns of Pd ₃ ⁵⁷ Fe (“Ordered-II”) collected on a Cu K α laboratory diffractometer. Measurements were performed on the sample after the heat treatment (“Pre-NRIXS”) and after the NRIXS measurements (“Post-NRIXS”). The labeled peaks include both fundamental and superlattice peaks. The intensity is displayed in a logarithmic scale.	67
4.13	(Top) Room temperature Mössbauer spectrum of the annealed Pd ₃ ⁵⁷ Fe foil sample before the NRIXS experiment (Ordered-II). (Bottom) Pd ₃ ⁵⁷ Fe Mössbauer spectra for the “Ordered-I” state, “Ordered-II” state, and after the NRIXS experiment.	69
4.14	Two-dimensional synchrotron diffraction patterns of Pd ₃ Fe recorded on a CCD detector plate at (a) 298 K and (b) 786 K. (c) One-dimensional synchrotron x-ray diffraction patterns of Pd ₃ ⁵⁷ Fe from 298 to 786 K. The black dashed lines are the locations of the 298 K diffraction peaks. The dips in intensity for 627 and 786 K are where extraneous diffraction peaks from the aluminum foil were masked.	70
4.15	(Left) Raw NRIXS scattering spectra showing ⁵⁷ Fe vibrational excitations in Pd ₃ ⁵⁷ Fe as a function of scattering energy. Spectra are collected over a range of temperatures. (Right) The elastic line of the raw scattering spectrum of ⁵⁷ Fe at room temperature, used as the instrument resolution function for the NRIXS measurements.	72
4.16	The multi-phonon components of the NRIXS spectra of Pd ₃ ⁵⁷ Fe at (left) 298 K and (right) 786 K.	72
4.17	Lamb-Mössbauer factors obtained from NRIXS (blue squares) and NFS (green triangles).	73

4.18	The room temperature ^{57}Fe pDOS of the $\text{Pd}_3^{57}\text{Fe}$ sample measured in this study (purple) compared with prior measurements of the room temperature ^{57}Fe pDOS of ordered $\text{Pd}_3^{57}\text{Fe}$ (black) and the disordered fcc alloy $\text{Pd}_{0.75}^{57}\text{Fe}_{0.25}$ (red).	74
5.1	The frequency shifts and linewidth of the E_g 187 cm^{-1} Raman line versus temperature in FeF_3 , measured by Shepherd [197].	78

LIST OF TABLES

<i>Number</i>	<i>Page</i>
3.1 Electron-phonon interaction parameters and superconducting transition temperatures of nonmagnetic bcc transition metals.	44
4.1 Hyperfine fields H and change in the hyperfine field ΔH in the $\text{Pd}_3^{57}\text{Fe}$ sample at different stages of this study, shown together with measurements performed by Longworth [154]. For the $\text{Pd}_3^{57}\text{Fe}$ sample, the hyperfine field for “Ordered-II” is treated as a reference for ΔH . For the measurements performed by Longworth, the hyperfine field for the ordered sample is treated as a reference for ΔH	68
4.2 The Fe partial vibrational heat capacity calculated from the integration of the ^{57}Fe phonon DOS.	72
4.3 The vibrational kinetic energy calculated from the integration of the ^{57}Fe phonon DOS.	73
4.4 The mean force constant calculated from the integration of the ^{57}Fe phonon DOS.	74

Chapter 1

INTRODUCTION

“A theory is the more impressive the greater the simplicity of its premises, the more different kinds of things it relates, and the more extended its area of applicability. Therefore the deep impression that classical thermodynamics made upon me. It is the only physical theory of universal content which I am convinced will never be overthrown, within the framework of applicability of its basic concepts.”

— Albert Einstein

1.1 Overview

The traditional development of materials for industrial applications typically takes decades, from initial discovery to market. The demand for new advanced materials that address pertinent challenges including clean energy, national security, and human welfare has only grown stronger over time. In response, recent research efforts and initiatives including the Materials Genome Initiative have aimed to accelerate the process of discovering, manufacturing, and mass producing new materials [1].

High performance computing (HPC) has become a major part of this push towards accelerated materials discovery. Computational materials discovery would allow us to predict candidate materials given desired macroscopic properties, minimizing the time and cost of experimental discovery. Recent developments to computational materials discovery have been made through high-throughput computing, in which large volumes of *ab initio* calculations are combined with data mining of large databases using supercomputer architectures [2]. With the explosion of new materials discoveries from these new methods, we are living in exciting times.

Now we must, however, make sure to stay grounded in reality. These predictive tools must be able to predict the existence of existing materials, and hypothetical materials must be able to be developed under realistic conditions. In order to carry out reality checks on developments in this new scientific field, we turn to the older but fundamental branch of physics, thermodynamics. In particular, we turn to the Gibbs free energy, which allows us to assess the thermodynamic stability of phases

of materials:

$$G = U + PV - TS. \quad (1.1)$$

The stable phase is the one that minimizes the free energy given conditions including temperature, pressure, mechanical stress, and magnetism [3]. Calculating and understanding the free energy of a phase and of competing phases provides essential information on material stability under different operational temperatures, an important consideration concerning the processing and performance of the material in technological service.

The entropic contribution to the free energy of solids, $-TS$, changes rapidly with temperature. The entropy S enumerates the way heat is stored in a material within the many degrees of freedom of the material. For ordered crystalline solids, the vibrations of atoms make up the largest entropic contribution. With increasing temperature, we see increased populations of *phonons*, quanta of lattice vibrations, and greater vibrational excursions of atoms. The *vibrational entropy* S_{vib} increases with temperature because the material explores a larger volume in the phase space of position and momentum [4]. Understanding the vibrational entropy and the lattice dynamics of a material is crucial for accurately calculating the temperature-dependent behavior of its free energy.

1.2 Harmonic Lattice Dynamics

We can begin our discussion of lattice vibrations by building off of the harmonic model, in which lattice vibrations are calculated from a Taylor expansion of the potential energy of the crystal up to the second order of atomic displacement. In this model, normal modes do not transfer energy to other normal modes, such that phonons with energies ε_i may be considered as independent harmonic oscillators that persist forever. This treatment allows us to write the partition function of a harmonic solid with N atoms and $3N$ independent oscillators as the product of individual oscillator partition functions:

$$Z_N = \prod_i^{3N} Z_i = \prod_i^{3N} \frac{e^{-\beta\varepsilon_i/2}}{1 - e^{-\beta\varepsilon_i}}, \quad (1.2)$$

where $\beta \equiv (k_B T)^{-1}$. From this partition function, we can calculate the vibrational entropy by differentiating the phonon free energy $F_{\text{vib}} = -k_B T \ln Z_N$:

$$S_{\text{vib}} = - \left(\frac{\partial F_{\text{vib}}}{\partial T} \right)_V = k_B \sum_i^{3N} \left[-\ln \left(1 - e^{-\beta \varepsilon_i} \right) + \frac{\beta \varepsilon_i}{e^{\beta \varepsilon_i} - 1} \right]. \quad (1.3)$$

From the vibrational entropy, we can calculate thermodynamic quantities such as the heat capacity from lattice vibrations:

$$C_V(T) = T \left(\frac{\partial S}{\partial T} \right)_V = k_B \sum_i^{3N} (\beta \varepsilon_i)^2 \frac{e^{\beta \varepsilon_i}}{(e^{\beta \varepsilon_i} - 1)^2}. \quad (1.4)$$

The mean occupation of these bosonic oscillators can be described with the Planck distribution

$$n_T(\varepsilon_i) = \frac{1}{e^{\beta \varepsilon_i} - 1}, \quad (1.5)$$

with which we can rewrite Eq. 1.3 as

$$S_{\text{vib}} = k_B \sum_i^{3N} [(n_T(\varepsilon_i) + 1) \ln(n_T(\varepsilon_i) + 1) - n_T(\varepsilon_i) \ln(n_T(\varepsilon_i))]. \quad (1.6)$$

We often work with a phonon density of states (DOS) $g(\varepsilon)$, a distribution of phonon modes with respect to energy. Measurements or calculations of phonon frequencies allow us to calculate the vibrational entropy and thermodynamic quantities:

$$S_{\text{vib}} = 3N k_B \int g(\varepsilon) [(n_T(\varepsilon) + 1) \ln(n_T(\varepsilon) + 1) - n_T(\varepsilon) \ln(n_T(\varepsilon))] d\varepsilon. \quad (1.7)$$

In this harmonic approximation of the vibrational entropy, the only temperature dependence is from the Planck distribution $n_T(\varepsilon)$. Phonon frequencies and the DOS can be calculated following the Einstein, Debye, or Born von Kármán model [5], as discussed in Appendix A.

The harmonic model often explains physical phenomena at low temperatures. Fig. 1.1 shows that the harmonic vibrational entropy S_h of α -iron deviates from both the total entropy [6] and vibrational entropy measured with inelastic x-ray scattering [7] at high temperatures. We can rectify some shortcomings of the harmonic model with the quasiharmonic (QH) model, which introduces effects of thermal expansion. Phonons are still treated as independent harmonic oscillators, but the frequencies are scaled by the change in volume with increasing temperature:

$$\frac{\Delta \omega}{\omega} = -\gamma \frac{\Delta V}{V}, \quad (1.8)$$

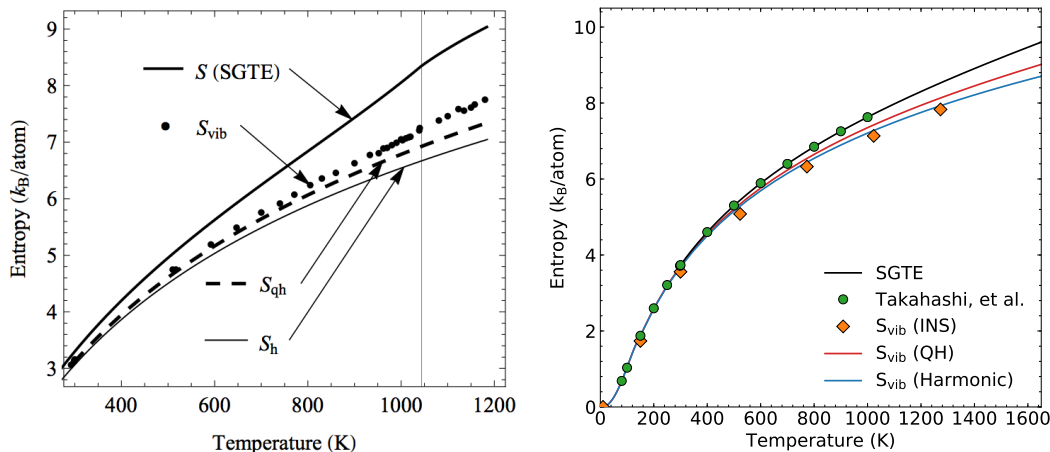


Figure 1.1: (Left) The harmonic S_h , quasi-harmonic S_{qh} , and measured vibrational entropy S_{vib} of α -iron compared with the total entropy from the SGTE database [6]. Vibrational entropies calculated and measured by Mauger *et al.* [7]. (Right) The harmonic, quasi-harmonic, and measured vibrational entropy of vanadium [10] compared with the total entropy from the SGTE database [6] and laser-flash calorimetry measurements by Takahashi *et al.* [9].

where the proportionality constant γ is the Grüneisen parameter [8]. Using the expression for the vibrational entropy (Eq. 1.6), its temperature dependence is introduced from both the Planck distribution $n_T(\varepsilon)$ and how the phonon DOS $g_T(\varepsilon)$ is scaled with Eq. 1.8. Fig. 1.1 shows that the QH model improves on the harmonic model, but still falls short of the measured vibrational entropy. Fig. 1.1 also shows us how the vibrational entropy from the QH model deviates from the total entropy of vanadium [6, 9] and fails to model the vibrational entropy of vanadium measured with inelastic neutron scattering [10]. We note for Fig. 1.1 that the difference between the total and vibrational entropies of α -Fe is the sum of the electronic and magnetic entropies, and the difference between the total and vibrational entropies of vanadium is the electronic entropy.

We see that even the QH approximation is too simple for modeling the behavior of phonons in real crystals. The treatment of phonons as independent harmonic oscillators fails to explain macroscopic phenomena like thermal expansion or finite thermal conductivities. More realistic models of phonon behavior must take into account the previously neglected higher order terms in atomic displacements of the potential energy. With these additional terms, we can no longer treat phonons as independent oscillators. We need to take into account *phonon interactions* to make accurate predictions of the free energy of a material. The nonharmonic contributions to the vibrational entropy may appear to be minor numerical corrections. These

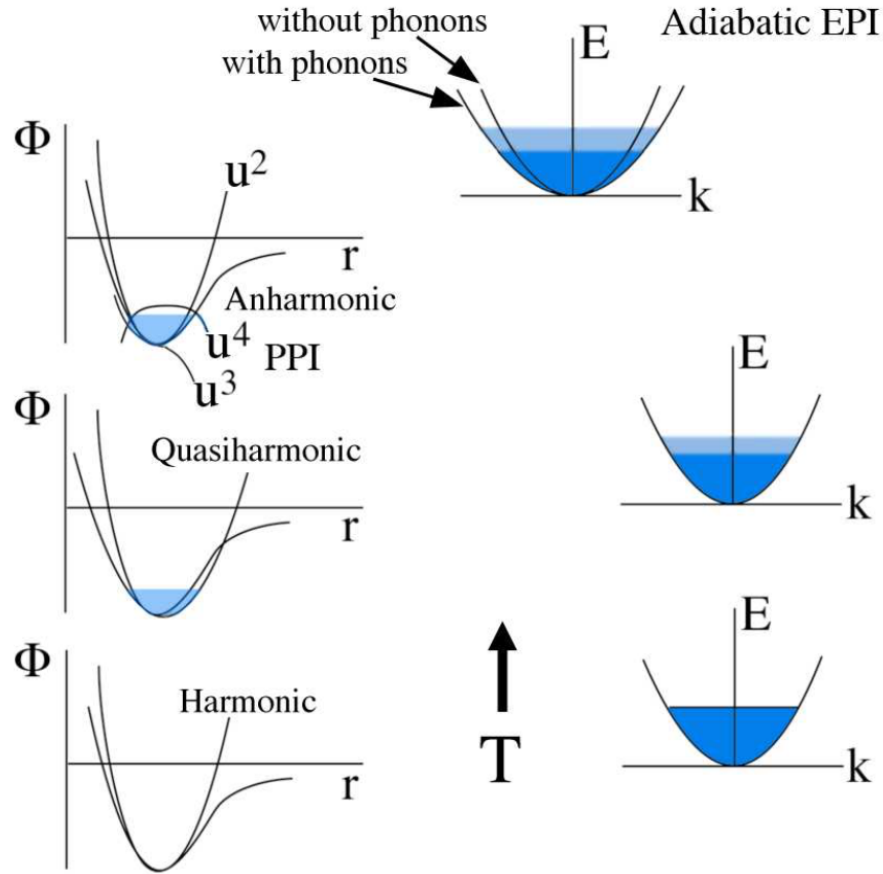


Figure 1.2: The effects of temperature (from bottom to top) on phonons (left) and electrons (right), and the effects of the adiabatic electron-phonon interaction (EPI) when phonons alter the electronic band structure in the presence of electron excitations. Also shown are illustrations of the quasiharmonic approximation and phonon-phonon interactions (PPI). Increasing width of light shading indicates increasing thermal energy spreads. From Ref. [4].

seemingly minor numerical corrections, however, can correct for when the QH model incorrectly predicts phase instabilities [7, 11–14].

The anharmonic phonon-phonon interaction (PPI) underlies phenomena like the thermal expansion or finite thermal conductivities. Electron-phonon interactions (EPIs) are responsible for Cooper pairing in conventional superconductors and play a role in the temperature dependence of the electrical resistivity in metals and the carrier mobility in semiconductors. Phonons can also interact with magnetic excitations, impacting the thermodynamics of magnetic systems, such as the phase transitions of the Ni_2MnGa magnetic shape memory system [12]. From experimental measurements of phonons in materials at high temperatures, we observe that these phonon interactions shift and broaden their energies (Fig. 1.2).

We are interested in expanding our understanding of these phonon interactions, particularly at high temperatures. While we study the effects of phonon-phonon interactions in this thesis, the effect of anharmonicity on thermodynamic properties is not the focal point. The remainder of this introductory chapter provides overviews of the electron-phonon and magnon-phonon interactions, which follows the organization of this thesis.

1.3 Electron-Phonon Interactions

When a phonon is excited, atoms are moved from their equilibrium positions. The effective electrostatic potential acting on an electron is changed by this atomic displacement. As a result, this electron is likely to be scattered. This scattering process can alter the electronic screening of the atom if the phonon wavelength is comparable to the electron screening length [15].

This interaction at low temperatures has been mathematically modeled through perturbation theory. As detailed by Ziman [15] and Grimvall [16], an important component of perturbation theory is the electron-phonon matrix element:

$$g_{mn}^{\nu}(\mathbf{k}, \mathbf{q}) = \sqrt{\frac{\hbar}{2\omega_{\mathbf{q}\nu}}} \sum_{\kappa\alpha} \frac{e_{\mathbf{q}\nu}^{\kappa\alpha}}{\sqrt{m_{\kappa}}} \langle m\mathbf{k} + \mathbf{q} | \partial_{\mathbf{q}\kappa\alpha} V | n\mathbf{k} \rangle, \quad (1.9)$$

where m_{κ} is the nuclear mass of atom κ , $\mathbf{e}_{\mathbf{q}\nu}$ is the phonon displacement eigenvector, and $\partial_{\mathbf{q}\kappa\alpha} V$ is the variation of the electronic potential with respect to displacement of atom κ in the Cartesian direction α . This matrix element describes the interaction of the phonon mode with wavevector \mathbf{q} and polarization ν with the electronic states $|n\mathbf{k}\rangle$ and $|m\mathbf{k} + \mathbf{q}\rangle$.

The matrix element $g_{mn}^{\nu}(\mathbf{k}, \mathbf{q})$ is included in electron-phonon scattering rates. The scattering rate of phonons by electron-phonon interactions derived from either the phonon self-energy [16] or Fermi's golden rule [17, 18] is

$$\begin{aligned} \frac{1}{\tau_{\mathbf{q}\nu}} = & \frac{2\pi}{\hbar} \sum_{mn} \int \frac{d\mathbf{k}}{\Omega_{\text{BZ}}} |g_{mn}^{\nu}(\mathbf{k}, \mathbf{q})|^2 (f_{n\mathbf{k}} - f_{m\mathbf{k}+\mathbf{q}}) \\ & \times \delta(\varepsilon_m(\mathbf{k} + \mathbf{q}) - \varepsilon_n(\mathbf{k}) - \hbar\omega_{\mathbf{q}\nu}), \end{aligned} \quad (1.10)$$

where $f_{n\mathbf{k}}$ is the Fermi-Dirac distribution for electrons and $\varepsilon_n(\mathbf{k})$ is the electronic energy.

One takeaway from Eq. 1.10 is that the crystal momentum is conserved in this interaction. A phonon with wavevector \mathbf{q} interacts with two electronic states with

wavevectors \mathbf{k} and \mathbf{k}' if their wavevectors follow the condition

$$\mathbf{q} = \mathbf{k}' - \mathbf{k} - \mathbf{g}, \quad (1.11)$$

where \mathbf{g} is an arbitrary reciprocal lattice vector. A nonzero \mathbf{g} describes electron-phonon Umklapp processes, which is relevant only if the electronic structure is treated with the reduced zone scheme [15].

Another takeaway from Eq. 1.10 is that the energy is conserved in the electron-phonon interaction:

$$\varepsilon(\mathbf{k}') = \varepsilon(\mathbf{k}) \pm \hbar\omega_{\mathbf{q}\nu}, \quad (1.12)$$

where we account for both phonon absorption and creation.

The difference ($f_{n\mathbf{k}} - f_{m\mathbf{k}+\mathbf{q}}$) in Eq. 1.10 describes how an electron is scattered from an occupied state into an unoccupied state. If we also take into consideration how phonon energies are small in scale in comparison to electron energies, we see that electron-phonon interactions involve states near the Fermi surface, a map of k -points in the Brillouin zone (reciprocal space primitive cell) where the electronic energy equals the Fermi energy: $\varepsilon \equiv E - E_F = 0$.

An electron-phonon interaction involving a phonon mode $\mathbf{q}\nu$ is particularly strong if there is a high density of electronic state pairs $|n\mathbf{k}\rangle$ and $|m\mathbf{k} + \mathbf{q}\rangle$ on the Fermi surface. In other words, an electron-phonon interaction involving a phonon mode $\mathbf{q}\nu$ is strong if there are nesting features, or parallel sheets separated by one wavevector \mathbf{q} , on the Fermi surface. This causes an electronic screening that reduces the energy of the phonon mode $\mathbf{q}\nu$, causing a Kohn anomaly [19]. These strong interactions can contribute to a high superconducting transition temperature T_c [20, 21] and a high average electron-phonon coupling constant λ :

$$\lambda = \frac{N(E_F) \langle \langle |g_{mn}^\nu(\mathbf{k}, \mathbf{q})|^2 \rangle \rangle_{FS}}{m \langle \omega^2 \rangle}, \quad (1.13)$$

where $N(E_F)$ is the electronic density of states at the Fermi energy, $\langle \langle \dots \rangle \rangle_{FS}$ is the average over all possible combinations of electronic states on the Fermi surface, and $\langle \omega^2 \rangle$ is the second moment of the Éliashberg coupling function [16].

Our understanding of electron-phonon interactions up to this point in the thesis has been based on concepts from low temperatures. We cannot say for certain how well the concepts behind low temperature electron-phonon interactions translate to high temperatures, where the Fermi surface is altered by thermal excitations. The

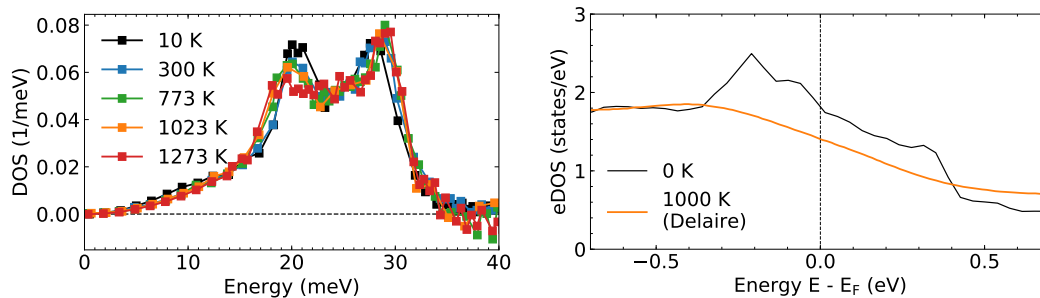


Figure 1.3: (Left) Phonon densities of states (DOS) of vanadium from 10 to 1273 K, as measured by Delaire *et al.* [10]. (Right) Electronic DOS (eDOS) of vanadium at 0 and 1000 K. The 0 K eDOS was calculated with a static density functional theory (DFT) calculation. The 1000 K eDOS was calculated from a convolution of the 0 K eDOS with a Lorentzian with a full-width-at-half-maximum (FWHM) of 380 meV [10].

thermodynamic importance of the adiabatic EPI at high temperatures had been a controversial topic [22–24].

Studies by Delaire *et al.* showed that the adiabatic EPI has significant effects on the high temperature thermodynamics of the $A15$ V_3Si and V_3Ge compounds and bcc vanadium. First-principles calculations for these materials showed that a thermal broadening smears the electronic DOS, reducing the number of electronic states at the Fermi level. A thermal phonon stiffening (increase in energy) opposed the expected softening (decrease in energy) from thermal expansion due to the decrease in the number of electrons available for screening, as illustrated in Fig. 1.3. The suppressed vibrational entropy and heat capacity were attributed to this interplay between electrons and phonons, which was observed at temperatures above 1000 K [10, 25].

The opposite effect was observed in a study by Delaire *et al.* on FeSi. The electronic DOS at the Fermi level was observed to increase with temperature as the narrow band-gap was filled in the semiconductor-to-metal transition. The anomalous thermal phonon softening was due to the increased electronic screening efficiency [26]. Fig. 1.4 summarizes the observed temperature-dependent interplay of electrons and phonons.

The aim of Chapters 2 and 3 of this thesis is to expand our knowledge of the high temperature adiabatic electron-phonon interaction. With scattering measurements and state-of-the-art computational methods, we can study the temperature-dependent lattice dynamics and the electronic structure in greater detail than what is provided

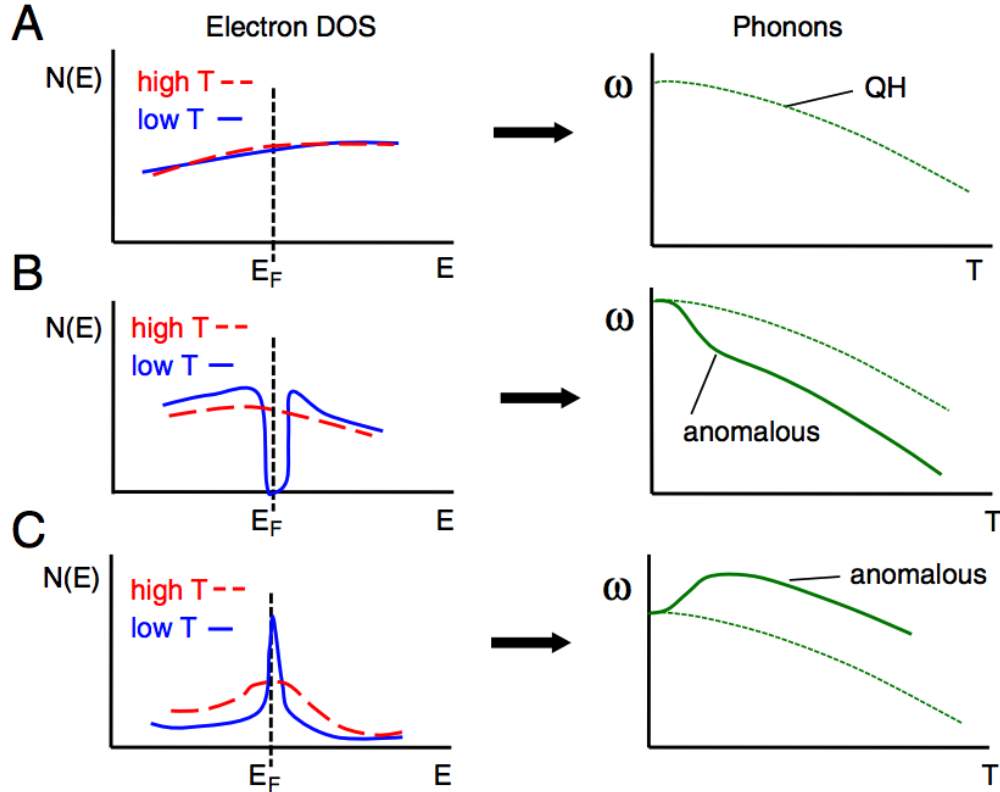


Figure 1.4: Trends in the temperature dependence of phonon energies ω on adiabatic electron-phonon interactions for different electronic densities of states $N(E)$, as summarized by Delaire, *et al.* [26]. The dotted line represents quasi-harmonic (QH) behavior.

by the phonon DOS and electronic DOS. We study the *B2*-ordered compound FeTi in Chapter 2 and revisit bcc vanadium in Chapter 3.

1.4 Magnon-Phonon Interactions

As the temperature increases through a magnetic transition temperature, the vibrations of atoms away from their equilibrium positions can modify the interactions of magnetic moments. The resulting changes in magnetic interactions between atoms can in turn alter their vibrations against each other. Magnon-phonon interactions, the exchange of energy between quanta of magnetic excitations and phonons, can be modeled with a coupling Hamiltonian \mathcal{H}_{mp} [27]:

$$\mathcal{H}_{\text{mp}} = \sum_{\mathbf{k}, \mathbf{q}} \phi_{\mathbf{k}, \mathbf{q}}^{\nu} b_{\mathbf{k}-\mathbf{q}}^{\dagger} b_{\mathbf{k}} (a_{\mathbf{q}\nu}^{\dagger} - a_{-\mathbf{q}\nu}), \quad (1.14)$$

where $a_{\mathbf{q}\nu}^{\dagger}$ and $a_{-\mathbf{q}\nu}$ are phonon creation and annihilation operators, $b_{\mathbf{k}-\mathbf{q}}^{\dagger}$ and $b_{\mathbf{k}}$ are magnon creation and annihilation operators, and $\phi_{\mathbf{k}, \mathbf{q}}^{\nu}$ is an interaction coefficient.

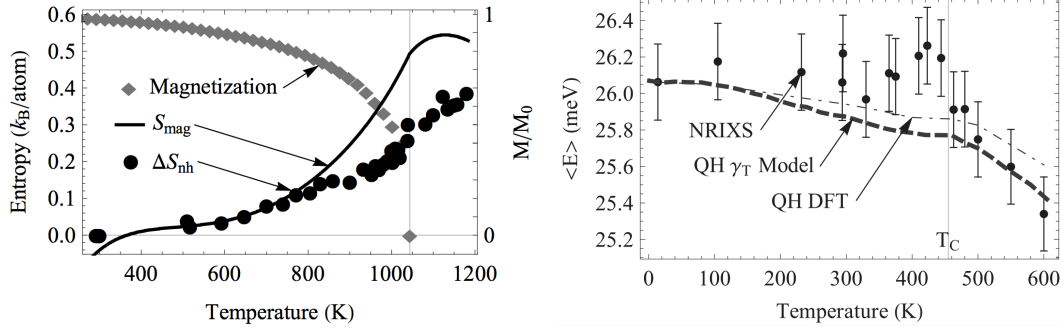


Figure 1.5: (Left) The nonharmonic vibrational entropy ΔS_{nh} from phonon DOS spectra measured by Mauger *et al.* compared to the magnetization of bcc Fe [29] and the magnetic vibrational entropy S_{mag} , obtained by subtracting S_{vib} and S_{el} [32] from the SGTE total entropy [6]. From Ref. [7]. (Right) Average Fe phonon energies of cementite from NRIXS measurements (points). The dashed lines are quasiharmonic energies from experiment (“QH γ_T Model”) and computation (“QH DFT”). From Ref. [31].

Magnon-phonon interactions can have an impact on bulk properties of materials, such as the negligible thermal expansion in Invar materials [28].

The investigation of magnon-phonon interactions at elevated temperatures in this thesis was motivated by recent studies of vibrational thermodynamics impacted by thermal magnetic disorder. Mauger *et al.* have observed through nuclear resonant inelastic x-ray scattering (NRIXS) measurements an anomalous thermal softening of phonons in bcc α -iron stronger than predicted by the QH model [7]. The strong deviation from the QH model tracked the rapid decrease in the magnetization of α -Fe [29] and the rise in magnetic entropy, as seen in the left panel of Fig. 1.5. The second-nearest-neighbor (2NN) longitudinal force constants associated with an abnormal 2NN exchange interaction [30] were observed to soften by 40 to 60% from 30 K to the Curie temperature. The sharp increase in the vibrational entropy from the magnon-phonon interaction was reported to help extend the stability of the bcc phase of iron well past its Curie temperature.

The study by Mauger *et al.* of ferromagnetic cementite Fe_3C showed more subtle impacts of the Curie transition on lattice dynamics. The average Fe phonon energies measured with NRIXS were observed to be nearly constant to the Curie temperature, as seen in the right panel of Fig. 1.5. At higher temperatures where cementite is paramagnetic, the phonon energies began to soften. A magnon-phonon interaction was observed to stiffen phonons below the Curie temperature and possibly drive changes in the elastic constants [31].

Temperature-dependent magnon-phonon interactions have also been observed in computational studies. Körmann *et al.* analyzed the impact of magnetic short-range order on the lattice vibrations above the Curie temperature of α -Fe by combining the NRIXS data provided by Mauger *et al.* with a computational framework [33]. A more recent example is the study by Stockem *et al.* that replicated the abnormal temperature dependence of the thermal conductivity above the magnetic transition temperature by dynamic coupling of spin fluctuations and lattice vibrations [34].

The aim of Chapter 4 of this thesis is to not only extend our knowledge of temperature-dependent magnon-phonon interactions, but to further develop the computational methods for predicting the lattice dynamics of materials with increasing thermal magnetic disorder. With experiments and computations, we analyze the lattice dynamics of Pd₃Fe across its Curie temperature at ambient pressure.

*Chapter 2*THERMALLY DRIVEN ELECTRONIC TOPOLOGICAL
TRANSITION IN FETI**2.1 Main Text**

An electronic topological transition (ETT), first identified by Lifshitz [35], occurs when changes to a metal cause new features to appear in the topology of the Fermi surface [36]. Structural, mechanical, and electronic properties are usually altered by an ETT, which can be induced by alloying [37–39] or pressure [40–42]. Recently a novel temperature-induced ETT has been reported to alter magnetoresistivity [43]. In this present work, we show through first-principles calculations and ancillary experiments how a thermally-driven ETT drives anomalous changes in phonon dynamics.

FeTi is a thermodynamically stable [44–46] nonmagnetic [47] intermetallic compound with a bcc-based *B2* structure and a melting point of approximately 1600 K. FeTi is of interest for its hydrogen absorption capabilities [48–50] and for its mechanical properties [51, 52]. It has been the subject of a large number of experimental and theoretical studies including inelastic neutron scattering [53, 54] and first-principles calculations [55–57]. The calculations show that FeTi has a Fermi level that lies in a pseudogap in its electronic density of states (DOS) [58–60], so thermal smearing could increase the effective density of electrons at the Fermi level.

First-principles calculations on FeTi were performed with projector augmented wave potentials [61, 62] and the generalized gradient approximation [63] of density functional theory (DFT) [64] using the VASP package [65, 66]. The electronic DOS curves at various temperatures were obtained through static calculations and constant volume ab-initio molecular dynamics (AIMD) calculations on 128-atom supercells. Convergence with respect to kinetic energy cutoffs and sampling of *k* points in the Brillouin zone was checked in all cases. The calculations show that the pseudogap is present at the Fermi level in the 0 K electronic DOS, and is filled as the number of electronic states at the Fermi level increases by 218% from 0 K to 1035 K, as shown in the Supporting Information.

Forces and atomic configurations in the AIMD simulations were used to compute interatomic force constants at different temperatures with the temperature-dependent

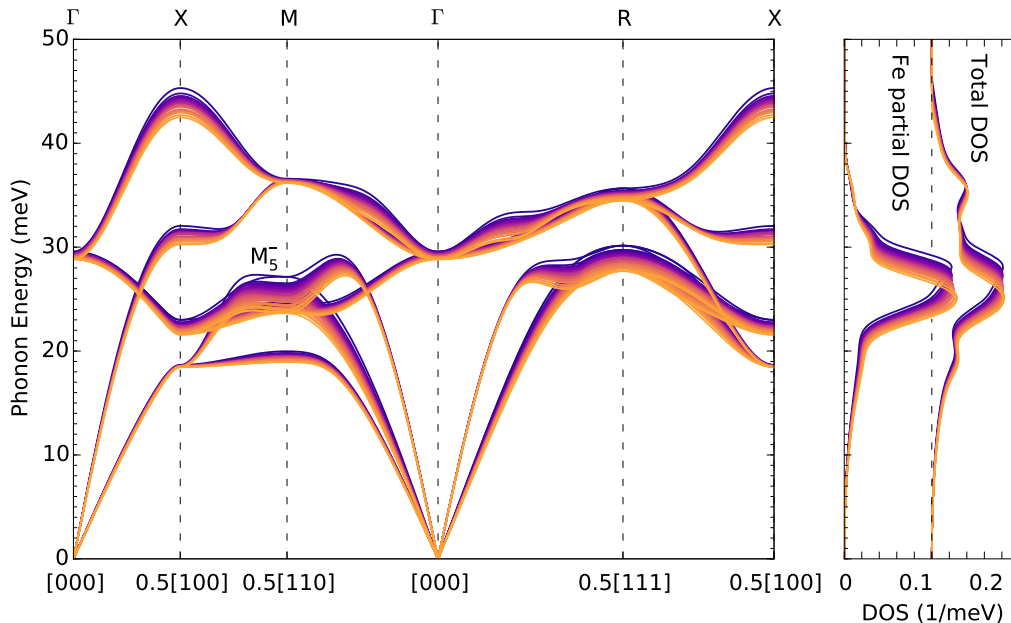


Figure 2.1: Calculated FeTi phonon dispersions at temperatures from 300 to 1500 K. Also shown are phonon DOS curves for the motions of all atoms (total) and iron atoms (Fe partial).

effective potential (TDEP) method [11, 67]. The quadratic and cubic force constants were calculated from the model Hamiltonian fit to the potential energy surface at the most probable positions of atoms in an AIMD simulation:

$$\mathcal{H} = U_0 + \sum_i \frac{\mathbf{p}_i^2}{2m_i} + \frac{1}{2!} \sum_{ij\alpha\beta} \Phi_{ij}^{\alpha\beta} u_i^\alpha u_j^\beta + \frac{1}{3!} \sum_{ijka\beta\gamma} \Phi_{ijk}^{\alpha\beta\gamma} u_i^\alpha u_j^\beta u_k^\gamma, \quad (2.1)$$

where \mathbf{p}_i is the momentum of atom i , Φ_{ij} and Φ_{ijk} are quadratic and cubic force constants, and u_i^α is the Cartesian component α of the displacement of atom i . The effects of the quartic force constants are included by renormalizing the quadratic force constants [68, 69]. The cubic force constants account for cubic anharmonicity associated with phonon-phonon interactions [70]. The thermal phonon-phonon interaction shifts $\Delta(T)$ of a phonon mode $\mathbf{q}\nu$ calculated from the third-order force constants were negligible compared to the calculated phonon thermal softening from the quadratic force constants.

The force constants from Eq. 2.1 were used to obtain phonon dispersions and phonon DOS curves at temperatures from 300 to 1500 K (Fig. 2.1). Thermal expansion causes phonons to soften with temperature, and this was accounted for by the quasiharmonic calculations presented in the Supporting Information section. The AIMD calculations were performed without thermal expansion, so Fig. 2.1

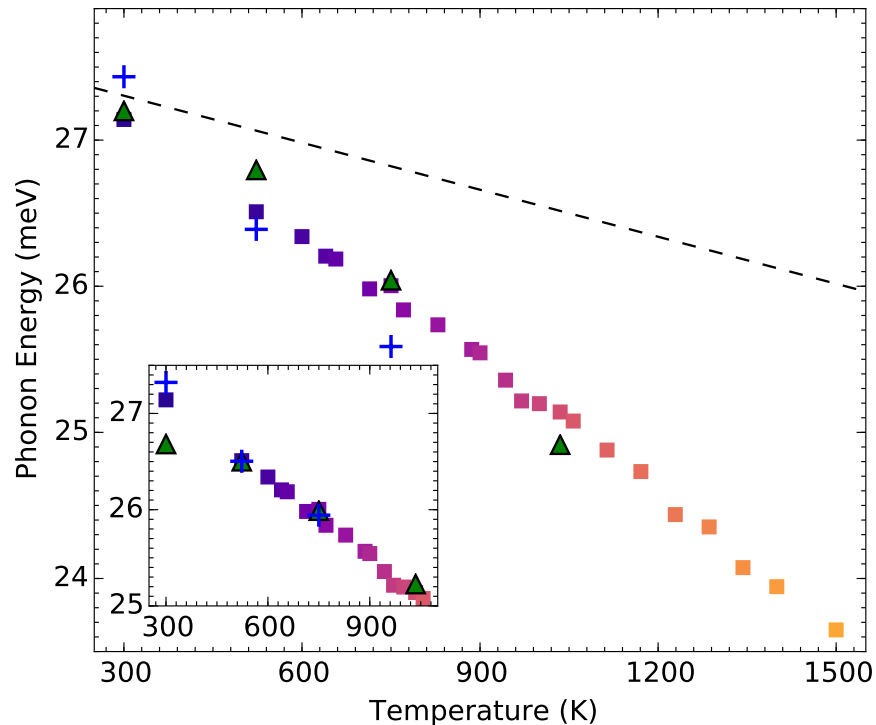


Figure 2.2: Temperature dependence of the M_5^- phonon energy calculated from TDEP (squares). The colors of the squares are identical to those shown in Fig. 2.1. The green and blue markers are mean phonon energies obtained from Lorentzian fits to the Fe NRIXS DOS and the INS DOS, respectively. The dashed line is the thermal softening of the M_5^- phonon from quasiharmonicity alone. The inset shows the agreement in the slopes of the experimental and computational phonon energies without quasiharmonic contributions. For convenience in showing the slopes, the NRIXS data were offset by -0.76 meV and the INS by -0.35 meV.

shows the thermal effects from pure anharmonicity and from the adiabatic EPI. These are significantly larger than the thermal softenings from quasiharmonicity reported in the Supporting Information.

The nonadiabatic electron-phonon interaction (EPI) is well known from conventional superconductivity, where electrons are paired by phonons with wavevectors that span the Fermi surface [16, 71]. With increasing temperature the effects of the nonadiabatic EPI dissipate [16], but there can be an increase in the adiabatic EPI, which requires excitations of both electrons and phonons [24, 72]. The adiabatic EPI can have a significant effect on the high-temperature thermodynamics of materials with sharp features in the electronic DOS at the Fermi level because the thermal broadening of electronic states can change the availability of electrons to screen atomic displacements in phonons [4, 10, 25, 26].

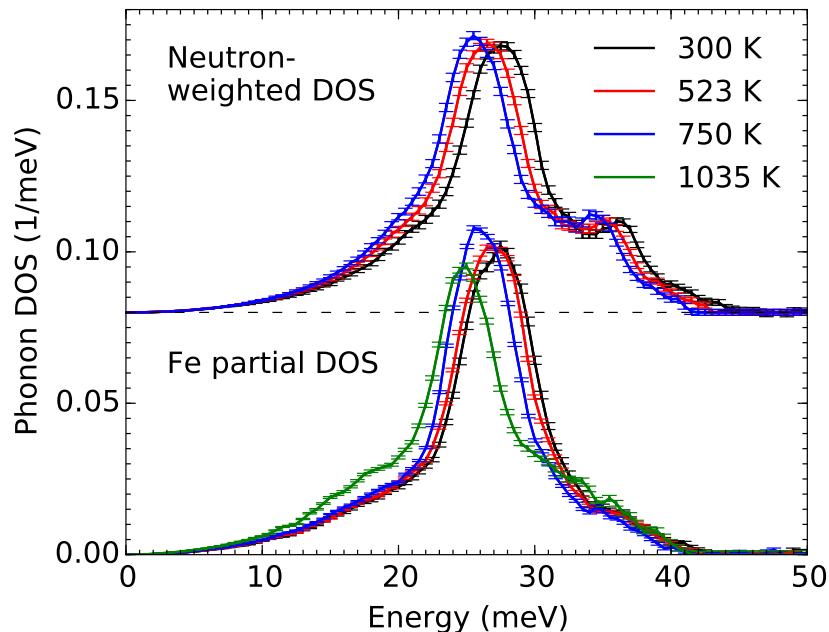


Figure 2.3: Experimental FeTi phonon DOS curves. The neutron-weighted DOS curves were obtained from INS measurements and the Fe partial DOS curves from NRIXS measurements. Error bars are from counting statistics.

To help understand the EPI in FeTi, density functional perturbation theory [73] implemented with the Quantum ESPRESSO package [74] was used to calculate 0 K electron-phonon linewidths

$$\Gamma_{\mathbf{q}\nu} = \frac{2\pi}{\hbar} \sum_{mn} \int \frac{d\mathbf{k}}{\Omega_{\text{BZ}}} |g_{mn}^{\nu}(\mathbf{k}, \mathbf{q})|^2 (f_{n\mathbf{k}} - f_{m\mathbf{k}+\mathbf{q}}) \quad (2.2)$$

$$\times \delta(\varepsilon_m(\mathbf{k} + \mathbf{q}) - \varepsilon_n(\mathbf{k}) - \hbar\omega_{\mathbf{q}\nu}), \quad (2.3)$$

where $g_{mn}^{\nu}(\mathbf{k}, \mathbf{q})$ is the matrix element of an EPI involving a phonon and two electronic states $|n\mathbf{k}\rangle$ and $|m\mathbf{k} + \mathbf{q}\rangle$, $f_{\mathbf{k}m}$ is the Fermi-Dirac distribution for electrons, and $\varepsilon_n(\mathbf{k})$ is the eigenenergy of an electron. The Supporting Information shows that many of the modes that soften with temperature in Fig. 2.1 are those with strong electron-phonon coupling and large $\Gamma_{\mathbf{q}\nu}$. Interestingly, these calculations showed that the M_5^- mode has a negligible electron-phonon linewidth at 0 K, even though it shows the strongest thermal softening in Fig. 2.1.

Figure 2.1 shows the anomalous behavior of the M_5^- mode, which softens increasingly rapidly with temperature as shown in Fig. 2.2. The M_5^- mode and modes near it contribute strongly to the softening of the phonon DOS peak around 25–27 meV. This mode is dominated by the motions of iron atoms, and both the experimental

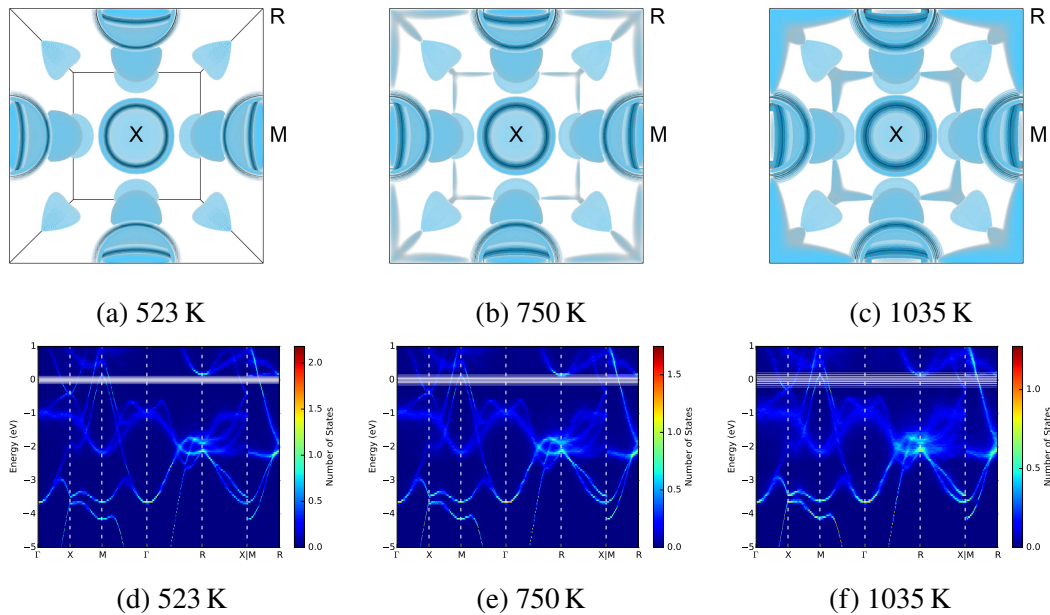


Figure 2.4: (a)-(c) Approximated finite-temperature Fermi surfaces in the Brillouin zone. The dark blue surfaces are the unshifted 0 K Fermi surfaces, and the lighter blue surfaces are at energies shifted from the Fermi energy by factors of $1.8 k_B T$. (d)-(f) Finite-temperature band structures from supercell AIMD calculations, produced by BandUP. The Fermi surface and band structure at 523 K resemble those at 0 K without any broadening.

DOS curves from inelastic neutron scattering (INS) and nuclear-resonant inelastic x-ray scattering (NRIXS) shown in Fig. 2.3 emphasize phonon scattering from iron atoms (Ti is a weaker scatterer of neutrons, and Ti cannot contribute to the NRIXS spectrum). When the phonon softening from thermal expansion, obtained from quasiharmonic calculations described in the Supporting Information is removed from the experimental points, the agreement in slopes of the curves in Fig. 2.2 is excellent. The magnitudes of the phonon energies show agreement between computation and experiment that is better than expected. For example, the experimental peaks include contributions from phonons around the R point, which lie above 3 meV higher than the M_5^- mode. (Agreement at lower temperatures is not expected owing to the use of classical statistical mechanics in the AIMD calculations.)

To calculate the adiabatic EPI, the effects of phonons were simulated by DFT calculations on supercells with thermal atom displacements, obtained at random times during the AIMD simulations. The thermal excitations of electrons were described by a thermal smearing function from the energy derivative of the Fermi-Dirac distribution function, which is similar to a Gaussian function with a standard deviation of $\sigma = 1.8 k_B T$. A discrete set of energies representative of this thermal

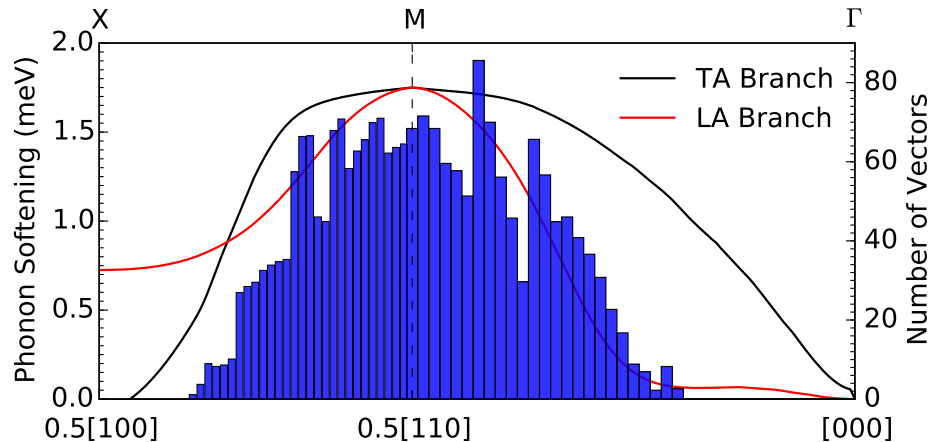


Figure 2.5: Histogram of spanning vectors that couple the new states at one of the R symmetry points with the rest of the Fermi surface along the $[\xi\xi 0]$ and $[\frac{1}{2}\xi 0]$ directions at 1035 K, displayed together with the changes in energies of the TA and LA branches from 300 K to 1035 K along the same directions.

spread gave a set of Fermi levels that were used to construct the Fermi surfaces of Fig. 2.4 (a)-(c). The BandUP code [75, 76] was used to project the supercell band structures into the range of k -space for a standard $B2$ unit cell. Through unfolding operations [77], BandUP obtains effective primitive cell representations of the band structures of systems simulated using supercells. Results are shown in Fig. 2.4(d)-(f). (We found no noticeable differences in the band structures when thermal expansion was included, as reported previously in Ref. [57].)

Owing to a decrease in band energy from thermal atom displacements, but more to the thermal smearing of the Fermi level, electronic states at the R point that lie above the Fermi level at 0 K intersect the Fermi level at high temperatures. New topological features appear in the Fermi surface around the R symmetry points and along the M-R symmetry lines of the Brillouin zone, as shown in Figs. 2.4(a)-(c). These new features grow with increasing temperature. This is a thermally-driven electronic topological transition.

When the Fermi surface allows for many spanning vectors of phonons, the electronic screening of charge displacements can be more efficient, and phonons exhibit softenings such as Kohn anomalies [19]. With the appearance of thermally-driven features of the Fermi surface around the R point, new sets of spanning vectors are available to couple electronic states across the Fermi surface. Spanning vectors along the $[\xi\xi 0]$ and $[\frac{1}{2}\xi 0]$ directions that connect these new features and the Fermi surface feature around the X points were counted as described in the Supporting In-

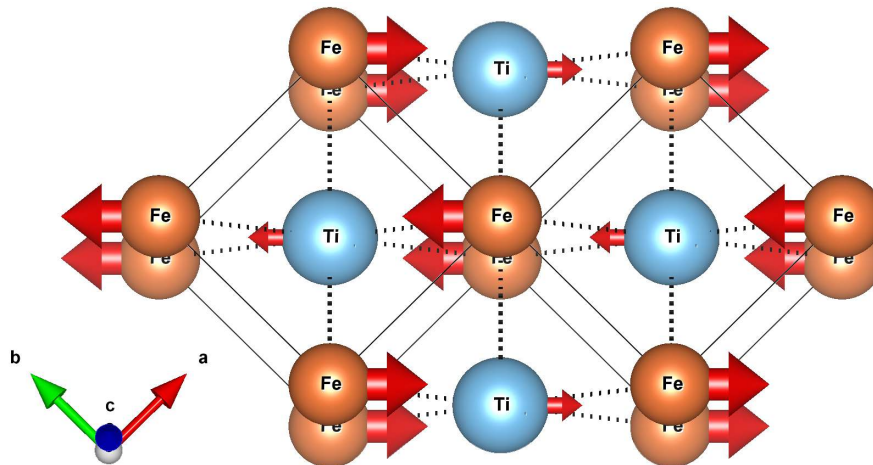


Figure 2.6: A view of the displacement pattern of the M_5^- phonon, in which Fe (orange) and Ti (blue) atoms move along the $[1\bar{1}0]$ directions. The dashed lines are the 1nn Fe–Ti interactions, and the solid lines are the 2nn Fe–Fe interactions.

formation. The numbers of vectors obtained for 1035 K are displayed in a histogram in Fig. 2.5. This distribution overlaps well with the group of wavevectors over which the transverse acoustic (TA) and longitudinal acoustic (LA) phonon branches soften significantly around the M symmetry point. These new spanning vectors should increase screening of the corresponding phonon modes by conduction electrons, causing the large softening of phonons as seen in Fig. 2.2. The softening graphed in Fig. 2.5 was corrected for the softening expected from phonon-phonon interactions calculated by the TDEP method, as described in the Supporting Information.

Interatomic force constants were calculated by the TDEP method, and they showed thermal weakening of both Fe–Ti first-nearest-neighbor (1nn) transverse force constants and Fe–Fe second-nearest-neighbor (2nn) longitudinal force constants. By testing the sensitivity of the phonon dispersions to changes in these force constants, we found that the thermal weakening of both the Fe–Ti 1nn transverse force constants and the Fe–Fe 2nn longitudinal force constants contribute significantly to the thermal softening of the M_5^- mode. This behavior is consistent with the atomic displacement pattern shown in Fig. 2.6, in which (110) planes slide in opposite $[1\bar{1}0]$ directions. (This is also a proposed displacement pattern for the structural phase transition in B2-ordered NiTi, a shape-memory alloy [78, 79].) From the phonon polarization vectors, we found that the magnitude of the Fe displacement is at least twice as that of Ti. Softening of the the Fe–Ti 1nn transverse force constants and the Fe–Fe 2nn longitudinal force constants are particularly effective for softening the M_5^- mode, and these changes occur with the thermally-driven ETT.

It has been known for a number of years that the adiabatic EPI can alter the phonon dynamics, often making an important contribution to the free energy of a metal or alloy. A temperature dependence of the adiabatic EPI occurs when there is a substantial variation in the electronic DOS at the Fermi level, for example. A thermally-driven ETT is expected to cause more rapid and perhaps more abrupt changes with temperature. Such effects are expected in materials with occupied or unoccupied bands that are a few $k_B T$ away from the Fermi level at low temperatures, so these effects are expected in many systems. Shifts and broadenings of the electronic bands from atomic displacement disorder can enhance or diminish these effects.

2.2 Supporting Information

Experimental

Sample Preparation

The FeTi sample for neutron scattering measurements was synthesized by arc-melting 99.98% pure Ti and 99.97% pure Fe in the equiatomic ratio under an argon atmosphere. There was a negligible mass loss and no visible oxidation after melting. The brittle sample was crushed into a fine powder. Samples for x-ray measurements were synthesized in the same way, but were 96% enriched with ^{57}Fe . Conventional characterization was performed with x-ray diffractometry using Cu K_α radiation. All samples were found to have the $B2$ structure and no traces of other phases. These diffraction measurements included the determination of thermal expansion using a furnace for in situ measurements. The lattice parameters of $B2$ FeTi were determined to be

$$2.978 \text{ \AA} \text{ at } 300 \text{ K}; 2.984 \text{ \AA} \text{ at } 523 \text{ K}; 2.991 \text{ \AA} \text{ at } 750 \text{ K}.$$

The coefficient of linear thermal expansion was $2.9 \times 10^{-5}/\text{K}$.

Scattering Measurements

Nuclear resonant inelastic x-ray scattering (NRIXS) measurements were performed at beamline 16 ID-D at the Advanced Photon Source at Argonne National Laboratory. NRIXS is sensitive only to the motions of ^{57}Fe atoms, so it provides partial phonon density of states (DOS) curves for Fe alone. For measurements at 300, 523, 748, and 1035 K, the sample was loosely dispersed between two Kapton polyimide films and then accommodated in a custom-built vacuum furnace. The sample was fixed at

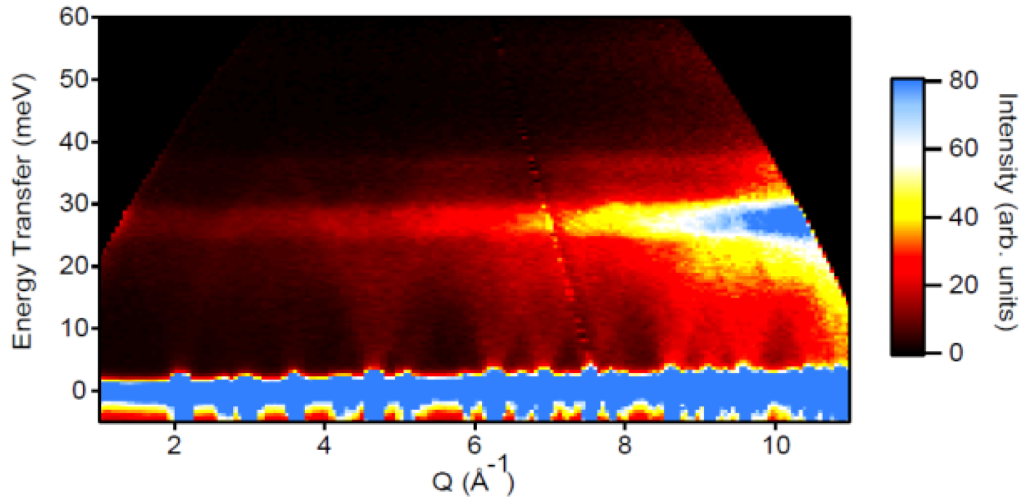


Figure 2.7: Neutron scattering function $S(Q, E)$ spectrum of FeTi at 300 K.

a grazing angle to the x-ray beam and an avalanche photodiode detector (APD) was set on top of the furnace at a right angle with the beam. The energy was scanned from -90 to $+90$ meV around 14.413 keV, the resonant energy of ^{57}Fe , in several scans that were combined for final analysis. The energy resolution of all NRIXS measurements was measured to be 2.2 meV (FWHM) at the elastic line. The NRIXS data were reduced using the PHOENIX code [80].

Inelastic neutron scattering (INS) measurements were performed with the ARCS spectrometer [81] at the Spallation Neutron Source at Oak Ridge National Laboratory. The sample was loaded into an Al can which was then mounted in a low-background vacuum furnace for measurements at 300 , 523 , and 748 K. The nominal incident neutron energy was 80 meV. The energy resolution was 1.7 meV at an energy transfer of 40 meV, increasing to 3.1 meV at the elastic line (FWHM). The empty Al can was measured at all temperatures and subtracted from the measured spectra of the sample. The data reduction was performed using the DANSE software [82], giving the neutron-weighted DOS curves $g_{\text{NW}}(\varepsilon)$ shown in Fig.2.8. Our NRIXS and INS spectra had very similar energy resolutions over much of the phonon spectra, and this permitted direct comparisons.

The neutron-weighting arises from the differences in the masses and neutron scattering cross-sections for each element and isotope. The neutron-weighted curves from INS could be corrected using the partial phonon DOS $g_{\text{Fe}}(\varepsilon)$ obtained from NRIXS as described in Refs. [83–86]. Results are shown in the “neutron-weight-corrected

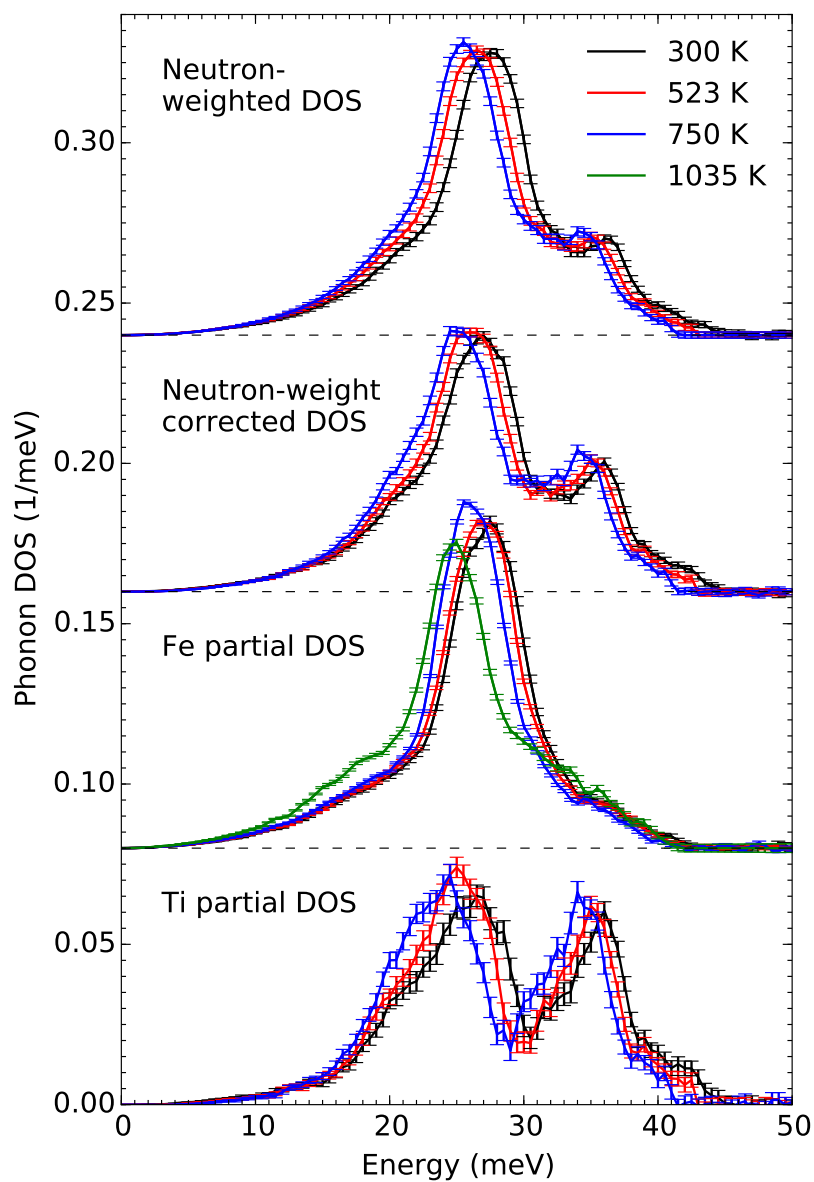


Figure 2.8: Phonon DOS curves for FeTi at elevated temperatures. The neutron-weighted DOS curves were obtained from INS measurements and the Fe partial DOS curves from NRIXS measurements. The two data sets were combined to obtain neutron-weight-corrected DOS curves and Ti partial DOS curves. Error bars from counting statistics.

DOS" panel in Fig. 2.8, noting that

$$g_{\text{NW}}(\varepsilon) \simeq \frac{\sigma_{\text{Fe}}}{M_{\text{Fe}}} g_{\text{Fe}}(\varepsilon) + \frac{\sigma_{\text{Ti}}}{M_{\text{Ti}}} g_{\text{Ti}}(\varepsilon), \quad (2.4)$$

where the ratios of the neutron cross section to molar mass σ_d/M_d are 0.208 and 0.091 barns/amu for Fe and Ti, respectively. The partial Ti phonon DOS $g_{\text{Ti}}(\varepsilon)$ was also obtained using this approach and is shown in the lower panel of Fig. 2.8.

Computational Details

Density Functional Theory

Density functional theory (DFT) calculations [64] were performed with VASP [65, 66] with projector augmented wave potentials with the Perdew-Burke-Ernzerhof (PBE) exchange-correlation functional [63] and an energy cutoff of 500 eV. The equilibrium volume of the structure was optimized to minimize the total energy. Spin-polarized calculations gave a negligible magnetic moment, in agreement with experimental results in Ref. [47].

The 0 K electronic band structure and Fermi surface were computed on the FeTi two-atom unit cell with a $80 \times 80 \times 80$ grid of k -points, sampled with the Monkhorst-Pack scheme [87]. The dense grid allowed for a greater sampling of phonon wavevectors which may span nesting features of the Fermi surface.

To assess the effect of thermal expansion on the phonons in FeTi, phonon dispersions shown in Fig. 2.9 were calculated under the quasiharmonic approximation using the Parlinski-Li-Kawazoe method [88] implemented in the PHONOPY code [89]. The calculations were performed on 128-atom $4 \times 4 \times 4$ supercells with a $6 \times 6 \times 6$ k -point mesh and a grid of atom displacements of 0.01 Å for the temperatures 0, 300, 523, 750, and 1035 K. The volumes of the supercells were calculated by minimizing the free energy $F(T, V)$:

$$F(T, V) = E_0(V) + \int d\varepsilon g(\varepsilon) \left[\frac{\varepsilon}{2} + k_{\text{B}}T \ln \left(1 - e^{-\varepsilon/k_{\text{B}}T} \right) \right]. \quad (2.5)$$

Ground-state energies $E_0(V)$ were calculated separately for each volume, and the DOS $g(\varepsilon)$ were calculated with lattice parameters that produced the minimized volume at each temperature. The calculated lattice parameters were smaller than the experimental ones by 0.7%. Figure 2.9 shows that the softening of the M_5^- phonon mode from thermal expansion alone is small compared to the large anomalous softening discussed in the main text.

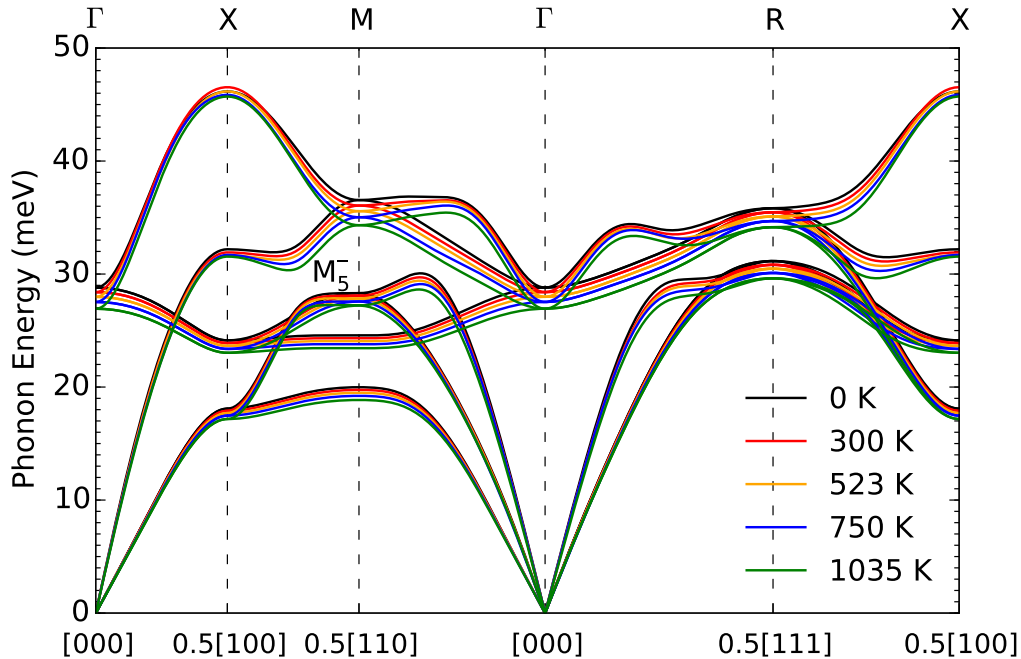


Figure 2.9: FeTi phonon dispersions calculated in the quasiharmonic model.

Density Functional Perturbation Theory

Density functional perturbation theory calculations [73] were performed with Quantum ESPRESSO [74] with ultrasoft pseudopotentials [90] and the PBE exchange-correlation functional. The electron-phonon interaction matrix elements were first calculated on a $20 \times 20 \times 20$ k mesh and a $10 \times 10 \times 10$ q mesh, and later interpolated to a $60 \times 60 \times 60$ q mesh through Fourier interpolation implemented in the package. The matrix elements were then used to compute the electron-phonon linewidth plotted in Fig. 2.10. It is seen that EP linewidths of the longitudinal optical modes along the Γ -X, Γ -M, and Γ -R symmetry lines are large compared to the negligible linewidths of many other modes, such as the M_5^- mode.

Ab-Initio Molecular Dynamics

Ab-initio molecular dynamics (AIMD) calculations were performed using VASP with the potentials given in the DFT section on 128-atom supercells using a $2 \times 2 \times 2$ k -point mesh for 23 temperatures from 300 to 1500 K. The energy cutoff was 400 eV and the Monkhorst-Pack scheme was used to sample the Brillouin zone. Each simulation was carried out for over 10,000 timesteps using a canonical ensemble and the standard Nosé thermostat [91]. The electronic DOS curves shown in Fig. 2.11 were computed for each temperature from 0 to 1035 K by averaging the recomputed

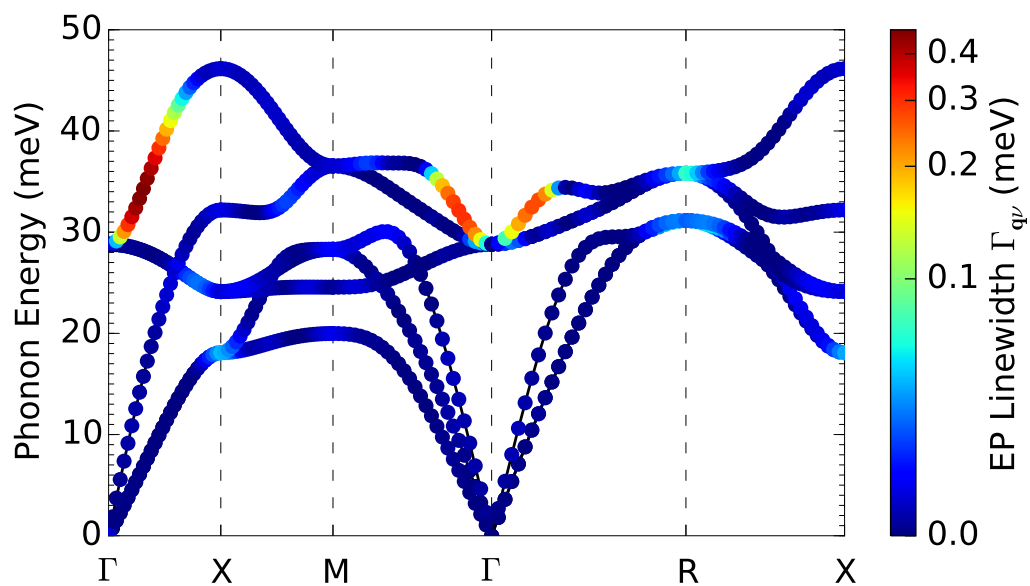


Figure 2.10: Calculated 0 K electron-phonon linewidths displayed over the 0 K FeTi phonon dispersion.

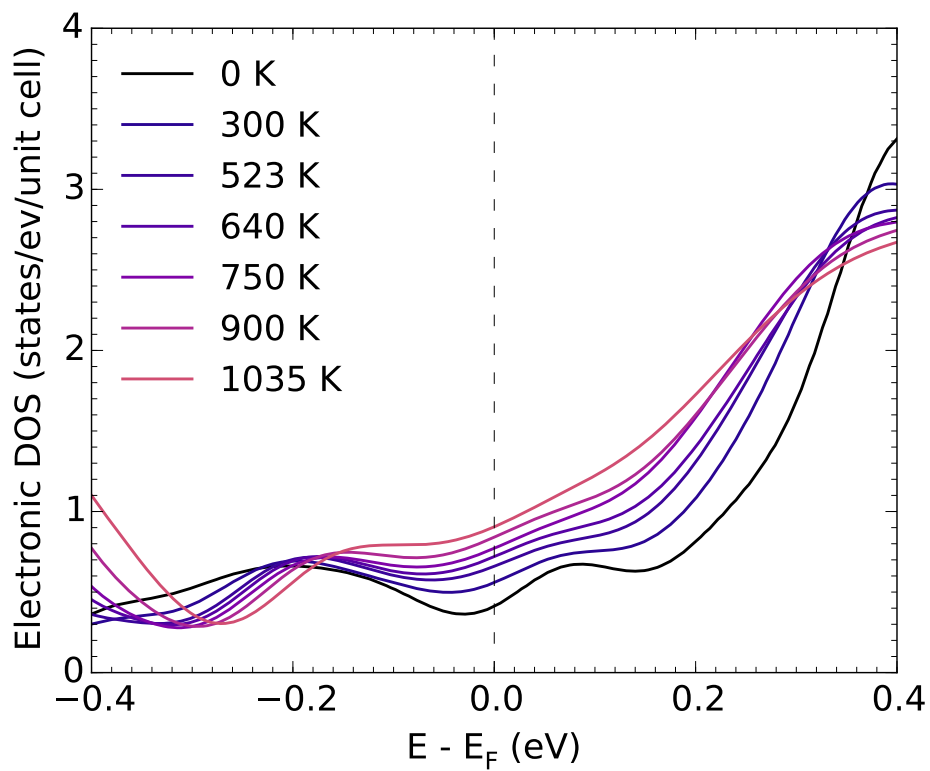


Figure 2.11: Electronic DOS for FeTi from 0 to 1035 K. Obtained from AIMD and static DFT calculations.

densities of states from 20 saved configurations using a $3 \times 3 \times 3$ k -point mesh. For each temperature, the BandUP code [75, 76] was performed on five of these configurations with 81 k -points along each high symmetry direction. The mean energies $\tilde{\varepsilon}_{\mathbf{k}m}$ and smearing widths $\Delta\varepsilon_{\mathbf{k}m}$ of the bands were obtained from BandUP.

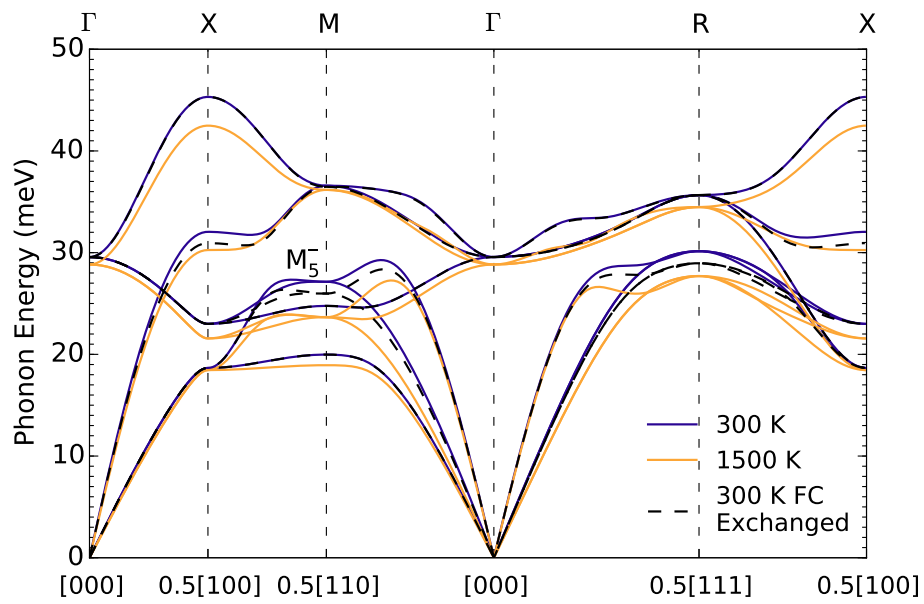
Spanning Vectors

The histogram in Fig. 5 of the main text was obtained by counting spanning vectors from one of the new topological features around the R symmetry points to the rest of the Fermi surface. The vectors were counted in the Brillouin zone defined by an $80 \times 80 \times 80$ grid of k -points. For each spanning vector, the conservation of momentum and energy was required:

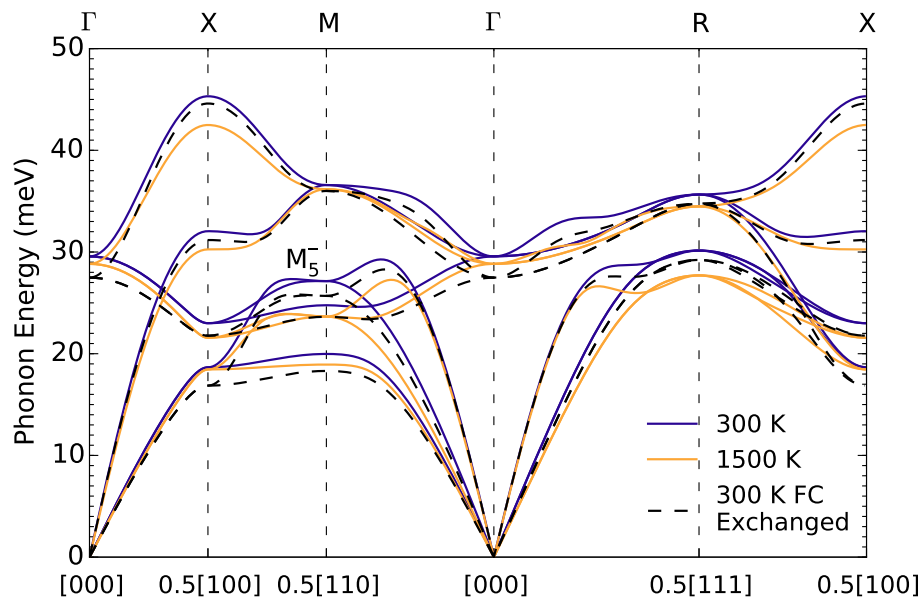
$$\tilde{\varepsilon}_{\mathbf{k}+\mathbf{q}n} - \varepsilon_{\mathbf{k}m} \pm \hbar\omega_{\mathbf{q}\nu} - c_i\sigma \leq \Delta\varepsilon_{\mathbf{k}+\mathbf{q}n}, \quad (2.6)$$

where $\mathbf{k} + \mathbf{q}n$ is a state on one of the new topological features around the R symmetry points, $\mathbf{k}m$ is a state from the rest of the Fermi surface, $\tilde{\varepsilon}_{\mathbf{k}+\mathbf{q}n}$ is the mean energy of the state $\mathbf{k} + \mathbf{q}n$ calculated by BandUP, $\varepsilon_{\mathbf{k}m}$ is equal to the Fermi energy, and $\hbar\omega_{\mathbf{q}\nu}$ is the energy of the phonon mode with polarization ν and wavevector \mathbf{q} . The smearing width $\Delta\varepsilon_{\mathbf{k}+\mathbf{q}n}$ describes the broadening of the electron pocket induced by the thermal disorder of the Fe and Ti atoms at higher temperatures.

The $c_i\sigma$ term describes the thermal excitation of electrons, where $\sigma = 1.8 k_B T$ is the standard deviation of the Gaussian-like thermal smearing function. Four histograms of spanning vectors were counted, one for each value of $c_i \in \{\frac{1}{3}, \frac{2}{3}, 1, \frac{4}{3}\}$. The histogram in Fig. 5 of the main text is an average of the four histograms, where each histogram is weighted according to the thermal smearing function.



(a) Fe-Fe 2nn Longitudinal



(b) Fe-Ti 1nn Transverse

Figure 2.12: FeTi phonon dispersions calculated after individually exchanging the (a) Fe-Fe 2nn longitudinal and (b) Fe-Ti 1nn transverse force constants at 300 K with those at 1500 K.

*Chapter 3*THERMAL EVOLUTION OF ELECTRON-PHONON
INTERACTIONS IN VANADIUM**3.1 Introduction**

Vanadium is a body-centered cubic (bcc) metal that displays some of the strongest electron-phonon coupling for pure elements [92]. It is a superconductor with a transition temperature $T_c = 5.3$ K, one of the highest critical temperatures for pure elements [16]. Experimental and computational studies on the superconductive, electronic, and mechanical properties of vanadium at high pressures have revealed anomalies in the elastic constants and a positive relationship between the superconducting transition temperature with pressure [93–96].

Elemental vanadium also displays anomalous behavior with temperature. The temperature dependence of the elastic constant C_{44} has two points of inflection at approximately 800 K and 1600 K [97]. Inelastic neutron scattering (INS) experiments have shown that the increase in the vibrational entropy of vanadium from thermal expansion is cancelled by nonharmonic thermal stiffening [98] attributed to an adiabatic electron-phonon interaction (EPI) broadening of the sharp features in the electronic density of states (DOS). The strength of the EPI was related to the decrease in the electronic DOS at the Fermi level [10].

Electron-phonon interactions at low temperatures have been extensively studied for almost a century. Advances over the past two decades have allowed us to calculate materials properties related to these electron-phonon interactions from first-principles [99]. These state-of-the-art methods for calculating properties from the EPI are based on density functional perturbation theory (DFPT), which does not adequately describe thermal effects observed at finite temperatures, such as anharmonic lattice dynamics. The adiabatic EPI at high temperatures had been best understood by studying the changes in the average phonon energies and the electronic DOS [10, 25, 26]. We are only now starting to see advances in first-principles computational methods for studying finite temperature electron-phonon interactions [100].

Chapter 2 showed how the thermal phonon softening in FeTi was linked to the appearance of new features on the Fermi surface with temperature [101]. The

adiabatic EPI was altered dramatically by a thermally-driven electronic topological transition (ETT), a novel Lifshitz transition [35] that had been rarely observed with temperature [43]. We suggested that a thermally-driven ETT may be observed in other materials with occupied or unoccupied electronic bands that are a few $k_B T$ from the Fermi level at low temperatures.

Delaire *et al.* reported that the adiabatic EPI in vanadium saturates at high temperatures owing to the complete smearing of a peak in the electronic DOS at the Fermi level. This was in agreement with the subsequent softening of phonons in vanadium past 1000 K. In this present work, we study the nonlinear nature of the phonon frequency shifts from the adiabatic EPI and investigate if this behavior can be attributed to a thermally-driven ETT using an extension of the computational methods employed in Chapter 2.

3.2 Computation

Phonon Calculations

Phonon frequencies at elevated temperatures were calculated with a modified temperature dependent effective potential (TDEP) method [11, 102, 103]. In the TDEP procedure, the Born-Oppenheimer surface of a material at a given temperature is sampled with *ab initio* molecular dynamics (AIMD). The energies, displacements, and forces on thermally displaced atoms are recorded over time. With these energy-force-displacement data sets, force constants are obtained with a least-squares fit of a model Hamiltonian to the potential-energy surface:

$$\mathcal{H} = U_0 + \sum_i \frac{\mathbf{p}_i^2}{2m_i} + \frac{1}{2!} \sum_{ij\alpha\beta} \Phi_{ij}^{\alpha\beta} u_i^\alpha u_j^\beta + \frac{1}{3!} \sum_{ijk\alpha\beta\gamma} \Phi_{ijk}^{\alpha\beta\gamma} u_i^\alpha u_j^\beta u_k^\gamma, \quad (3.1)$$

where \mathbf{p}_i and u_i are the momentum and displacement of atom i , respectively, and $\alpha\beta\gamma$ are Cartesian components. The temperature-dependent U_0 is a fit parameter for the baseline of the potential energy surface [102]. The quadratic force constants Φ_{ij} capture temperature-dependent nonharmonic effects and are used to calculate phonon frequencies ω shifted by these effects [102]. These quadratic force constants are also renormalized by the quartic term in the potential [68, 69]. The cubic force constants Φ_{ijk} capture phonon-phonon interactions (PPI) that contribute to the broadening and additional shifts of phonon modes.

The same model Hamiltonian was used in this work, except the Born-Oppenheimer surface was sampled by multiple density functional theory (DFT) calculations on supercells of thermally displaced atoms generated by stochastic sampling of a canonical

ensemble. For a cell of N_a atoms with mass m_i , a harmonic normal-mode transformation was used to generate positions $\{u_i\}$ consistent with a canonical ensemble:

$$u_i = \sum_{s=1}^{3N_a} \epsilon_{is} \langle A_{is} \rangle \sqrt{-2 \ln \xi_1} \sin(2\pi \xi_2), \quad (3.2)$$

where ξ_n are uniformly distributed numbers between 0 and 1 producing the Box-Muller transform. $\langle A_{is} \rangle$ is the thermal amplitude of the normal mode s with eigenvector ϵ_{is} and frequency ω_s [104, 105]:

$$\langle A_{is} \rangle = \underbrace{\sqrt{\frac{\hbar(2n_s + 1)}{2m_i\omega_s}}}_{\text{quantum}} \approx \underbrace{\frac{1}{\omega_s} \sqrt{\frac{k_B T}{m_i}}}_{\text{classical}}, \quad (3.3)$$

where $n_s = (e^{\hbar\omega_s/k_B T} - 1)^{-1}$ is the thermal occupation of mode s , and $\hbar\omega \ll k_B T$ denotes the classical limit at high temperatures.

These stochastically generated thermal displacements from Eqs. 3.2 and 3.3 sample the Born-Oppenheimer surface in the stochastically initialized temperature-dependent effective potential (s-TDEP) method [11, 102, 103, 106, 107]. This method approximates the inclusion of zero-point motion not included in AIMD simulations and connects seamlessly to the classical limit at high temperature. The s-TDEP procedure can be used to calculate force constants capturing anomalous high-temperature effects [106–109] to low-temperature quantum effects [110, 111] at a much lower computational cost than what is required by AIMD. The force constants calculated with this method are numerically converged with respect to the number of configurations and supercell size. The convergence of the force constants and the baseline U_0 was further ensured by repeating DFT calculations on new snapshots generated from force constants from the previous iteration of s-TDEP. The force constants used to generate the supercells in the first iteration of s-TDEP were generated through a model pair potential as described in Ref. [106]. The weakness of the s-TDEP method is that it relies on Gaussian distributions of coordinates generated by Eq. 3.2.

The *ab initio* DFT calculations were performed with the projector augmented wave [112] formalism as implemented in VASP [65, 66]. All calculations used a supercell with 250 vanadium atoms, a $3 \times 3 \times 3$ Monkhorst-Pack [87] k -point grid, and a plane-wave energy cutoff of 580 eV. The exchange–correlation energy was calculated with the PBE functional [63].

These force constants were calculated on a grid of six temperatures, $\{0, 300, 550, 750, 1250, 1650\}$ K, and six volumes. The quadratic and cubic interatomic force constants for temperatures and volumes between these grid points were obtained by interpolation. Through three iterations of the s-TDEP procedure, we obtained the Helmholtz free energy surface $F(V, T)$:

$$F(V, T) = U_0(V, T) + F_{\text{vib}}(V, T). \quad (3.4)$$

$U_0(V, T)$ is the baseline from Eq. 3.1. $F_{\text{vib}}(V, T)$ is from lattice vibrations:

$$F_{\text{vib}} = \int_0^\infty g(\omega) \left\{ k_B T \ln \left[1 - \exp \left(-\frac{\hbar\omega}{k_B T} \right) \right] + \frac{\hbar\omega}{2} \right\} d\omega, \quad (3.5)$$

where $g(\omega)$ is the phonon density of states calculated from the phonons in the first Brillouin zone,

$$g(\omega) = \sum_s \delta(\omega - \omega_s). \quad (3.6)$$

We minimized the free energy to calculate the equilibrium volume at each temperature and evaluated the phonon frequencies at these conditions.

We then corrected our phonon frequencies by calculating the linewidths Γ_s and shifts Δ_s arising from anharmonicity, or phonon-phonon interactions. This required the many-body perturbation calculation of the real and imaginary parts of the phonon self-energy [70, 113] $\Sigma(\Omega) = \Delta(\Omega) + i\Gamma(\Omega)$, where $E = \hbar\Omega$ is a probing energy. The imaginary component $\Gamma(\Omega)$ is

$$\begin{aligned} \Gamma_s(\Omega) = & \frac{\hbar\pi}{16} \sum_{s's''} |\Phi_{ss's''}|^2 \{ (n_{s'} + n_{s''} + 1) \delta(\Omega - \omega_{s'} - \omega_{s''}) \\ & + (n_{s'} - n_{s''}) [\delta(\Omega - \omega_{s'} + \omega_{s''}) - \delta(\Omega + \omega_{s'} - \omega_{s''})] \} \end{aligned} \quad (3.7)$$

and the real component is obtained by a Kramers-Kronig transformation

$$\Delta(\Omega) = \frac{1}{\pi} \int \frac{\Gamma(\omega)}{\omega - \Omega} d\omega. \quad (3.8)$$

The imaginary component of the self-energy is a sum over all possible three-phonon interactions, where $\Phi_{ss's''}$ is the three-phonon matrix element determined from the cubic force constants Φ_{ijk} . $\Gamma(\Omega)$ and $\Delta(\Omega)$ were calculated with a $28 \times 28 \times 28$ q -grid.

Anharmonic phonon DOS curves were calculated with the real and imaginary parts of the phonon self-energy:

$$g_{\text{anh}}(\omega) = \sum_s \frac{2\omega_s \Gamma_s(\omega)}{[\omega^2 - \omega_s^2 - 2\omega_s \Delta_s(\omega)]^2 + 4\omega_s^2 \Gamma_s^2(\omega)}. \quad (3.9)$$

If both Δ and Γ go to zero, Eq. 3.9 reduces to Eq. 3.6.

To evaluate the effects of thermal expansion, the phonon energies predicted by the quasiharmonic (QH) approximation were calculated by interpolation of the 0 K quadratic force constants to volumes obtained from the minimization of the free energy. The QH calculations exclude the anharmonic corrections provided by Eqs. 3.7 and 3.8.

Electronic Band Unfolding

The electronic band structure of vanadium at 0 K can be calculated through a DFT calculation on a static lattice using a primitive unit cell (PC). We model finite temperatures with supercell (SC) calculations with thermally displaced atoms. The electronic bands from these calculations are folded into a smaller SC Brillouin zone (SCBZ), giving rise to complicated band structures that cannot be directly compared to 0 K electronic bands in the larger primitive cell Brillouin zone (PCBZ).

We can recover an approximation of these supercell electronic bands in the PCBZ through band unfolding [77] as implemented with the BANDUP software package [75, 76]. Details of the implementation of the band unfolding procedure are available in Refs. [75] and [76]. In brief, BANDUP is used to obtain the spectral function $A(\mathbf{k}; \varepsilon)$ from supercell calculations [77, 114]

$$\begin{aligned} A(\mathbf{k}, \varepsilon) &= \sum_m P_{m\mathbf{K}}(\mathbf{k}) \delta(\varepsilon - \varepsilon_m(\mathbf{K})) \\ &= \sum_m \sum_n |\langle m\mathbf{K} | n\mathbf{k} \rangle|^2 \delta(\varepsilon - \varepsilon_m(\mathbf{K})), \end{aligned} \quad (3.10)$$

where $\{\mathbf{k}\}$ and $|n\mathbf{k}\rangle$ are electron wavevectors and eigenstates in the PCBZ, and $\{\mathbf{K}\}$ and $|m\mathbf{K}\rangle$ are electron wavevectors and eigenstates in the SCBZ. The spectral weight $P_{m\mathbf{K}}(\mathbf{k})$ is the projection of $|m\mathbf{K}\rangle$ on all of the PC Bloch states $|n\mathbf{k}\rangle$ at the PC wavevector \mathbf{k} . The only pairs of wavevectors (\mathbf{k}, \mathbf{K}) that are included in the sum in Eq. 3.10 are those in which \mathbf{K} unfolds onto \mathbf{k} :

$$\mathbf{k} = \mathbf{K} + \mathbf{G}, \quad (3.11)$$

where \mathbf{G} is a reciprocal lattice vector in the SBCZ.

The unfolded electronic band structure is represented as an effective PC band structure (EBS). In BANDUP, this quantity is calculated from the spectral function with

the infinitesimal version of the cumulative probability function $S_{\mathbf{k}}(\varepsilon)$. The quantity $dS_{\mathbf{k}}(\varepsilon) = A(\mathbf{k}, \varepsilon)d\varepsilon$ represents the number of PC electronic bands at the PC wavevector \mathbf{k} crossing the energy interval $(\varepsilon, \varepsilon + d\varepsilon)$. We can obtain the EBS $\delta N(\mathbf{k}_i, \varepsilon_j)$ in a region of interest in the $(\mathbf{k}, \varepsilon)$ space with energy intervals of size $\delta\varepsilon$:

$$\begin{aligned} \delta N(\mathbf{k}_i, \varepsilon_j) &= \int_{\varepsilon_j - \delta\varepsilon/2}^{\varepsilon_j + \delta\varepsilon/2} dS_{\mathbf{k}_i}(\varepsilon) \\ &= \sum_m P_{m\mathbf{K}}(\mathbf{k}_i) \int_{\varepsilon_j - \delta\varepsilon/2}^{\varepsilon_j + \delta\varepsilon/2} \delta(\varepsilon - \varepsilon_m(\mathbf{K}))d\varepsilon. \end{aligned} \quad (3.12)$$

The EBS gives the number of PC electronic bands crossing $(\mathbf{k}_i, \varepsilon_j)$.

The EBS calculated from this unfolding procedure is exactly equal to the PC electronic band structure only for perfect supercells, where the atoms are in their equilibrium positions. The EBS calculated with BANDUP shows the effects of perturbations on the electronic structure such as from crystallographic defects and atom substitutions [75, 76].

For the electronic band structure at 1100 K, we assembled an ensemble of supercells $\{\eta\}$ with thermal displacements $\{u_i\}$ generated with Eqs. 3.2 and 3.3 and phonon frequencies at 1100 K. For each of the configurations η with displacements $\{u_i\}$, we calculated the EBS $\delta N_\eta(\mathbf{k}_i, \varepsilon_j)$, where $\varepsilon_j \equiv E_j - E_F^{(\eta)}$ is defined with respect to the Fermi energy $E_F^{(\eta)}$ calculated for the supercell η . The thermal atomic displacements from the equilibrium positions are treated as perturbations. Our calculated electronic structure at 1100 K is the ensemble average of the EBS $\langle \delta N_\eta \rangle$. This methodology was previously used to model finite temperature electronic bands in FeTi [101].

Density Functional Perturbation Theory

Density functional perturbation theory calculations [73] were performed with Quantum ESPRESSO [74, 115] with ultrasoft pseudopotentials [90] and the Perdew-Burke-Ernzerhof (PBE) exchange-correlation functional [63]. The electron-phonon interaction matrix elements were first calculated on a $72 \times 72 \times 72$ k -point mesh and a $12 \times 12 \times 12$ q -point mesh, and later interpolated to 720 q -points along the high symmetry lines in the bcc Brillouin zone through Fourier interpolation implemented in the package. The matrix elements were then used to compute the scattering rates of phonons by electrons:

$$\begin{aligned} \frac{1}{\tau_{\mathbf{q}\nu}} &= \frac{2\pi}{\hbar} \sum_{mn} \int \frac{d\mathbf{k}}{\Omega_{\text{BZ}}} |g_{mn}^{\nu}(\mathbf{k}, \mathbf{q})|^2 (f_{n\mathbf{k}} - f_{m\mathbf{k}+\mathbf{q}}) \\ &\quad \times \delta(\varepsilon_m(\mathbf{k} + \mathbf{q}) - \varepsilon_n(\mathbf{k}) - \hbar\omega_{\mathbf{q}\nu}), \end{aligned} \quad (3.13)$$

where $g_{mn}^\nu(\mathbf{k}, \mathbf{q})$ is the electron-phonon interaction matrix element associated with a phonon mode ν with wavevector \mathbf{q} and two electronic states with the eigenstates $|m\mathbf{k}\rangle$ and $|n\mathbf{k} + \mathbf{q}\rangle$, and $f_{m\mathbf{k}}$ is the Fermi-Dirac distribution for electrons. The electron-phonon coupling strength associated with this interaction is

$$\lambda_{\mathbf{q}\nu} = \frac{1/\tau_{\mathbf{q}\nu}}{\pi N(E_F)\omega_{\mathbf{q}\nu}}, \quad (3.14)$$

where $N(E_F)$ is the electronic DOS at the Fermi level.

3.3 Results

Phonons

Figure 3.1(a) shows phonon densities of states of vanadium calculated with the s-TDEP method at temperatures from 0 to 1650 K. There is no significant broadening from PPI. The high-energy longitudinal phonon modes from 26 to 30 meV stiffen before they begin to slowly soften with temperature. This anomalous behavior is seen more clearly in the plot of average phonon energies derived from the phonon DOS in Fig. 3.1(b): the average phonon energy increases with temperature before it begins to decrease starting at around 750 K. This behavior strongly deviates from what is predicted by the QH model, where the average phonon energy decreases in the entire temperature range. The calculated average phonon energies and their thermal trend are in good agreement with inelastic neutron scattering (INS) measurements of the vanadium phonon DOS [10, 84, 98].

We further verified our computational results by comparing our calculated 300 K spectral function $S(\mathbf{q}, \omega)$ to room temperature phonon dispersions measured with thermal diffuse x-ray scattering (TDS) [116] and inelastic x-ray scattering (IXS) [117], shown in Fig. 3.2. The s-TDEP spectral function agrees with both the IXS (particularly along the H-P and Γ -P directions) and the TDS measurements (the longitudinal branch along the Γ -H and Γ -N directions). The Kohn anomalies [19] are more pronounced in the s-TDEP spectral function along Γ -H and Γ -N than the TDS and IXS measurements, and there are disparities for the transverse acoustic TA_1 phonon mode at the N symmetry point. We observe a crossover of the longitudinal phonon branch with the the TA_2 branch at the N symmetry point in the TDS, IXS, and s-TDEP phonon dispersions. This anomaly and many other features seen in our s-TDEP spectral function have been observed in the phonon dispersions calculated with DFPT by Luo *et al.* [94].

From 0 to 1650 K (Fig. 3.3), many phonon modes soften with temperature, including

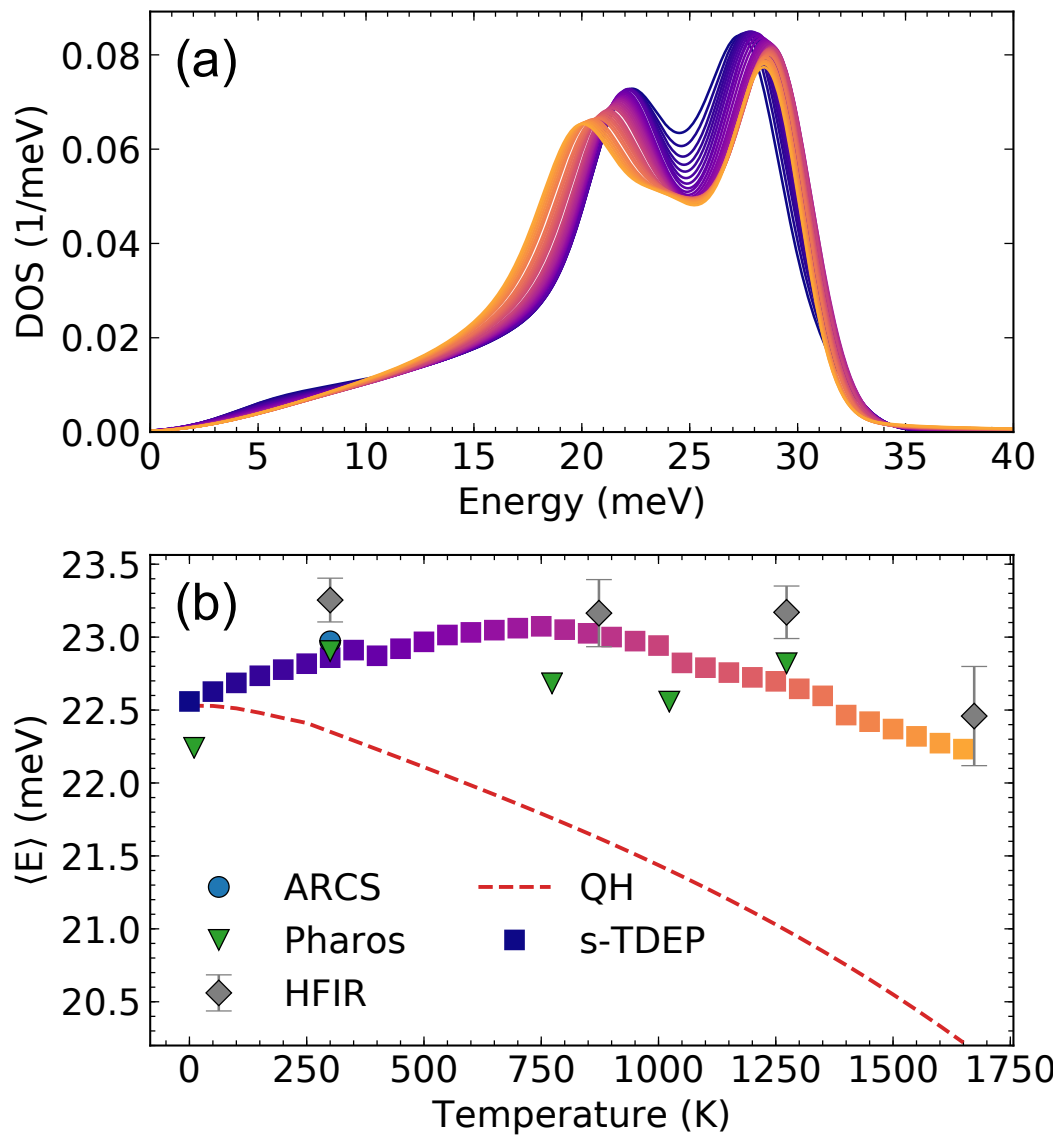


Figure 3.1: (a) The phonon DOS curves of vanadium calculated with the s-TDEP method at temperatures from 0 (dark purple) to 1650 K (orange). (b) Average phonon energies of vanadium calculated with the s-TDEP method (identical colors to those shown in (a)), shown together with average phonon energies from inelastic neutron scattering measurements (Refs. [10, 84, 98]). The dashed red curve corresponds to quasi-harmonic (QH) behavior as calculated from first-principles.

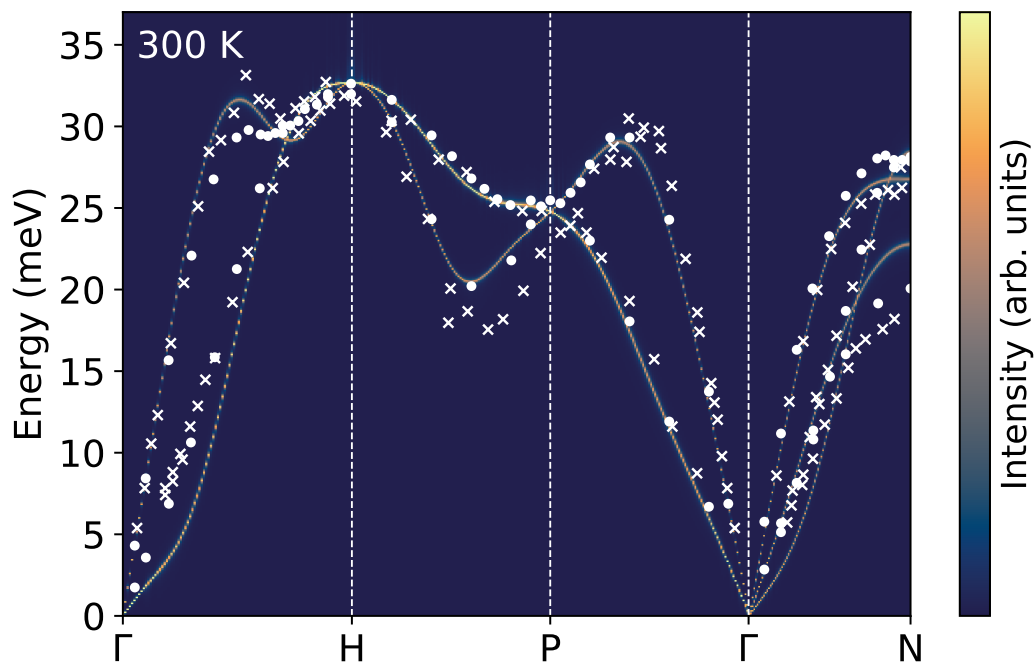


Figure 3.2: The 300 K spectral function calculated with s-TDEP along the high-symmetry directions, plotted together with measurements from thermal diffuse x-ray scattering (crosses) [116] and inelastic x-ray scattering (dots) [117].

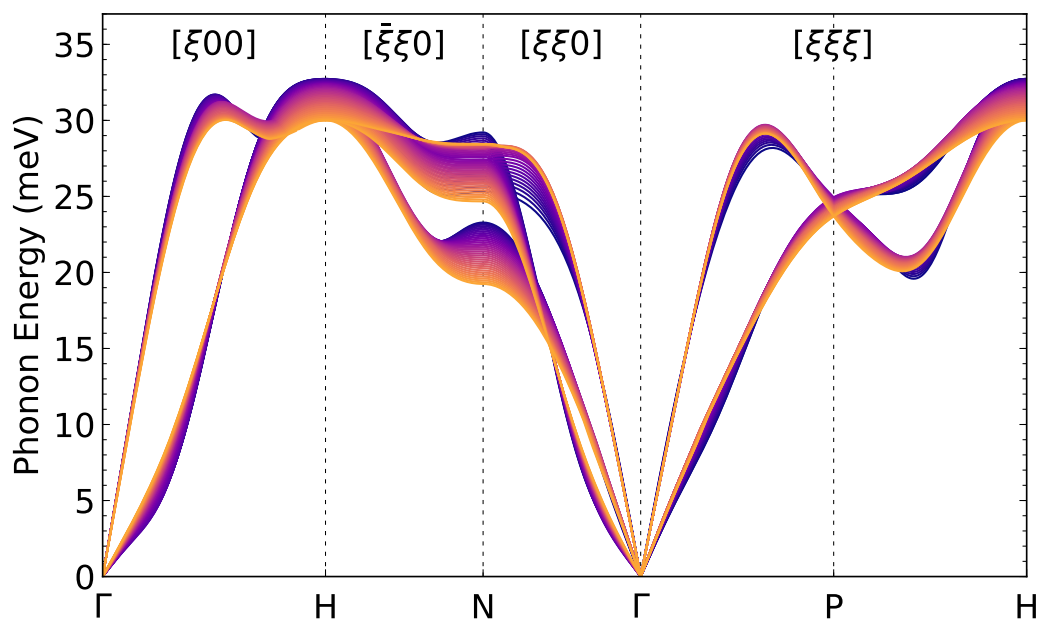


Figure 3.3: Phonon dispersion curves of vanadium calculated with the s-TDEP method at temperatures from 0 (dark purple) to 1650 K (orange). Vector coordinates are written in simple cubic lattice coordinates.

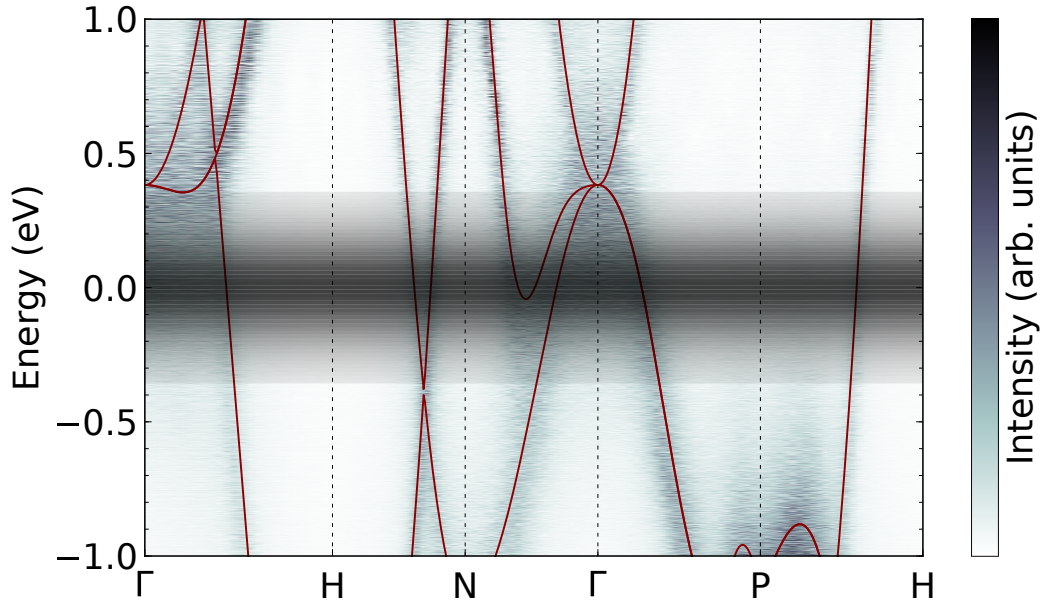


Figure 3.4: Unfolded electronic bands at 1100 K, compared with 0 K electronic bands in dark red. The Fermi level is represented as a spread in energies.

the transverse acoustic modes at the N symmetry point and the phonon modes at the H and P symmetry points. A few phonon modes stiffen before they begin softening with temperature, such as the longitudinal phonon mode at $\mathbf{q} = \left[\frac{1}{3}\frac{1}{3}\frac{1}{3}\right]$ along the Γ -P direction. A number of phonon modes stiffen with temperature, including the Kohn anomalies close to the Γ point along the Γ -H, Γ -N, and Γ -P directions. The anomalous crossover of the longitudinal and TA_2 phonon modes at the N symmetry point is no longer present at high temperatures because the longitudinal phonon mode stiffens strongly with temperature. The stiffening of the longitudinal phonon modes at the N symmetry point and $\mathbf{q} = \left[\frac{1}{3}\frac{1}{3}\frac{1}{3}\right]$ contribute to the anomalous behavior of the longitudinal peak in the phonon DOS.

Electronic Band Structure

Figure 3.4 shows the electronic band structure of vanadium at 1100 K calculated with band unfolding implemented with BANDUP. The 1100 K electronic band structure is the average of the EBS $\langle \delta N_\eta \rangle$ calculated from 15 stochastically generated supercells with thermal displacements characteristic of 1100 K. Each EBS was calculated from -1 to 1 eV along the high-symmetry directions of the bcc Brillouin zone in $(\mathbf{k}, \varepsilon)$ space.

The Fermi level is represented as a distribution of energies at 1100 K. This accounts

for how the occupation of electronic states is neither exactly 0 nor exactly 1 within a few $k_B T$ around the Fermi energy, as specified by the Fermi-Dirac distribution at finite temperatures. This is our visual representation of the *thermal layer* $\Delta\varepsilon$ of thickness proportional to $k_B T$ in which there are electrons together with empty states into which they may be scattered [15].

We do not observe significant shifts in the positions of the electronic bands from 0 to 1100 K. What we do observe is a strong broadening of these electronic bands with thermal disorder, a high temperature phenomenon that is consistent with predictions from the Allen-Heine-Cardona (AHC) theory [118–123]. Electronic states at the Γ point intersect the thermal layer because of this strong broadening.

Fermi Surface

We have calculated the Fermi surface of vanadium at 0 and 1100 K through band unfolding implemented with BANDUP. The EBS for a given supercell η was calculated for ε from -0.50 to $+0.50$ eV for all of the k -points that make up the bcc irreducible Brillouin zone in a $50 \times 50 \times 50$ k -point grid. The Fermi surface $F(\mathbf{k}, \varepsilon)$ is our average EBS $\langle \delta N_\eta \rangle$ unfolded from the irreducible Brillouin zone to the full Brillouin zone. We unfold the EBS by applying the symmetry operations used to recover the full Brillouin zone from the irreducible Brillouin zone.

For visualization, each k -point in the Brillouin zone is assigned an intensity derived from integrating the average EBS $\langle \delta N_\eta \rangle$ over our integration window:

$$I(\mathbf{k}) = \int_{\varepsilon_{\min}}^{\varepsilon_{\max}} \langle \delta N_\eta(\mathbf{k}, \varepsilon) \rangle \left(-\frac{\partial f(\varepsilon, T)}{\partial \varepsilon} \right) d\varepsilon. \quad (3.15)$$

The EBS is weighted against the derivative of the Fermi-Dirac distribution $f(\varepsilon, T)$ with respect to energy. This derivative provides us a distribution function with a width proportional to the thermal layer [15], which was represented as the distribution of energies $\Delta\varepsilon$ around the Fermi energy in Fig. 3.4. For 0 K, this distribution function is a Dirac delta function, yielding intensities expected from the definition of the 0 K Fermi surface as the map of k -points where electronic bands intersect the Fermi energy ($\varepsilon = E - E_F = 0$).

The $\{100\}$ cross sections of the Fermi surface are shown in Fig. 3.5 for 0 and 1100 K. The cross section of the 0 K Fermi surface in Fig. 3.5(a) is similar to what was calculated by Landa *et al.* [96]. The broadening Δk of the electronic states in Fig. 3.5(b) arises from both thermal atomic displacements and the thermal layer. Representing the finite temperature Fermi surface as an overlay of surfaces defined

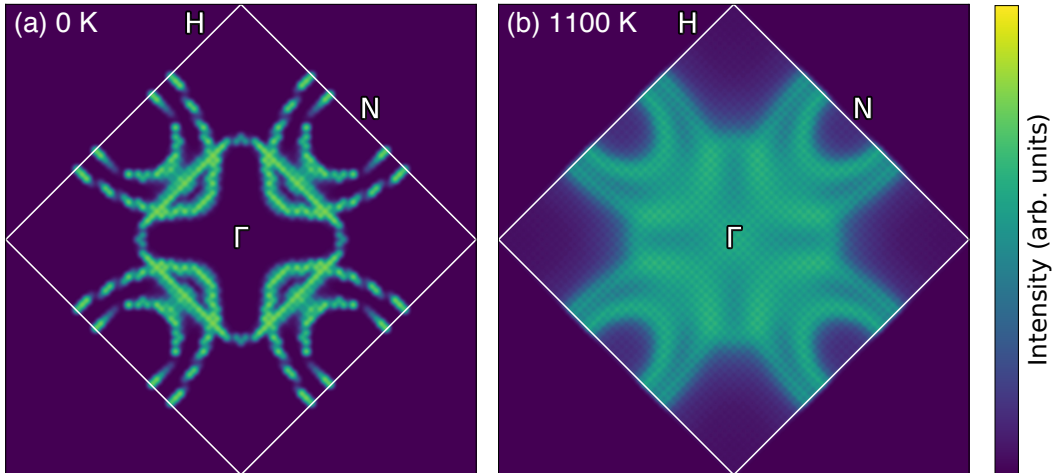


Figure 3.5: The $\{100\}$ cross sections of the Fermi surface of vanadium at (a) 0 K and (b) 1100 K (cross section indices are expressed in simple cubic coordinates).

in the thermal layer allows us to account for all of the electronic states relevant for thermodynamic and transport properties, such as the electronic specific heat and conductivity [15].

The values for the intensity $I(\mathbf{k})$ of the 1100 K Fermi surface are lower than the values for the 0 K Fermi surface. The broadening Δk of the Fermi surface washes away sharp features of the 0 K Fermi surface, especially for the closed distorted hole-ellipsoids centered at the N symmetry points. The distorted octahedron closed hole-pocket centered at the Γ point at 0 K is no longer distinguishable from these hole-ellipsoids at elevated temperatures. We observe a number of additional electronic states at the Γ point at 1100 K arising from the broadening of the triply degenerate electronic band seen in Fig. 3.4. The formerly hollow octahedron is filled up with these new electronic states in a thermally-driven ETT.

3.4 Discussion

Fermi Surface Nesting

The 0 K electron-phonon coupling strength $\lambda_{q\nu}$ was calculated for vanadium and is plotted in Fig. 3.6. The maximum value for the electron-phonon coupling strength is observed for the transverse phonon branch near the Γ point along the Γ -H direction, coinciding with the Kohn anomaly [19]. Peaks in the electron-phonon coupling strength are also observed for transverse phonon branches close to the Γ point along the Γ -N and Γ -P directions. A high value for the electron-phonon coupling strength is observed for the longitudinal phonon mode at the N point. This is the same

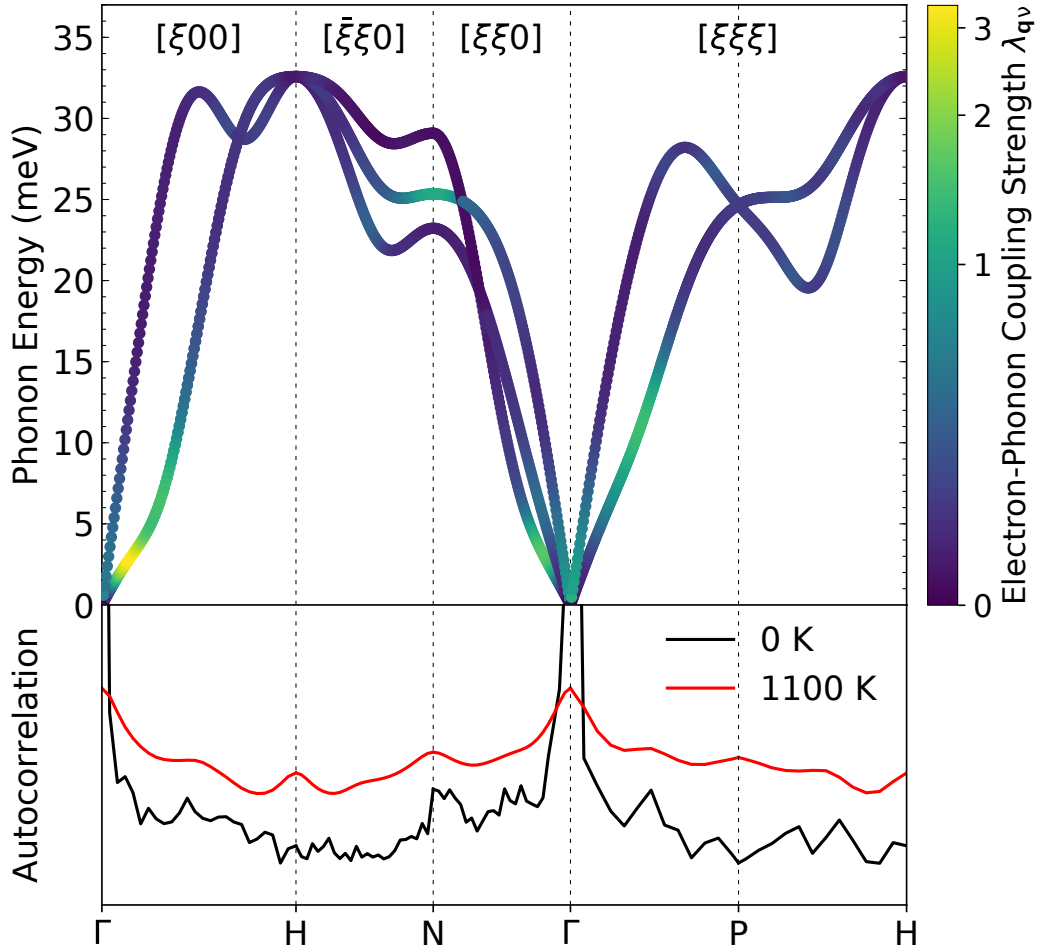


Figure 3.6: (Top) 0 K electron-phonon coupling strengths of phonon modes calculated with Quantum ESPRESSO displayed over the 0 K vanadium phonon dispersion calculated with s-TDEP. (Bottom) Autocorrelation of the Fermi surface at 0 and 1100 K.

phonon mode that crosses over with the high transverse acoustic mode. All of these phonon modes stiffen with temperature (Fig. 3.3).

The peak in the electron-phonon coupling strength along the Γ -H direction coincides with the peak at the wavevector $\mathbf{q} = [0.24, 0, 0]$ in the generalized susceptibility calculated by Landa *et al.* [96]. The wavevector $\mathbf{q} = [0.24, 0, 0]$ spans nesting features, pairs of parallel sheets in the Fermi surface $\{|n\mathbf{k}\rangle\}$ and $\{|m\mathbf{k}'\rangle\}$ that are related by $\mathbf{k}' = \mathbf{k} + \mathbf{q} + \mathbf{g}$, where \mathbf{g} is a reciprocal lattice vector. A high density of these *spanning vectors* results in high numbers of nonzero terms in Eq. 3.13. The peaks in the electron-phonon coupling strength along Γ -N, Γ -P, and at N may correspond to additional wavevectors that span Fermi surface nesting features.

We can probe for spanning wavevectors by calculating the periodic autocorrelation of the Fermi surface

$$R(\mathbf{q}) = \frac{1}{N_F} \sum_{\mathbf{k}} I(\mathbf{k})I(\mathbf{k} + \mathbf{q} + \mathbf{g}), \quad (3.16)$$

where $I(\mathbf{k})$ is the integrated Fermi surface intensity calculated from Eq. 3.15 and N_F is the number of k -points on the Fermi surface. We expect peaks in the autocorrelation where nesting features in $I(\mathbf{k})$ and $I(\mathbf{k} + \mathbf{q} + \mathbf{g})$ overlap.

The autocorrelations of the 0 and 1100 K Fermi surfaces are plotted in the bottom panel of Fig. 3.6. A sharp peak is observed in the 0 K autocorrelation at $\mathbf{q} = [0.24, 0, 0]$ along the Γ -H direction, approximately lining up with the location of the peak in the electron-phonon coupling strength $\lambda_{\mathbf{q}\nu}$. Similar sharp peaks are observed near the Γ point along the Γ -N and Γ -P directions and at the N symmetry point, approximately lining up with the peaks in $\lambda_{\mathbf{q}\nu}$.

We still observe a peak at the N symmetry point in the 1100 K Fermi surface autocorrelation. We see an additional peak at the H symmetry point. No peak is observed at $\mathbf{q} = [0.24, 0, 0]$. None of the peaks in the 1100 K autocorrelation are as narrow as the 0 K peaks, and the peaks barely stand out from the baseline. The small population of broad peaks in the 1100 K autocorrelation may indicate that electron-phonon interactions are reduced, as nesting features are smeared out with the thermal broadening observed in Fig. 3.5.

Temperature Dependence of Electron-Phonon Interactions

We can get a closer look at how changes in the Fermi surface with temperature affect electron-phonon interactions by calculating the density of specific spanning vectors $D_\nu(\mathbf{q})$ at 0 and 1100 K. By comparing the spanning vector densities of phonon modes between the two temperatures, we can see if electron-phonon interactions are strengthened or weakened with temperature. We can also see if the spanning vector densities and electron-phonon interactions are impacted by the thermally-driven ETT observed in Fig. 3.5.

Our calculation of the spanning vector density sums over all possible electron-phonon scattering processes that may occur in our window from -0.50 to $+0.50$ eV with respect to the Fermi energy, which is an overestimation of the thermal layer

(TL):

$$D_\nu(\mathbf{q}) = \frac{1}{N_F} \sum_{\substack{\mathbf{k} \\ \varepsilon \in \text{TL} \\ \mathbf{q}_i \in S\mathbf{q}}} [F(\mathbf{k}, \varepsilon)F(\mathbf{k} + \mathbf{q}_i + \mathbf{g}, \varepsilon + \hbar\omega_{\mathbf{q}\nu}) + F(\mathbf{k} + \mathbf{q}_i + \mathbf{g}, \varepsilon)F(\mathbf{k}, \varepsilon + \hbar\omega_{\mathbf{q}\nu})] \\ \times [f(\varepsilon, T)(1 - f(\varepsilon + \hbar\omega_{\mathbf{q}\nu}, T)) + f(\varepsilon + \hbar\omega_{\mathbf{q}\nu}, T)(1 - f(\varepsilon, T))], \quad (3.17)$$

where \mathbf{q}_i is a vector related to \mathbf{q} by symmetry. We are treating the Fermi surface F as a function of both \mathbf{k} and energy ε to take the conservation of energy into account.

In the 0 K limit, the Fermi surface function F is either a nonzero integer or zero, and the thermal layer is localized at $E = E_F$. At 0 K, the sum in Eq. 3.17 would simply be a count of the number of spanning vectors \mathbf{q} on the Fermi surface. At finite temperatures, the Fermi surface function F is interpreted as the probability of the presence of an electronic state at $(\mathbf{k}, \varepsilon)$ as a consequence of electronic broadening from thermal atomic displacements. According to the Fermi-Dirac distribution terms in the second bracket in Eq. 3.17, electrons at energies far from the Fermi level are less likely to be involved in scattering processes due to low occupation or unoccupation probabilities. This is what is also described by the derivative of the Fermi-Dirac distribution.

We can gather insights about nesting features by looking at the summands $D_\nu^{(\mathbf{k})}(\mathbf{q})$:

$$D_\nu(\mathbf{q}) = \sum_{\mathbf{k}} D_\nu^{(\mathbf{k})}(\mathbf{q}). \quad (3.18)$$

The nesting strength $D_\nu^{(\mathbf{k})}(\mathbf{q})$ is the density of spanning vectors \mathbf{q} for the electronic state at wavevector \mathbf{k} . Nesting features are composed of electronic states with high values of $D_\nu^{(\mathbf{k})}(\mathbf{q})$. Fig. 3.7 shows the nesting strengths $D_\nu^{(\mathbf{k})}(\mathbf{q})$ for three phonon modes at 0 and 1100 K: the transverse phonon mode at $\mathbf{q} = [0.24, 0, 0]$ (subfigures a and b), the longitudinal N phonon mode (subfigures c and d), and the H phonon mode (subfigures e and f).

We can attribute the high 0 K electron-phonon coupling strength $\lambda_{\mathbf{q}\nu}$ for the transverse phonon mode at $\mathbf{q} = [0.24, 0, 0]$ to the high density of vectors spanning the flat features on the hole-ellipsoids (Fig. 3.7(a)). These flat features are the previously identified nesting features associated with the Kohn anomaly along Γ -H for vanadium [96] and contribute to the high superconducting transition temperature T_c of vanadium [20, 21].

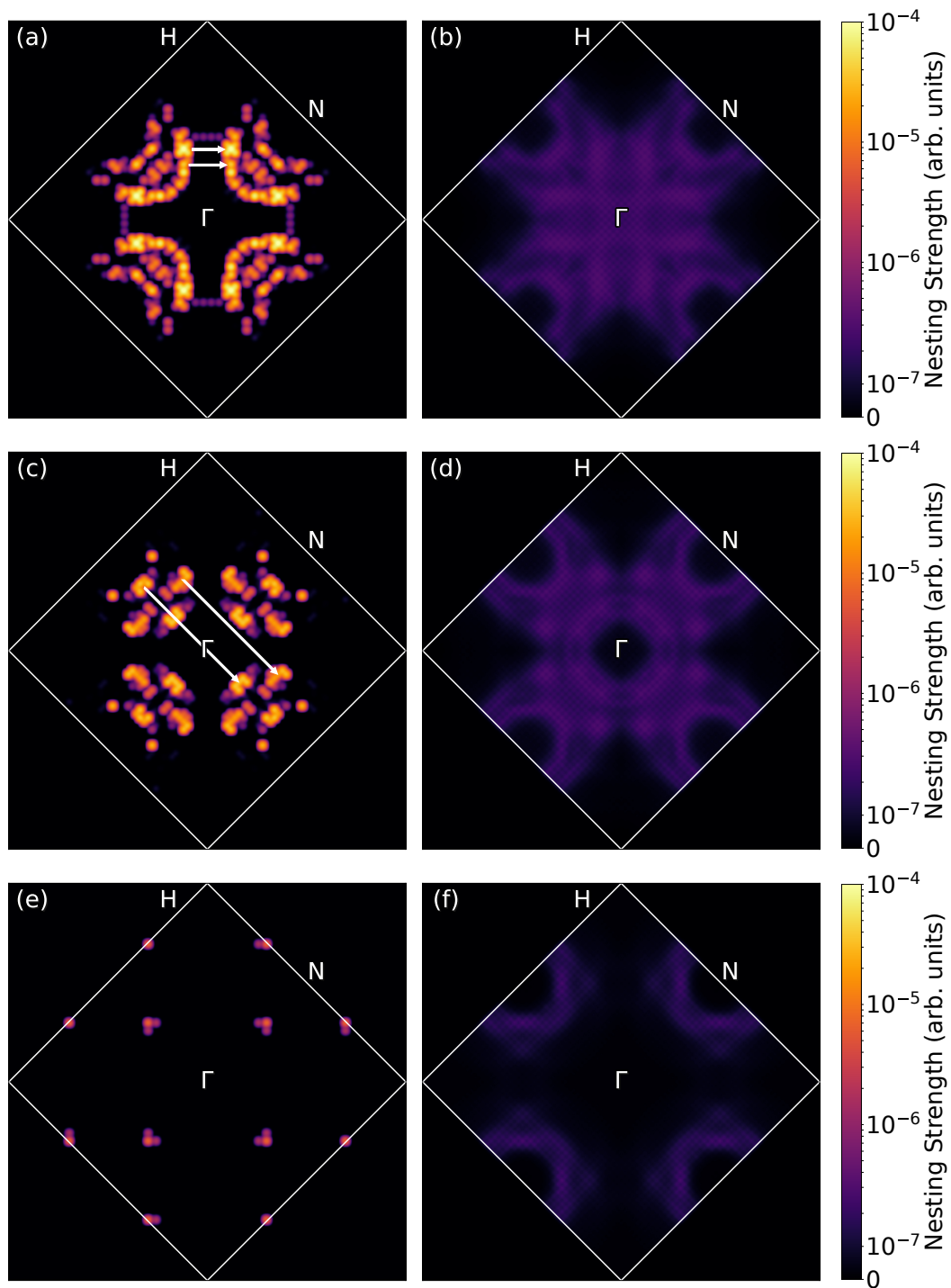


Figure 3.7: $\{100\}$ cross sections of the Fermi surface nesting strengths of vanadium for the transverse phonon mode at $\mathbf{q} = [0.24, 0, 0]$ at (a) 0 K and (b) 1100 K, the longitudinal N phonon mode at (c) 0 K and (d) 1100 K, and the H phonon mode at (e) 0 K and (f) 1100 K. Sample $[0.24, 0, 0]$ and $[0.5, 0.5, 0]$ spanning vectors are shown in (a) and (c).

We can attribute the peak in $\lambda_{\mathbf{q}\nu}$ for the longitudinal phonon mode at N to the high density of spanning vectors spanning the hole-ellipsoids and the distorted octahedron (Fig. 3.7(c)). The crossover of the longitudinal and transverse acoustic modes at N can be attributed to the interaction of this phonon mode with these electronic states.

No notable peaks were observed in the 0 K values of $\lambda_{\mathbf{q}\nu}$ and Fermi surface auto-correlation for the H phonon mode. There are almost no nesting features for the $\mathbf{q} = [1, 0, 0]$ spanning vector (Fig. 3.7(e)), such that no 0 K electron-phonon interaction is observed for the H phonon mode. We observe that the vector $\mathbf{q} = [1, 0, 0]$ spans more features of the Fermi surface at 1100 K, but these features make up only a small fraction of the number of k -points making up the Fermi surface at 1100 K. These features also display low nesting strengths, such that the spanning vector density $D_\nu(\mathbf{q})$ for this phonon mode is actually *reduced* by a factor of 1.731 from 0 to 1100 K. This is consistent with our observation that this phonon mode softens quasiharmonically with temperature.

The $[0.24, 0, 0]$ and $[0.5, 0.5, 0]$ vectors span several more k -points in the Fermi surface at 1100 K than at 0 K, as shown in Fig. 3.7(b) and (d). The nesting strengths for these phonon modes are also low. The spanning vector density for the transverse mode at $[0.24, 0, 0]$ is reduced by a factor of 2.364 from 0 to 1100 K, and the spanning vector density for the longitudinal N phonon mode is reduced by a factor of 3.094 from 0 to 1100 K.

It appears that the reduction of the spanning vector density for the transverse mode at $[0.24, 0, 0]$ is not as severe as the reduction for the longitudinal N phonon mode owing to the introduction of additional nesting features from the thermally-driven ETT. The thermally-driven ETT does not counteract the reduction in the electron-phonon interaction strength for this phonon mode. The $[0.5, 0.5, 0]$ vector does not span any of the new electronic states at the Γ point, such that the thermally-driven ETT has no impact on the thermal evolution of the longitudinal N phonon mode. We had previously hypothesized that this thermally-driven ETT would counteract the phonon thermal stiffening, explaining the apparent saturation of the adiabatic EPI observed by Delaire *et al* [10] and the softening of the longitudinal peak and the average phonon energies past 750 K. We attribute the stiffening of the longitudinal N phonon mode only to the weakening of the low-temperature EPI owing to the thermal smearing of the Fermi surface. This stiffening slows down with temperature as it is opposed by softening from thermal expansion.

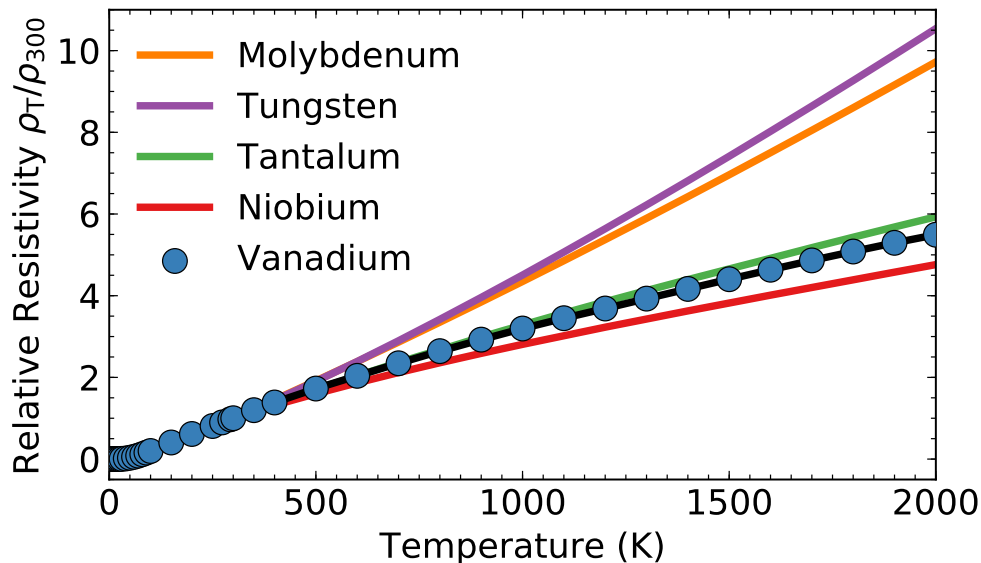


Figure 3.8: The electrical resistivities of bcc transition metals relative to their 300 K values. The plotted data are from measurements on high-purity samples.

Table 3.1: Electron-phonon interaction parameters and superconducting transition temperatures of nonmagnetic bcc transition metals.

Element	λ	T_c (K)
W	0.26 [20, 124]	0.015
Mo	0.199-0.41 [20, 125]	0.92
Ta	0.6923-0.88 [126–128]	4.47
V	0.7-0.82 [10, 124, 129]	5.3
Nb	0.867-1.22 [125, 130]	9.25

Electrical Resistivity

The thermal reduction of the electron-phonon interaction in vanadium could affect the temperature dependence of the electrical resistivity ρ , at least the resistivity from electron-phonon scattering ρ_T . We are also interested in comparing the resistivities ρ_T of vanadium to other nonmagnetic bcc transition metals, as these metals may display different electron-phonon interaction properties.

Fig. 3.8 shows the values for the electrical resistivity relative to their room temperature values for nonmagnetic bcc transition metals. The resistivity values for molybdenum, tungsten, tantalum, and vanadium were recommended by Desai *et al.* and were derived from experimental measurements of samples with 99.9% or higher purity (Ref. [131, 132] and references therein). Low temperature values of the electrical resistivity of high-purity niobium were obtained from measure-

ments by Webb [133] while high temperature values of the electrical resistivity of high-purity niobium were obtained from measurements by Abraham and Deviot, Peletskii, and Maglić *et al.* [134–136]

If electrons in the nonmagnetic bcc metals were described by the free electron model, the relative resistivities would change linearly with temperature past the Debye temperature. We see in Fig. 3.8 that the five nonmagnetic bcc metals deviate from the expected linear relationship $\rho_T \propto T$. The electrical resistivities of the group 6 transition metals molybdenum and tungsten increase with positive curvature at elevated temperatures, meaning electrons are increasingly scattered by phonons with temperature. The electrical resistivities of the group 5 transition metals tantalum, vanadium, and niobium increase with negative curvature at elevated temperatures. While the electrical resistivity increases with temperature, the electron scattering rate from phonons is suppressed. This is consistent with the reduction of electron-phonon interactions with temperature in vanadium. Fig. 3.8 would lead us to believe that niobium and tantalum show similar thermal trends in electron-phonon interactions. A thermal smearing of the Fermi surface nesting features can explain the stiffening of the longitudinal N phonon mode in niobium reported by Güthoff *et al.* [137].

Molybdenum and tungsten display weak low temperature electron-phonon interactions, as evidenced by their small electron-phonon interaction parameters λ . The low electron-phonon interaction strengths in these elements contribute to their low superconducting transition temperatures T_c , consistent with the McMillan theory of strong-coupled superconductors [20, 21]. Tantalum, vanadium, and niobium display strong low temperature electron-phonon interactions that lead to superconductivity, as evidenced by how their electron-phonon interaction parameters λ are close to or over unity, and how they display high superconducting transition temperatures.

The curvature of the thermal evolution of electrical resistivities of high-purity bcc transition metals follows the low temperature electron-phonon interaction strength. The rate of change $\frac{\partial \rho_T}{\partial T}$ of the relative electrical resistivity with temperature decreases with increasing low temperature electron-phonon interaction strengths and superconducting transition temperatures. The stronger the electron-phonon interaction at low temperatures, the more dramatic the thermal increase in electrical conductivity as the adiabatic EPI is lost.

3.5 Conclusions

The nonlinear thermal stiffening of phonons in vanadium previously measured with inelastic neutron scattering was reproduced with first-principles calculations. The Fermi surface of vanadium was calculated at 0 K and high temperatures through band unfolding procedures. The sharp features of the Fermi surface at low temperatures were drastically smeared with temperature from atomic displacements and thermal excitations of electrons. The overall weakening of the electron-phonon interactions in vanadium is primarily attributed to this thermal smearing. There is a thermally-driven electronic topological transition near the Γ point, but the atomic displacements smear its effectiveness. The phonon stiffening from this reduction in the EPI is counteracted by quasiharmonic softening at high temperatures.

The negative curvature of the electrical resistivity of vanadium at elevated temperatures follows the reduction of electron-phonon interactions with temperatures. Based on their negative curvatures in electrical resistivity, we suggest that the bcc nonmagnetic transition metals niobium and tantalum display similar changes in their electronic structure and electron-phonon interactions with temperature to vanadium.

*Chapter 4*TEMPERATURE DEPENDENCE OF PHONONS IN Pd_3Fe
THROUGH THE CURIE TEMPERATURE**4.1 Introduction**

Advances in the design of magnetic materials are enabled by understanding how their properties depend on the external conditions of temperature, pressure, and magnetic field. In particular, it is important to understand their thermodynamic properties over a range of temperatures. This requires modeling a magnetic material not only in its ground state at 0 K, but also in its magnetically disordered states at finite temperatures.

Progress has been made in first-principles simulations of magnetic disorder in materials [138]. Recent approaches to modeling the paramagnetic state of magnetic materials include disordered local moment molecular dynamics (DLM-MD) [139, 140], spin-space averaging [33, 141–143], and spin dynamics [144–146]. With such advances, a computational study accounting for the interaction of the magnetic and atomic degrees of freedom, which has been demonstrated to provide a more complete calculation of the Gibbs free energy of magnetic materials [7], is now within reach. In the present study of the thermal excitations in Pd_3Fe , magnetic disorder is included in the finite temperature calculations of vibrational thermodynamic properties.

Fe–Pd alloys have been a subject of numerous studies owing to their magnetic and mechanical behavior. Properties of interest include a martensitic transformation in Fe-rich alloys [143, 147, 148], noncollinear magnetic structures [149–152], and Invar behavior [153]. Pd_3Fe , a ferromagnetic metallic compound with an fcc-based $L1_2$ structure and a Curie temperature of approximately 500 K [154], exhibits Invar behavior under an applied pressure [155]. This compound also exhibits an anomalous dependence of phonon frequencies and volume with pressure as a consequence of a magnetic transition [151, 156]. In this present work, we investigate this interaction between lattice dynamics and magnetic excitations at temperatures through the Curie temperature, using nuclear resonant inelastic x-ray scattering and first-principles calculations.

4.2 Methods

Experiment

Measurements were performed on the $L1_2$ -ordered $\text{Pd}_3^{57}\text{Fe}$ sample used in a pressure-induced Invar experiment [155], which was prepared by arc-melting Pd of 99.95% purity and ^{57}Fe of 95.38% isotopic enrichment before being cold rolled to a thickness of 25 μm . This ordered sample was further annealed with a heat treatment at 873 K for 18 hours under vacuum, 773 K for 54 hours, and subsequent cooling to 293 K over 2 hours. X-ray diffraction confirmed the $L1_2$ structure and long-range order, and Mössbauer spectroscopy confirmed the short-range order (shown in the Supporting Information).

Nuclear resonant inelastic x-ray scattering (NRIXS) measurements were performed on $\text{Pd}_3^{57}\text{Fe}$ at seven temperatures from 298 to 786 K. NRIXS is a low background technique that provides direct access to the phonon partial density of states (pDOS) of ^{57}Fe [157, 158]. Measurements were performed at beamline 16ID-D of the Advanced Photon Source at Argonne National Laboratory. The synchrotron flashes had durations of 70 ps and were separated by 153 ns. Electronic scattering occurs within femtoseconds of the pulse arrival at the sample. The relatively long lifetime of the nuclear resonant state ($\tau = 141$ ns) allowed for a clear separation of the prompt electronic scattering from the delayed resonant scattering.

The $\text{Pd}_3^{57}\text{Fe}$ foil sample was held in vacuum under active evacuation in a resistive heating furnace with a kapton window for x-ray transmission. Errors in the values of the temperature ranged from ± 10 to ± 27 K. The ambiguity comes from comparing the furnace thermocouple measurements to NRIXS-derived detailed balance temperature calculations following procedure described in the literature [80, 159].

An avalanche photodiode was positioned at approximately 90° from the incident beam to collect incoherently reradiated photons. The energy was scanned from -80 to $+80$ meV around 14.413 keV, the resonant energy of ^{57}Fe , in several scans that were combined for final analysis. The energy resolution of all NRIXS measurements was measured to be 2.2 meV (FWHM) at the elastic line. The PHOENIX software package was used to extract the ^{57}Fe pDOS from the measured NRIXS spectra [80].

Nuclear forward scattering (NFS) measurements were collected immediately prior to NRIXS scans. The NFS spectra provide a measure of the magnetic state of $\text{Pd}_3^{57}\text{Fe}$, using an avalanche photodiode in the path of the forward-scattered x-ray beam to measure the transmitted intensity as a function of time.

In situ synchrotron x-ray diffraction (XRD) measurements were performed concurrently with the NRIXS and NFS measurements with the same monochromatic beam of 14.413 keV x-rays and a Mar CCD detector plate. Results from synchrotron XRD were used to obtain lattice parameters for the quasiharmonic (QH) approximation of the Fe pDOS.

Computational: Phonon Calculation

Phonon frequencies at elevated temperatures were calculated with the s-TDEP method [11, 102, 103, 106], as described in Chapter 3. In brief, first-principles calculations were performed on supercells of thermally-displaced atoms generated by stochastic sampling of a canonical ensemble. The thermal displacements were calculated with phonon populations and polarizations from short *ab initio* molecular dynamics (AIMD) simulations. The ensemble of calculated forces and energies were used to fit an effective potential with a model Hamiltonian

$$\mathcal{H} = U_0 + \sum_i \frac{\mathbf{p}_i^2}{2m_i} + \frac{1}{2!} \sum_{ij\alpha\beta} \Phi_{ij}^{\alpha\beta} u_i^\alpha u_j^\beta + \frac{1}{3!} \sum_{ijk\alpha\beta\gamma} \Phi_{ijk}^{\alpha\beta\gamma} u_i^\alpha u_j^\beta u_k^\gamma, \quad (4.1)$$

where \mathbf{p}_i and u_i are the momentum and displacement of atom i , respectively, and $\alpha\beta\gamma$ are Cartesian components. The temperature-dependent U_0 is a fit parameter for the baseline of the potential energy surface [102]. The quadratic force constants Φ_{ij} from the thermally-displaced atoms capture nonharmonic effects such as magnon-phonon interactions at a given temperature, and are used to calculate phonon frequencies ω_s shifted by these effects [102], where s is an index for phonon modes. The cubic force constants Φ_{ijk} capture phonon-phonon interactions (PPI) that contribute to the broadening and additional shifts of phonon modes [103].

The *ab initio* spin-polarized density functional theory (DFT) calculations with spin-orbit coupling were performed with the projector augmented wave [112] formalism as implemented in VASP [65, 66]. All calculations used a $3 \times 3 \times 3$ supercell with 108 atoms, a $2 \times 2 \times 2$ Monkhorst-Pack [87] k -point grid, and a plane wave energy cutoff of 520 eV. The exchange-correlation energy was calculated with the Perdew-Burke-Ernzerhof (PBE) functional [63]. It was observed from calculations and from past experiments [160–162] that the magnetic moment of Pd atoms in Pd₃Fe is small compared to that of Fe atoms. The Pd moments were approximated as zero.

At a given temperature, the forces and energies of 25 stochastically-generated supercells were calculated at five volumes within -2.5 to $+5\%$ around the 0 K equilibrium volume through three iterations of the s-TDEP procedure. For each volume, the

Helmholtz free energy $F(V, T)$ was calculated:

$$F(V, T) = U_0(V, T) + F_{\text{vib}}(V, T). \quad (4.2)$$

$U_0(V, T)$ is the baseline from Eq. 4.1. $F_{\text{vib}}(V, T)$ is from lattice vibrations:

$$F_{\text{vib}} = \int_0^\infty g(\omega) \left\{ k_B T \ln \left[1 - \exp \left(-\frac{\hbar\omega}{k_B T} \right) \right] + \frac{\hbar\omega}{2} \right\} d\omega, \quad (4.3)$$

where $g(\omega)$ is the phonon density of states calculated from the phonons in the first Brillouin zone. At a given temperature, the equilibrium volume V_T was obtained through the minimization of the Helmholtz free energy $F(T, V)$. The force constants were then interpolated to this volume, giving us phonon frequencies that capture volume expansion and temperature-dependent nonharmonic effects.

We then corrected our phonon frequencies $\omega_s(T, V_T)$ by calculating the linewidths Γ_s and shifts Δ_s arising from anharmonicity, or phonon-phonon interactions. This required the many-body perturbation calculation of the real and imaginary parts of the phonon self-energy [70, 113] $\Sigma(\Omega) = \Delta(\Omega) + i\Gamma(\Omega)$, where $E = \hbar\Omega$ is a probing energy. The imaginary component $\Gamma(\Omega)$ is

$$\begin{aligned} \Gamma_s(\Omega) &= \frac{\hbar\pi}{16} \sum_{s's''} |\Phi_{ss's''}|^2 \{ (n_{s'} + n_{s''} + 1) \\ &\quad \times \delta(\Omega - \omega_{s'} - \omega_{s''}) + (n_{s'} - n_{s''}) \\ &\quad \times [\delta(\Omega - \omega_{s'} + \omega_{s''}) - \delta(\Omega + \omega_{s'} - \omega_{s''})] \}, \end{aligned} \quad (4.4)$$

and the real component is obtained by a Kramers-Kronig transformation:

$$\Delta(\Omega) = \frac{1}{\pi} \int \frac{\Gamma(\omega)}{\omega - \Omega} d\omega. \quad (4.5)$$

The imaginary component of the self-energy is a sum over all possible three-phonon interactions, where $\Phi_{ss's''}$ is the three-phonon matrix element determined from the cubic force constants Φ_{ijk} . $\Gamma(\Omega)$ and $\Delta(\Omega)$ were calculated with a $36 \times 36 \times 36$ q -grid.

Anharmonic phonon DOS curves were calculated with the real and imaginary parts of the phonon self-energy:

$$g_{\text{anh}}(\omega) = \sum_s \frac{2\omega_s \Gamma_s(\omega)}{[\omega^2 - \omega_s^2 - 2\omega_s \Delta_s(\omega)]^2 + 4\omega_s^2 \Gamma_s^2(\omega)}. \quad (4.6)$$

This procedure was implemented to calculate two sets of phonon dispersions and DOS: for Pd₃Fe maintaining complete ferromagnetic order at 0, 300, 480, 600, and 800 K (illustrated with Fig. 4.1(a)), and for Pd₃Fe with increasing magnetic disorder at 300, 480, and 800 K (illustrated with Fig. 4.1(b)). Pd₃Fe is expected to be completely ferromagnetic only at 0 K. The calculations of the completely ferromagnetic Pd₃Fe at nonzero temperatures were performed for comparison with computations with magnetic disorder.

For comparison with the s-TDEP phonon spectra, the phonon energies predicted by the quasiharmonic (QH) approximation were calculated by interpolation of the 0 K quadratic force constants to volumes obtained from the minimization of the free energy. This “QH DFT model” assumes that the only temperature dependence in Eq. 4.2 and 4.3 is from volume expansion and the Planck distribution. The “QH DFT model” excludes the anharmonic corrections provided by Eqs. 4.4 and 4.5.

Computational: Magnetic Disorder

The magnetic disorder from thermal fluctuations was modeled with special quasirandom structures (SQSs) [163] of noncollinear Fe magnetic moments. The magnetic SQSs mimic the most relevant local correlation functions of random magnetic structures [164], where the correlation function of the coordination shell α is

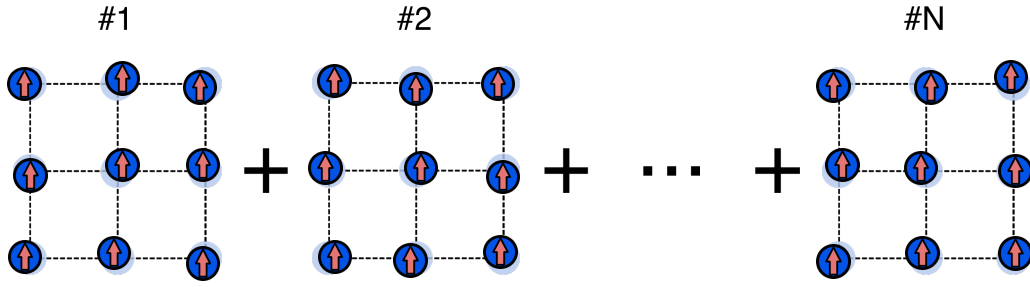
$$\Pi_\alpha = \frac{1}{N_\alpha} \sum_{i,j \in \alpha} \mathbf{e}_i \cdot \mathbf{e}_j, \quad (4.7)$$

where $\mathbf{e}_i = \mathbf{m}_i / \|\mathbf{m}_i\|$ is a unit vector in the direction of the magnetic moment \mathbf{m}_i on site i , and N_α is the number of magnetic moment pairs in the coordination shell α . This use of SQSs with noncollinear Fe magnetic moments is related to the disordered local moment (DLM) model, where magnetic disorder is modeled with randomly oriented local magnetic moments [165–170].

A histogram of magnetic SQSs was generated by simulated annealing, where Fe magnetic moments were flipped into random orientations until the local correlation functions matched target correlation functions. These bins were of increasing levels of magnetic disorder, from completely ordered to completely disordered. In the same bin of the histogram, the set of magnetic SQSs $\{\lambda\}$ were equivalent in their correlation functions.

All correlation functions of magnetic SQSs modeling complete ferromagnetic order equaled 1 ($\Pi_\alpha = 1, \forall \alpha$), and the resulting Fe magnetic moments were aligned in the same direction. All correlation functions of magnetic SQSs modeling complete

(a) 0 K, Ferromagnetic



(b) 800 K, Paramagnetic

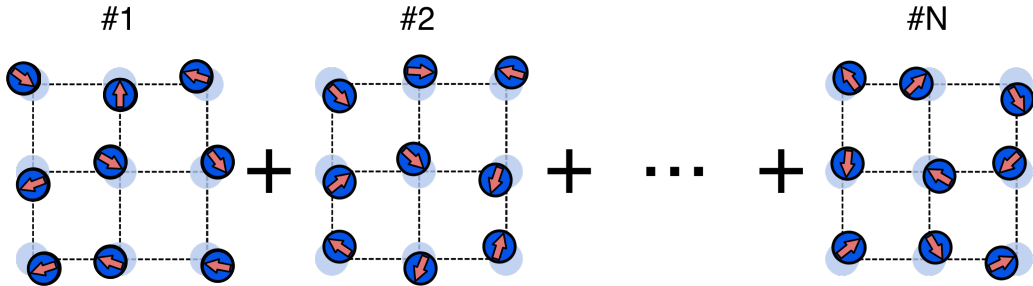


Figure 4.1: (a) Schematic of supercells with Fe atoms (dark blue) stochastically displaced from their ideal positions (light blue) in the 0 K ferromagnetic calculations, where the magnetic moments (red arrows) are aligned in the same direction. (b) Supercells with randomly oriented magnetic moments and stochastically displaced Fe atoms in the 800 K paramagnetic calculations. Each set of randomly oriented magnetic moments is a magnetic special quasirandom structure (SQS). Pd atoms are not shown for this illustration.

magnetic disorder equaled 0 ($\Pi_\alpha = 0, \forall \alpha$), and the resulting Fe magnetic moments were randomly oriented. The correlation functions for magnetic SQSs from a bin that was between complete order and complete disorder had values between 0 and 1. For a given bin, the generated magnetic SQSs had an averaged normalized magnetization

$$\langle M/M_0 \rangle_{\text{SQS}} = \frac{1}{N_m} \left\| \sum_{\lambda} \left(\sum_i \mathbf{m}_i \right) \right\|, \quad (4.8)$$

where N_m is a normalization constant.

For the phonon calculations of Pd_3Fe with increasing magnetic disorder, we coupled the s-TDEP procedure with these magnetic SQSs. For a given temperature T , 25 stochastically sampled supercells $\{\kappa\}$ with thermal atomic displacements characteristic of T were generated. Separately, 25 magnetic SQSs $\{\lambda\}$ were selected from a bin where the SQSs have an averaged normalized magnetization $\langle M/M_0 \rangle_{\text{SQS}}$

approximately equal to the normalized magnetization $M(T)/M_0$ expected at temperature T . A spin-polarized DFT calculation was performed on a supercell κ paired with a magnetic SQS λ . The forces from these spin-polarized DFT calculations on the ensemble of SQS-supercell (κ, λ) pairs, illustrated in Fig. 4.1(b), are used to obtain force constants used in the calculation of phonon dispersions and DOS, as described previously. This computational method can be considered to be a stochastic ensemble-averaged variant of disordered local moments molecular dynamics (DLM-MD) [139, 140] with local spin correlations.

For the calculations at 800 K, the magnetic structure was treated as a random distribution of magnetic moments characterized by the vanishing of the spin correlation functions ($\Pi_\alpha = 0, \forall \alpha$) so that the average magnetization $\langle M \rangle_{\text{SQS}}$ is zero, in accordance with the DLM model. The force constants calculated at 800 K were interpolated to a volume that minimized a modified Helmholtz free energy $F(T, V)$

$$F(T, V) = U_0(T, V) + F_{\text{vib}}(T, V) + F_{\text{mag}}(T, V), \quad (4.9)$$

where $F_{\text{mag}}(T, V)$ is the magnetic free energy. Because there is no exact formulation for the magnetic free energy, this free energy was approximated with a mean-field term

$$F_{\text{mag}}(T, V) = -TS_{\text{mag}} = -k_{\text{B}}T \ln(\langle m(V) \rangle + 1), \quad (4.10)$$

where $\langle m(V) \rangle$ is the average magnitude of the magnetic moments in units of μ_{B} . The magnetic entropy S_{mag} is the maximum orientational disorder of magnetic moments in the paramagnetic state for systems with local magnetic moments. This approach is widely used to describe the magnetic entropy of paramagnetic systems [142, 171].

For calculations at 300 and 480 K, the magnetic structures were sampled so the averaged normalized magnetizations $\langle M/M_0 \rangle_{\text{SQS}}$ were approximately equal to normalized hyperfine fields $H(T)/H_0$ obtained from Mössbauer spectroscopy measurements performed in this study and by Longworth [154], as seen in Fig. 4.3. Because there is no reliable method for calculating the magnetic free energy of Pd_3Fe at intermediate temperatures, force constants were calculated at volumes obtained by scaling the volume calculated at 800 K by volumes obtained from synchrotron x-ray diffraction measurements.

4.3 Results

Nuclear Forward Scattering

The NFS spectra measured from the $\text{Pd}_3^{57}\text{Fe}$ sample are shown in Fig. 4.2. The NFS spectrum at 298 K exhibits a clear magnetic beat pattern expected from a

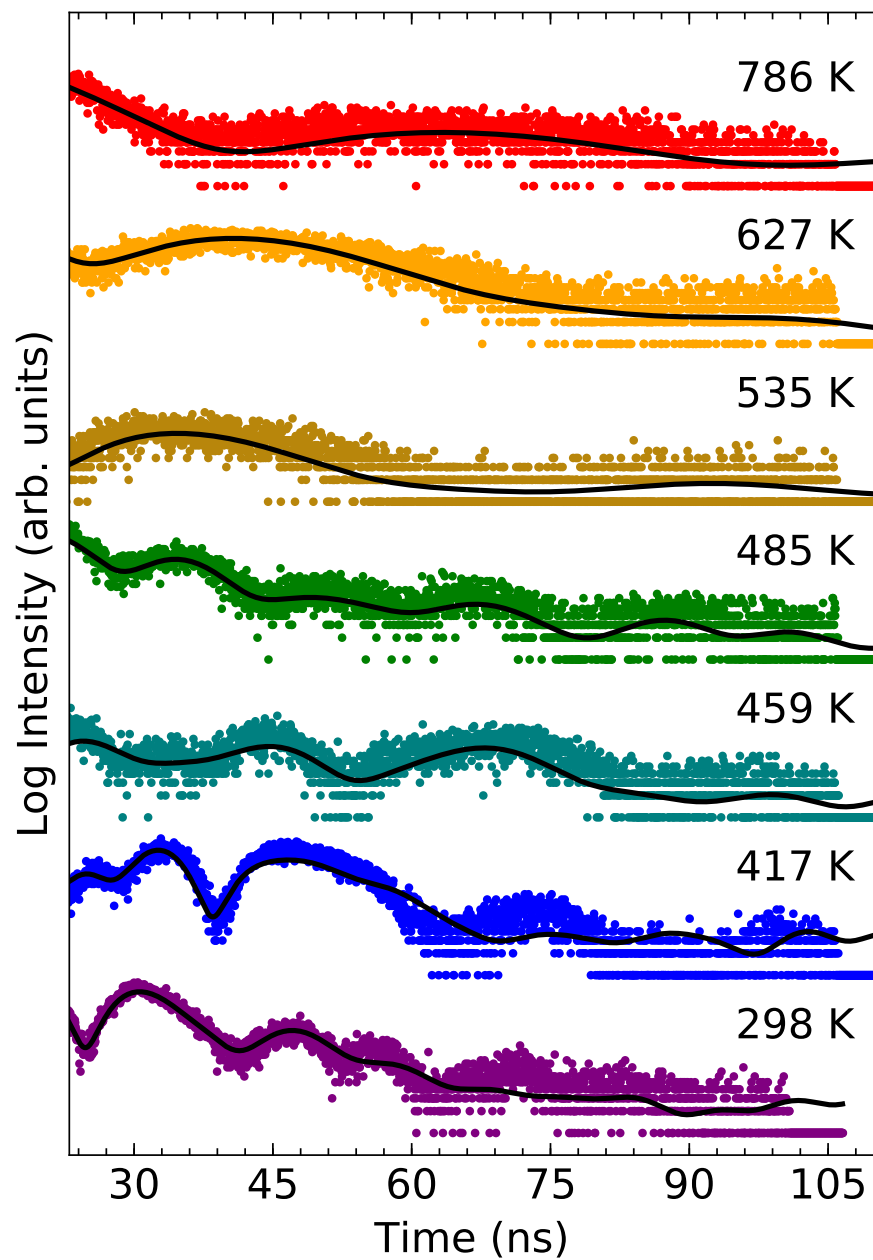


Figure 4.2: The ^{57}Fe nuclear forward scattering spectra from $L1_2$ -ordered Pd_3Fe at several temperatures. The fits (black curves) overlay experimental data (points). The spectra are displayed using a log scale, and offset for clarity.

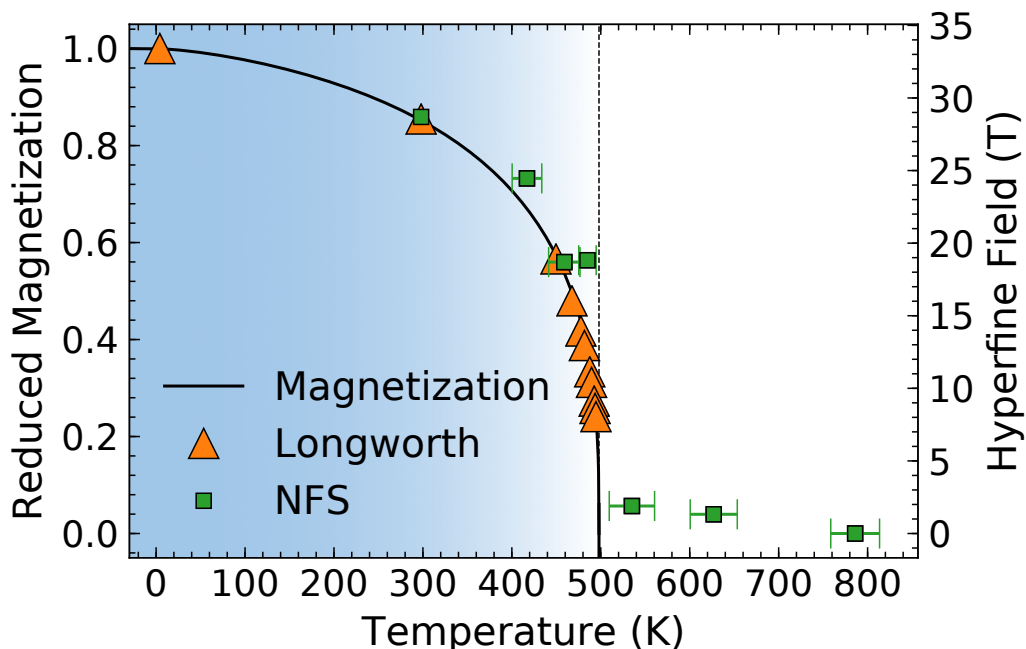


Figure 4.3: The magnetization curve of Pd_3Fe obtained from an empirical fit of a magnetic shape function [172] to hyperfine magnetic fields obtained from the NFS spectra in this study (green) and Mössbauer data from a study by Longworth [154] (orange). The shaded region indicates the temperature range where Pd_3Fe exhibits ferromagnetic order.

magnetically-ordered material, similar to a previous NFS measurement of $\text{Pd}_3^{57}\text{Fe}$ at ambient conditions [155]. The amplitudes and periods of the magnetic beats diminish with temperature, and the magnetic beats disappear above 485 K, consistent with a second-order phase transition in which the magnetic order continuously decreases through the Curie temperature. The remaining beats above 485 K are from the thickness of the sample.

A quantitative analysis of the NFS spectra was performed with the software package CONUSS [80, 173]. The refined fits overlay the experimental spectra in Fig. 4.2. Parameters extracted from these fits include the hyperfine field H , shown together with the magnetization of Pd_3Fe in Fig. 4.3, and the Lamb-Mössbauer factor, shown in the Supporting Information. The decrease in the hyperfine field of $\text{Pd}_3^{57}\text{Fe}$ with temperature is in agreement with the hyperfine fields measured by Longworth [154], and the decrease in this quantity with temperature tracks the decrease in magnetization through the Curie temperature.

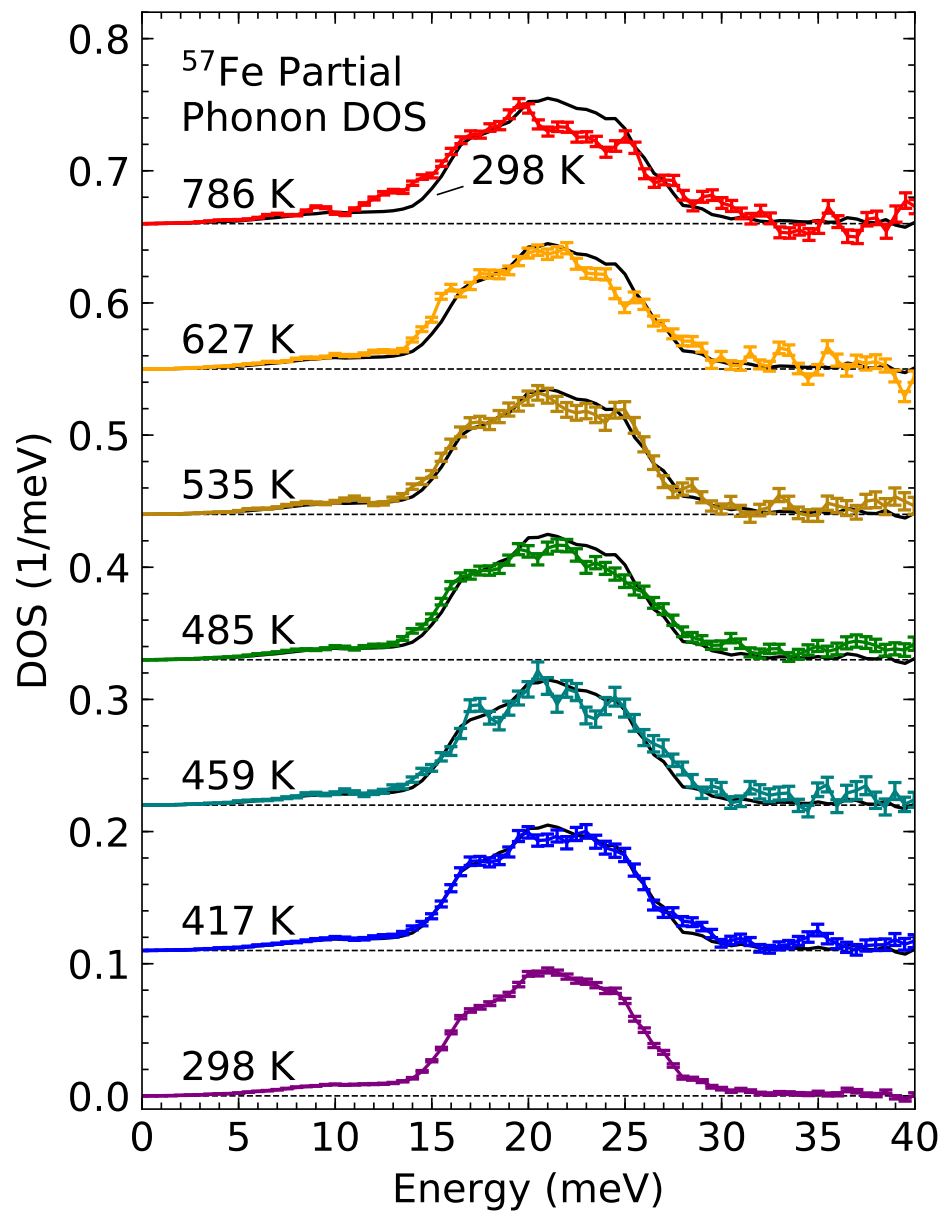


Figure 4.4: The normalized ^{57}Fe pDOS extracted from NRIXS measurements at various temperatures. The spectra from measurements above 298 K are offset and compared with the 298 K pDOS (black curve). Error bars are from counting statistics.

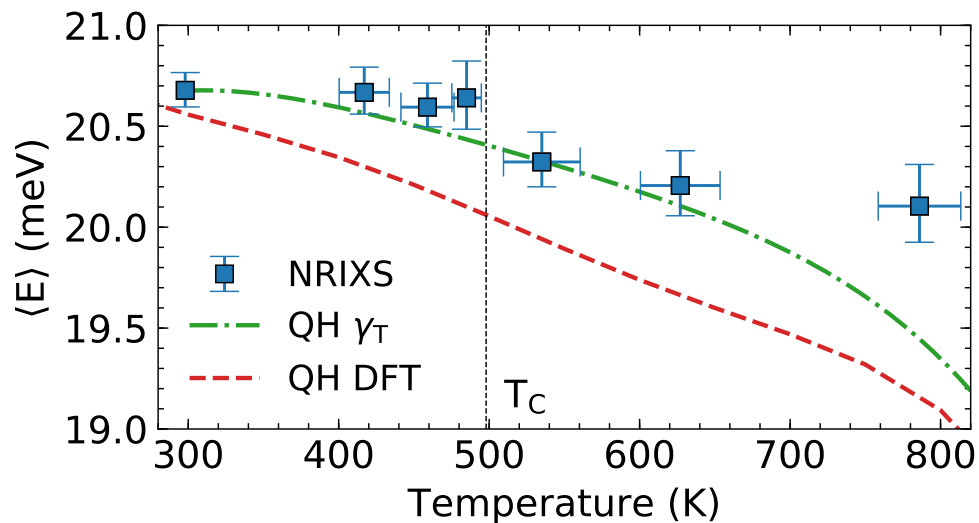


Figure 4.5: Average energies of the Fe pDOS from NRIXS measurements (blue points) plotted with the average Fe phonon energies from the Grüneisen parameter model (green line) and the QH DFT model (red line).

Phonons

The ^{57}Fe pDOS curves measured from the $\text{Pd}_3^{57}\text{Fe}$ sample are shown in Fig. 4.4. The pDOS do not show significant energy shifts below the Curie temperature. The phonons begin to show a small but significant thermal softening beyond the Curie temperature, made apparent when the 627 and 786 K pDOS are compared with the 298 K curve in Fig. 4.4. This trend is seen more clearly with the average Fe phonon energies calculated from the ^{57}Fe pDOS, shown in Fig. 4.5. These phonon shifts are similar to the experimental trends observed in the ferromagnetic cementite through the Curie temperature [31]. It is noted that the quality of the high temperature ^{57}Fe pDOS at 786 K was impacted by reduced counting statistics.

The phonon DOS curves calculated at 0, 300, 480, and 800 K with s-TDEP are shown in Fig. 4.6. The phonon DOS curves soften with temperature, although features like the peak at 21 meV in the Fe pDOS or at 25 meV in the Pd pDOS do not soften until the Curie temperature. The s-TDEP phonon DOS curves also exhibit a thermal broadening that is most prominent at 800 K, indicative of phonon-phonon interactions (PPI) [22, 70, 113, 174].

Figure 4.7 shows thermal trends from experiment (panel a) and computation (panel b). The difference spectra shown in both panels are in reasonable agreement with each other, indicating that the NRIXS measurements and s-TDEP calculations capture similar thermal trends in Pd_3Fe .

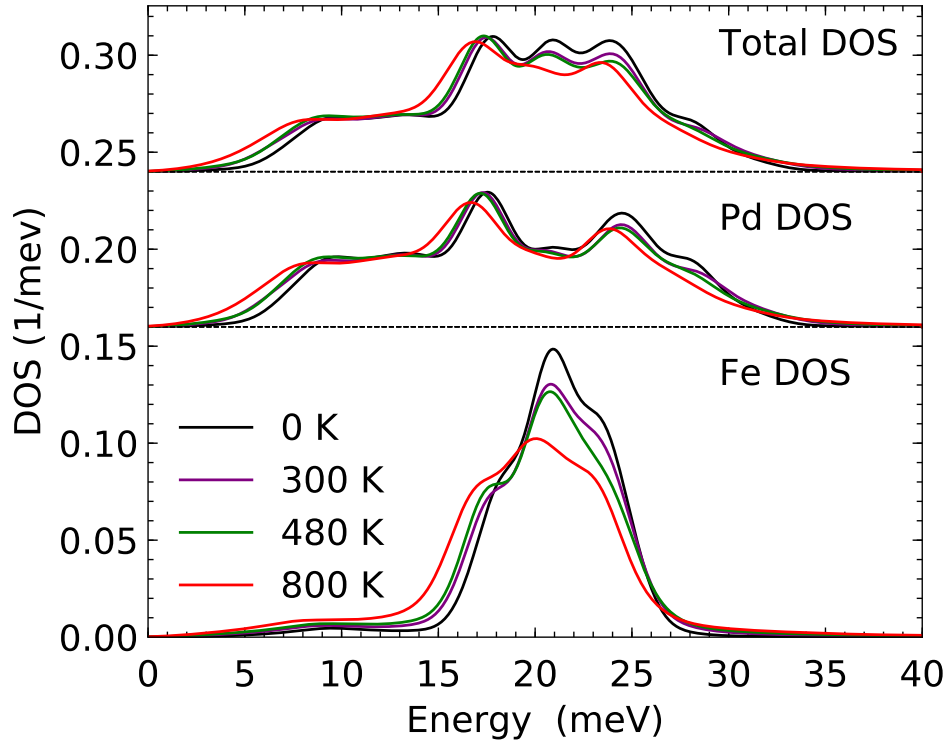


Figure 4.6: Total, Pd partial, and Fe partial phonon DOS curves of Pd₃Fe calculated with the s-TDEP method from 0 to 800 K.

Nonharmonic Behavior

The experimental nonharmonic behavior was analyzed by comparing the measured ⁵⁷Fe pDOS with Fe pDOS curves predicted by quasiharmonic (QH) approximations. The experimental QH phonon frequencies $\omega_i^{\text{QH}}(T)$ were calculated with the Grüneisen parameter model (referred to as the “QH γ_T Model”), a QH model using a thermal Grüneisen parameter $\bar{\gamma}_T$, averaged for all phonon modes:

$$\omega_i^{\text{QH}}(T) = \omega_i^{298\text{K}} \left(1 - \bar{\gamma}_{\text{th}} \frac{V_T - V_{298\text{K}}}{V_{298\text{K}}} \right), \quad (4.11)$$

with the 298 K ⁵⁷Fe phonons used for scaling the Grüneisen parameter in the QH γ_T model. The volumes at elevated temperatures V_T were calculated from the lattice parameters determined from our synchrotron XRD measurements, together with lattice parameters reported by Jääskeläinen [175]. The thermal Grüneisen parameter was calculated from bulk properties of Pd₃Fe:

$$\bar{\gamma}_{\text{th}}(T) = \frac{\alpha(T)K_T(T)\nu(T)}{C_V(T)}, \quad (4.12)$$

where $K_T(T)$ is the bulk modulus, $\alpha(T)$ is the linear thermal expansion, $\nu(T)$ is the crystalline volume per atom, and $C_V(T)$ is the heat capacity at constant volume. The

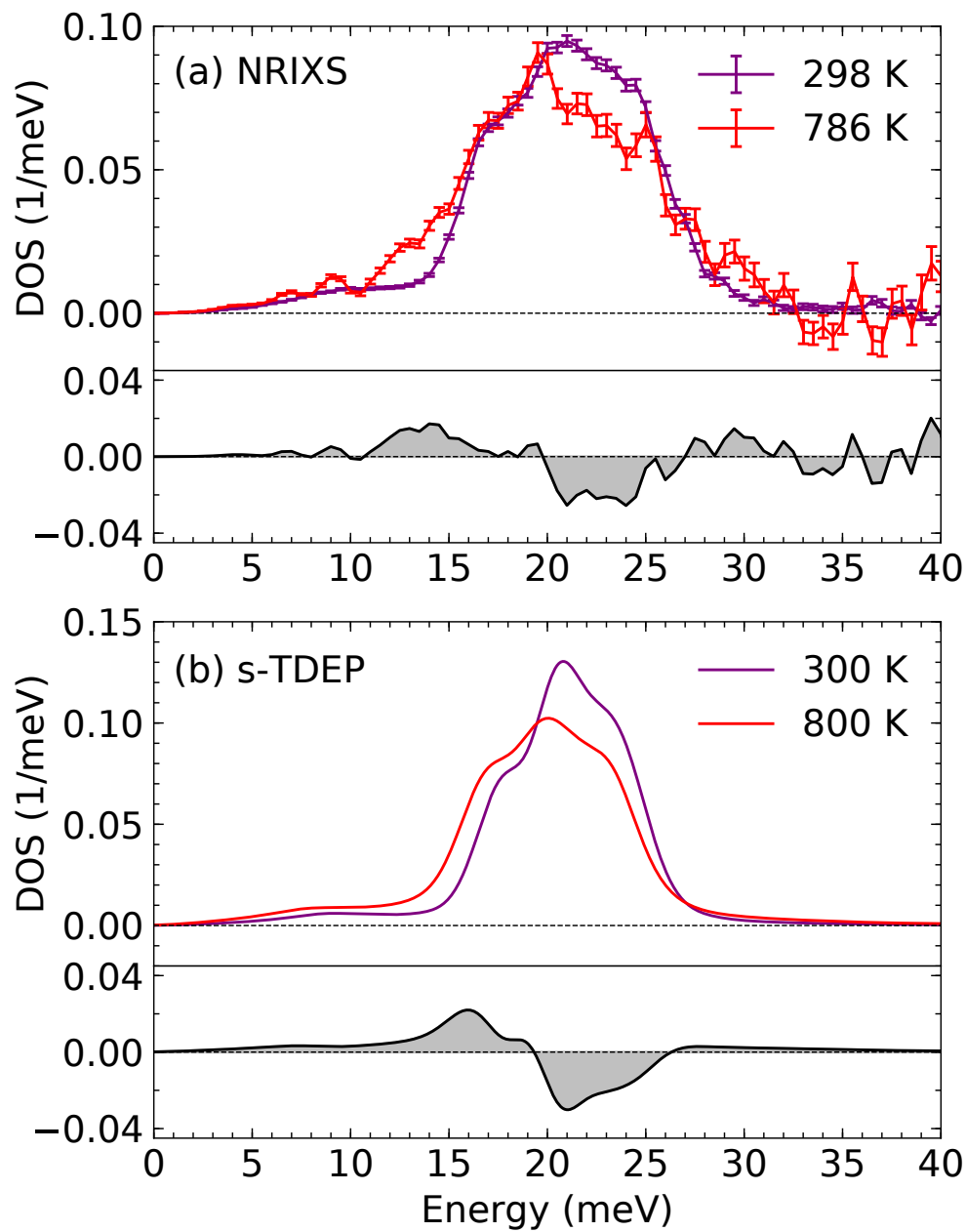


Figure 4.7: (a) NRIXS ^{57}Fe pDOS curves compared at 298 and 786 K. (b) s-TDEP Fe pDOS curves compared at 300 and 800 K. Phonon difference spectra are shown for both NRIXS and s-TDEP.

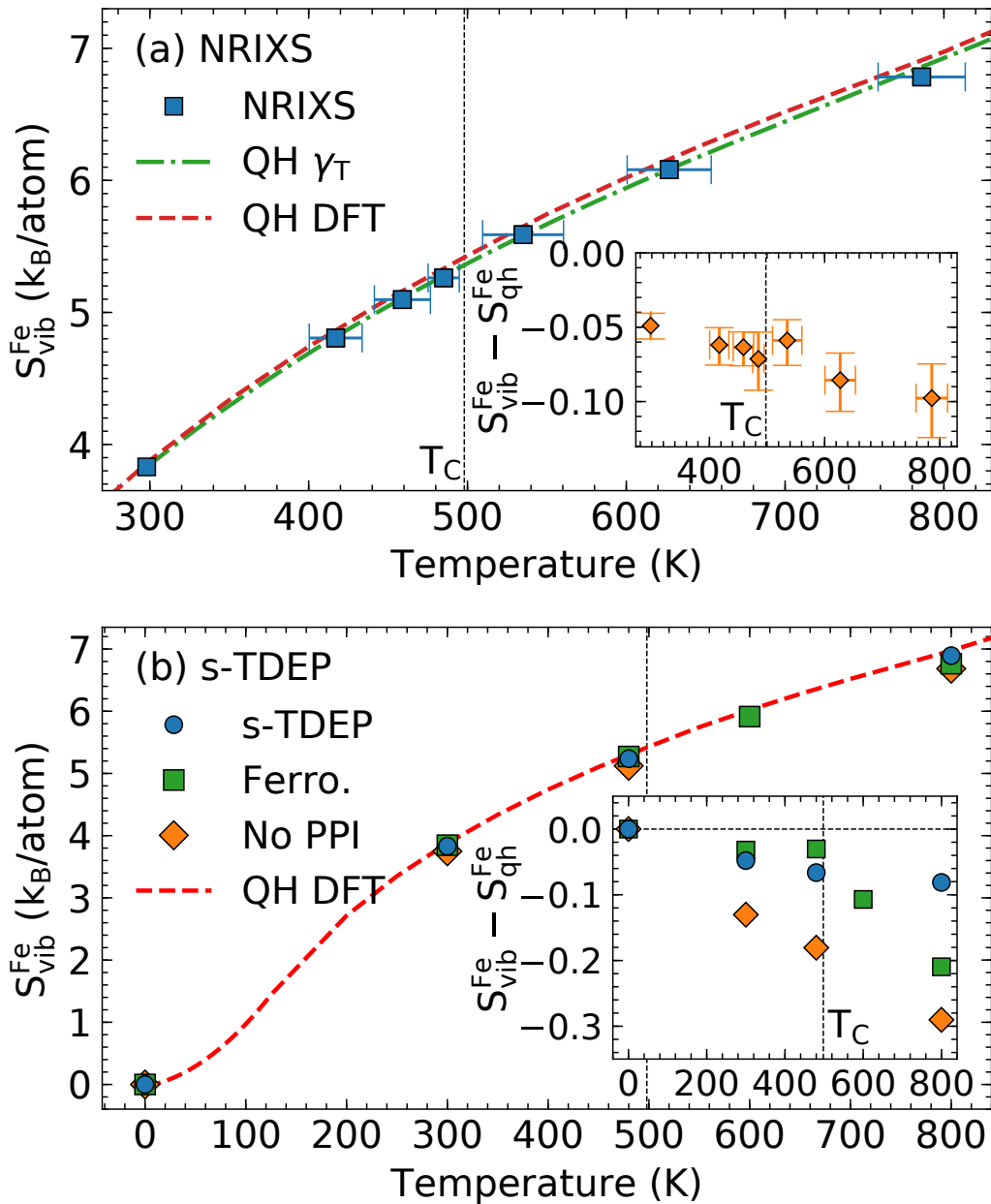


Figure 4.8: (a) The Fe partial vibrational entropy from the NRIXS measurements compared with the entropy from the Grüneisen parameter model (QH γ_T) and the QH DFT model. (b) The s-TDEP Fe partial vibrational entropy calculated for Pd_3Fe with changing magnetic order (blue), ferromagnetic order (green), and the absence of phonon-phonon interactions (orange). The red line is the entropy from the QH DFT model. The insets in (a) and (b) show the nonharmonic contributions to the vibrational entropy.

quantities $\alpha(T)$ and $\nu(T)$ were calculated from volumes obtained from synchrotron XRD and from Jääskeläinen. The heat capacity was calculated by integrating the total phonon DOS calculated by s-TDEP. The bulk modulus was previously determined by Winterrose through energy-dispersive x-ray diffraction [155].

The average Fe phonon energies from the QH γ_T and QH DFT models are plotted in Fig. 4.5. The Fe phonons calculated with the two QH models soften more strongly with temperature than the NRIXS ^{57}Fe pDOS, indicating that there is a nonharmonic stiffening in Pd_3Fe opposing the softening from thermal expansion.

Thermodynamic consequences of nonharmonic phonons were assessed by calculating the Fe partial vibrational entropy $S_{\text{vib}}^{\text{Fe}}$, which contributes to the total thermodynamic entropy. This $S_{\text{vib}}^{\text{Fe}}$ is obtained from the Fe pDOS as

$$S_{\text{vib}}^{\text{Fe}}(T) = 3k_B \int g_T^{\text{Fe}}(\varepsilon) \{ (n+1) \ln(n+1) - n \ln(n) \} d\varepsilon, \quad (4.13)$$

where k_B is the Boltzmann constant, $g_T^{\text{Fe}}(E)$ is the Fe pDOS at temperature T , and n is a Planck distribution evaluated at T for a given energy E . This expression provides accurate entropy values that include both quasiharmonic effects and nonharmonic effects [174].

The $S_{\text{vib}}^{\text{Fe}}(T)$ are plotted in Fig. 4.8(a). The quasiharmonic vibrational entropy $S_{\text{qh}}^{\text{Fe}}$, also shown in the figure, was calculated by substituting the Fe pDOS from the QH γ_T and QH DFT models into Eq. 4.13. The agreement is surprisingly good, considering that the QH model neglects so many nonharmonic effects, including those shown in Fig. 4.8(b).

Fig. 4.8(b) shows the Fe partial vibrational entropy calculated with the phonons calculated with s-TDEP, together with the Fe partial vibrational entropy without effects from PPI. This quantity, labeled “No PPI,” was calculated by substituting the Fe pDOS calculated with $\Gamma \rightarrow 0$ and $\Delta \rightarrow 0$ into Eq. 4.13. Also shown in the figure is the Fe partial vibrational entropy for ferromagnetic Pd_3Fe . These quantities were compared with the quasiharmonic entropy calculated from the QH DFT model.

The $S_{\text{vib}}^{\text{Fe}}$ of Pd_3Fe calculated with s-TDEP is lower than what is expected from the QH DFT model by $0.08 k_B/\text{atom}$ at 800 K. The inclusion of PPI increases $S_{\text{vib}}^{\text{Fe}}$ of Pd_3Fe by $0.2 k_B/\text{atom}$ at 800 K. The change in $S_{\text{vib}}^{\text{Fe}}$ from ferromagnetic Pd_3Fe to Pd_3Fe with magnetic disorder increases from roughly $-0.03 k_B/\text{atom}$ around the Curie temperature to roughly $0.1 k_B/\text{atom}$ at 800 K. This happens as the deviation

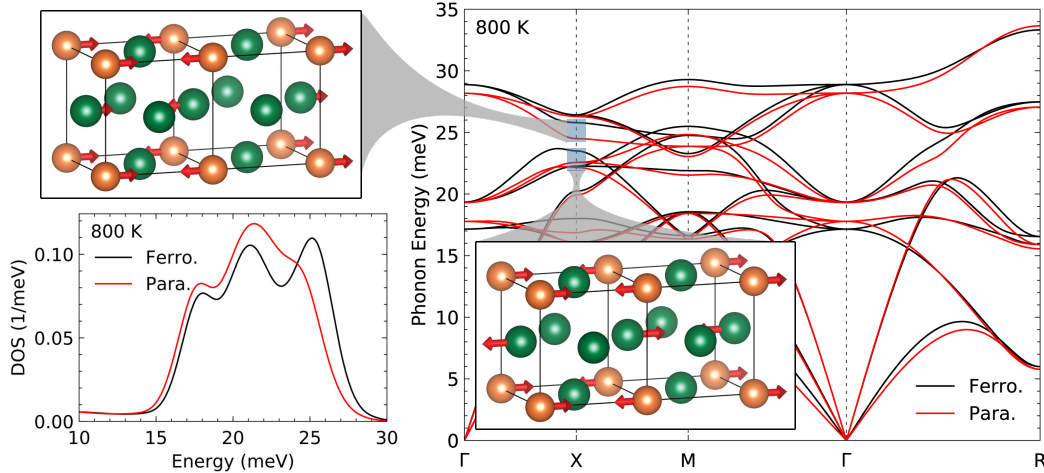


Figure 4.9: Calculated phonon dispersions for the ferromagnetic and paramagnetic states at 800 K. The dispersions displayed do not include effects from phonon-phonon interactions. Displacement patterns are shown for two high-energy optical phonon modes that soften with decreasing magnetization. The orange and green spheres represent Fe and Pd atoms, respectively. The Fe partial phonon DOS curves of Pd₃Fe calculated with the s-TDEP method for the ferromagnetic and paramagnetic states at 800 K are shown in the lower left.

from quasiharmonicity sharply increases for ferromagnetic Pd₃Fe past the Curie temperature.

4.4 Discussion

Magnon-Phonon Interaction

The increase in Fe partial vibrational entropy with decreasing magnetization at 800 K arises from the softening of Fe vibrational energies with the magnetic transition. A more in-depth analysis of this softening with decreasing magnetization is performed by comparing the 800 K phonon dispersions for both ferromagnetic and paramagnetic Pd₃Fe, as shown in Fig. 4.9.

A number of vibrational modes in Pd₃Fe undergo energy shifts with the randomization of the Fe magnetic moment orientations, particularly the two optical modes at the X symmetry point highlighted in Fig. 4.9. The softening of these modes contributes to the softening of the high-energy peak in the Fe partial phonon DOS with decreasing magnetization. By testing the sensitivity of the phonon dispersions to changes in each of the quadratic force constants obtained from the fit of Eq. 4.1 to the Born-Oppenheimer surface, we found that these two modes soften with the weakening of the Fe–Fe second-nearest-neighbor (2NN) longitudinal force con-

starts, which weaken by about 50% from the ferromagnetic state to the paramagnetic state at 800 K. This behavior is consistent with the atomic displacement patterns for the optical modes, which involve the motions of adjacent (100) planes of Fe atoms in opposite [100] directions. The softening of these modes coincides with a change in the interactions between the closest-neighbor magnetic atoms due to the loss of short-range magnetic order past the Curie temperature.

The average ^{57}Fe phonon energies from the NRIXS measurements change slowly below the Curie temperature. The s-TDEP calculations for Pd₃Fe and ferromagnetic Pd₃Fe show that the thermal evolution of the optical phonons depends on whether the magnetization changes with thermal fluctuations. A thermal optical phonon stiffening in ferromagnetic Pd₃Fe counteracts the phonon softening from thermal expansion. This behavior is observed in the NRIXS measurements from 298 to 485 K, where Pd₃Fe still maintains short-range magnetic order. In this case, the short-wavelength optical modes do not soften strongly with temperature, consistent with their behavior in a material with full magnetic order. Beyond the Curie temperature, where there is both long- and short-range magnetic disorder, the change in Fe–Fe interactions cancels this ferromagnetic stiffening of the short-wavelength optical phonons.

Phonon-Phonon Interaction

The s-TDEP calculations of the phonon DOS of Pd₃Fe show that anharmonicity has significant effects on the thermodynamics of the material, as indicated by the increase in the Fe partial vibrational entropy by up to $0.2 k_{\text{B}}/\text{atom}$ at 800 K. The anharmonic phonon shifts and broadenings can be studied in more detail with the phonon spectral functions $S(\mathbf{q}, E)$, the spectra of lattice excitations that can be interpreted as phonon modes broadened and shifted by phonon-phonon interactions. The spectral function is calculated with $\omega_{\mathbf{q}s}$, the phonon dispersion from quadratic force constants, and the real and imaginary components of the phonon self energy from Eq. 4.4 and 4.5:

$$S(\mathbf{q}, E) \propto \sum_s \frac{2\omega_{\mathbf{q}s}\Gamma_{\mathbf{q}s}(\Omega)}{[\Omega^2 - \omega_{\mathbf{q}s}^2 - 2\omega_{\mathbf{q}s}\Delta_{\mathbf{q}s}(\Omega)]^2 + 4\omega_{\mathbf{q}s}^2\Gamma_{\mathbf{q}s}^2(\Omega)}. \quad (4.14)$$

The spectral functions shown in Fig. 4.10 were calculated at multiple temperatures. The 0 K spectral function is in good agreement with the phonon dispersion measured with inelastic neutron scattering at 80 K by Stirling [176]. The significant phonon

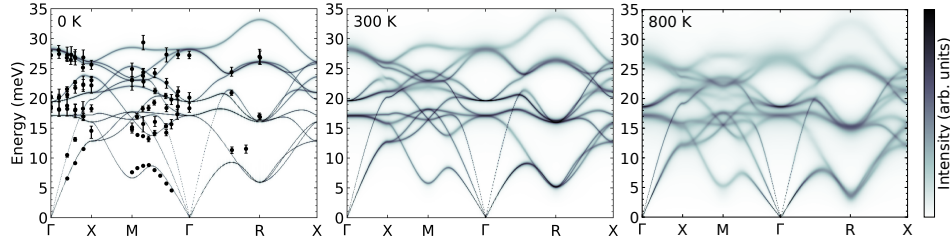


Figure 4.10: Pd₃Fe spectral functions (logarithmic intensity scale) calculated with s-TDEP along the high-symmetry directions at 0, 300, and 800 K. Measurements of the 80 K phonon dispersion by inelastic neutron scattering [176] are shown on top of the 0 K spectral function.

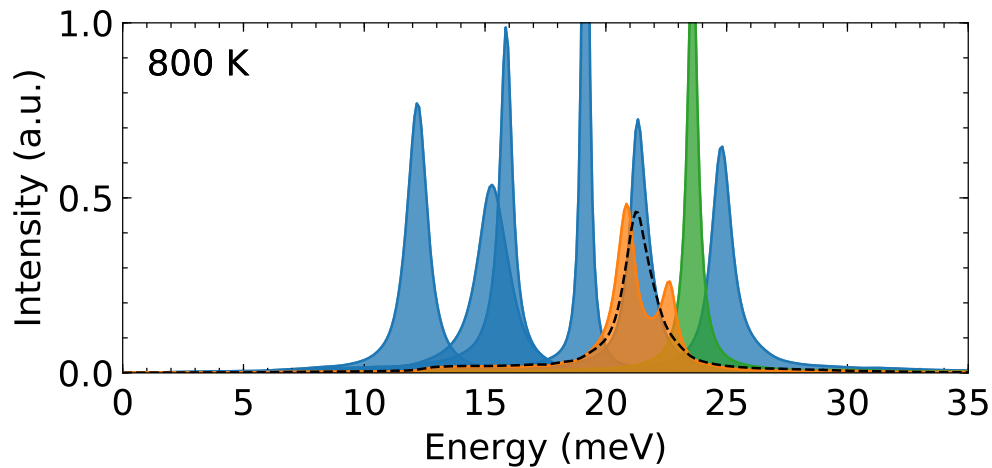


Figure 4.11: Pd₃Fe phonon lineshapes at the X high symmetry point at 800 K. The orange and green peaks are the optical modes that shift with changing magnetic order. The black dashed peak is the lineshape of the optical mode after the Pd–Pd 1NN cubic force constant is set to zero.

broadening and shifts in the spectral functions at higher temperatures come from many decay channels available to the phonons in the twelve branches.

We examined the lineshapes of phonon modes at specific \mathbf{q} points in the Brillouin zone, including the 800 K lineshapes of the phonon modes affected by the magnetic transition at the X symmetry point, shown in Fig. 4.11. What was unusual was a double-peak structure of one of these high-energy optical modes. Phonon modes with lineshapes that are characterized by a single peak broadened by a Lorentzian are mildly anharmonic, whereas phonon modes that have unusual lineshapes are more strongly anharmonic [177, 178].

To study the nature of the double peak of the high-energy phonon mode at X, we analyzed the cubic irreducible force constants responsible for three-phonon

interactions. The lineshapes at the X point were calculated when an irreducible force constant was set to zero. It was found that zeroing the cubic force constants for the Fe–Pd first nearest neighbors (1NN) along the $\langle 110 \rangle$ directions partially removes the double-peak structure, but zeroing the cubic force constants for the Pd–Pd 1NN along the $\langle 110 \rangle$ directions fully transforms the double-peak lineshape to a single Lorentzian peak, shown in Fig. 4.11.

These force constants are related to the movement of Fe and Pd atoms in the $[100]$ direction against the adjacent stationary (200) planes of Pd atoms. As shown in the displacement pattern of the vibrational mode in Fig. 4.9, (100) planes of Fe atoms and (100) of Pd atoms alternate in oscillating against the stationary (200) planes of Pd atoms. The cubic interactions from the oscillation of the (100) planes of Pd atoms against the (200) Pd planes more strongly contribute to the unusual phonon lineshape. We suggest that the palladium atoms dominate the anharmonic phonon-phonon interactions in $L1_2$ -ordered Pd_3Fe . This is consistent with how fcc Pd shows strong PPI at high temperatures [179].

4.5 Conclusions

Nuclear resonant inelastic x-ray scattering was used to measure the ^{57}Fe partial phonon DOS of $L1_2$ -ordered Pd_3Fe from room temperature through the Curie transition. The iron partial vibrational entropy at temperatures far from the Curie transition was observed to be approximately what was predicted by the quasiharmonic approximation owing to a cancellation of effects. A nonharmonic phonon stiffening opposed the expected softening from thermal expansion below the Curie temperature. Similar trends were observed from first-principles calculations that couple the stochastically-initialized temperature dependent effective potential (s-TDEP) method with magnetic special quasirandom structures (SQSs) of noncollinear magnetic moments.

The s-TDEP calculations showed that phonon-phonon interactions (PPI) contribute to the softening and broadening of the phonon spectra at elevated temperatures. A high-energy optical mode at the X symmetry point was calculated to have a double-peak lineshape. The first-nearest-neighbor Pd–Pd cubic interactions strongly contribute to this unusual lineshape, highlighting the strong contribution of the majority Pd atoms to the phonon anharmonicity in Pd_3Fe .

The calculations also showed that high-energy optical modes soften with decreasing magnetization, so a ferromagnetic optical phonon stiffening is lost. This softening

of optical modes originates with how the randomization of orientations of the Fe magnetic moments alters the short-range Fe–Fe interactions, softening the Fe–Fe second-nearest-neighbor force constants. The dependence of these optical vibrational modes on the magnetic transition can be understood as how magnon-phonon interactions alter lattice vibrations at elevated temperatures.

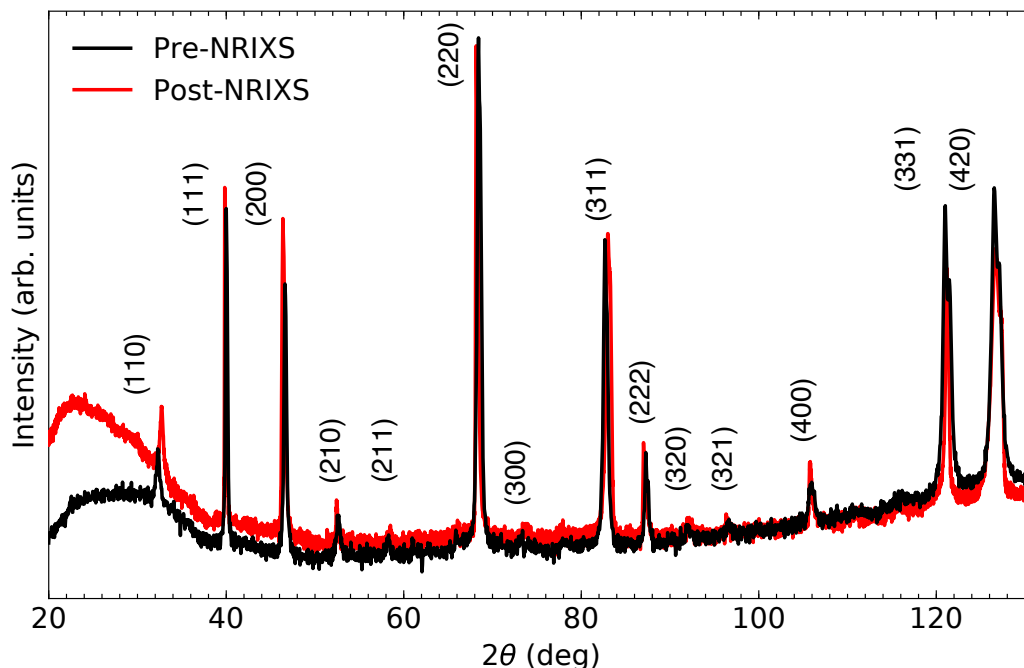


Figure 4.12: X-ray diffraction patterns of Pd₃⁵⁷Fe (“Ordered-II”) collected on a Cu K α laboratory diffractometer. Measurements were performed on the sample after the heat treatment (“Pre-NRIXS”) and after the NRIXS measurements (“Post-NRIXS”). The labeled peaks include both fundamental and superlattice peaks. The intensity is displayed in a logarithmic scale.

4.6 Supporting Information

Sample Preparation

Conventional X-Ray Diffraction

Characterization was performed on the Pd₃⁵⁷Fe sample with x-ray diffractometry using Cu K α radiation. The diffraction measurements were performed on the sample after the heat treatment described in the main text and after the nuclear resonant inelastic x-ray scattering (NRIXS) measurements at high temperature, with results shown in Fig. 4.12.

The diffraction patterns include fundamental peaks expected from fcc and fcc-based structures. The patterns also include superlattice peaks expected in the $L1_2$ structure, including (110), (210), (211), (320), and (321). The presence of these peaks are indicative of long-range $L1_2$ chemical order in the sample before and after the NRIXS measurements. X-ray diffractometry showed that the chemical order was at least as high after the NRIXS measurements as before.

Table 4.1: Hyperfine fields H and change in the hyperfine field ΔH in the $\text{Pd}_3^{57}\text{Fe}$ sample at different stages of this study, shown together with measurements performed by Longworth [154]. For the $\text{Pd}_3^{57}\text{Fe}$ sample, the hyperfine field for “Ordered-II” is treated as a reference for ΔH . For the measurements performed by Longworth, the hyperfine field for the ordered sample is treated as a reference for ΔH .

Sample	Hyperfine Field H (kOe)	ΔH (kOe)
Ordered-I	286.402 ± 0.01	-5.849
Ordered-II	292.251 ± 0.01	0
Post-NRIXS	290.821 ± 0.01	-1.430
Ordered (Longworth)	285.5 ± 1	0
Disordered (Longworth)	278 ± 1	-7.5

The lattice parameter of Pd_3Fe was measured to be $3.852 \pm 0.001 \text{ \AA}$. All diffraction measurements provided similar values of lattice parameters within the margin of error.

Mössbauer Spectrometry

Mössbauer spectra were collected from conversion electrons in backscatter geometry using a constant acceleration spectrometer with a ^{57}Co in Rh γ -ray source. Velocity and isomer shift calibrations were performed by reference to room temperature α -iron. The conversion electron Mössbauer spectra of the $\text{Pd}_3^{57}\text{Fe}$ foil sample over the course of this experiment are shown in Fig. 4.13.

The hyperfine field was measured from Mössbauer spectrometry for the previously annealed $\text{Pd}_3^{57}\text{Fe}$ sample before the second heat treatment described in the main text (“Ordered-I”), after this heat treatment (“Ordered-II”), and after the high-temperature NRIXS measurements. These values are reported in Table 4.1, together with the hyperfine field of the ordered Pd_3Fe and disordered $\text{Pd}_{0.73}\text{Fe}_{0.27}$ samples measured by Longworth [154].

From the mean hyperfine fields, it appears that there was little change in the state of chemical order near the surface of the sample probed by the conversion electron Mössbauer spectrometer.

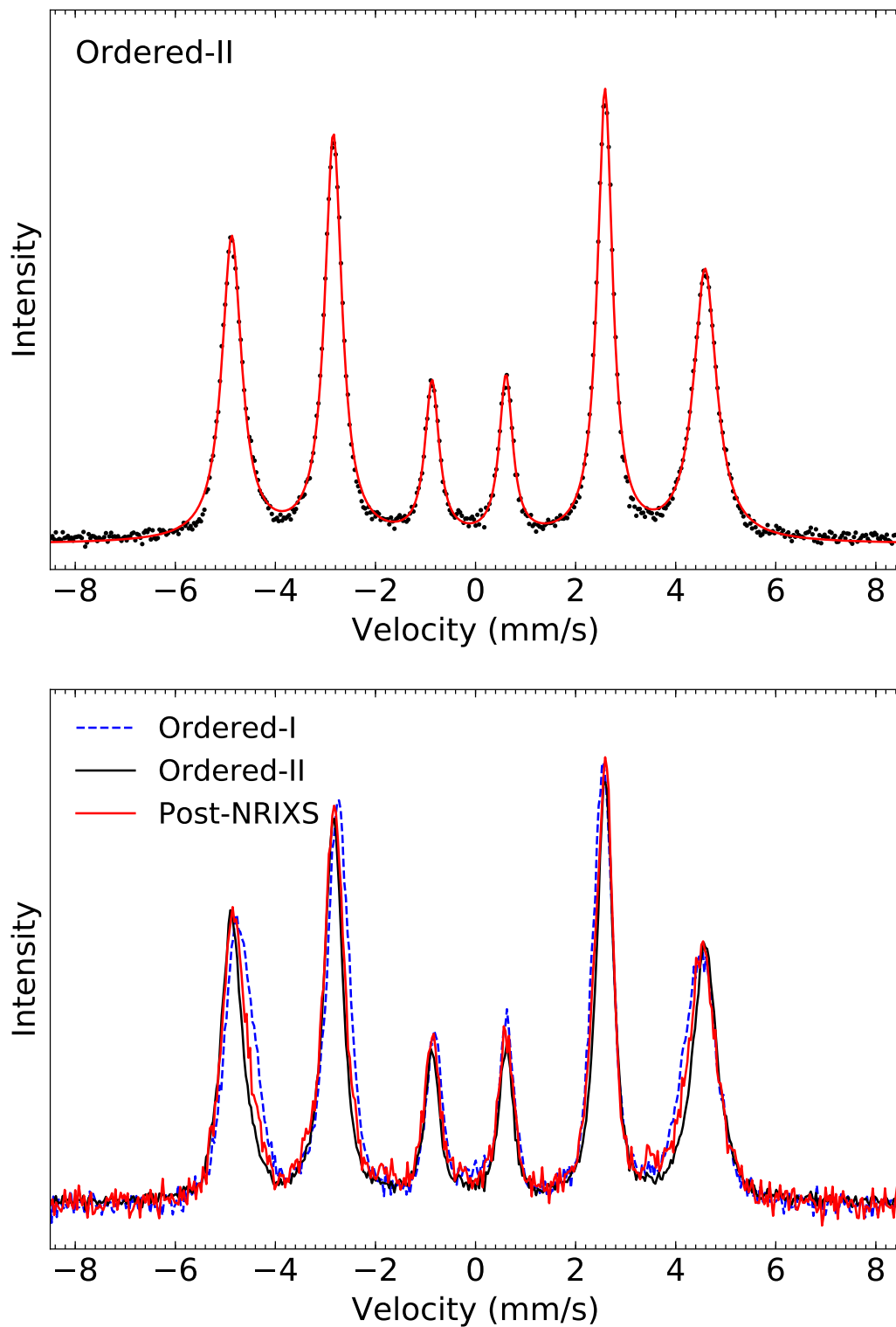


Figure 4.13: (Top) Room temperature Mössbauer spectrum of the annealed $\text{Pd}_3^{57}\text{Fe}$ foil sample before the NRIXS experiment (Ordered-II). (Bottom) $\text{Pd}_3^{57}\text{Fe}$ Mössbauer spectra for the “Ordered-I” state, “Ordered-II” state, and after the NRIXS experiment.

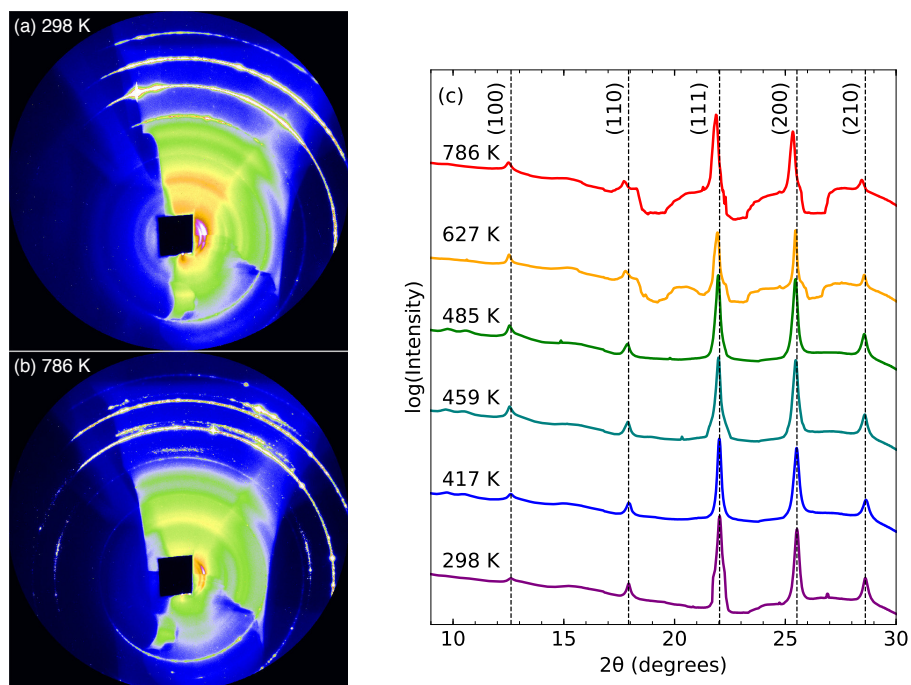


Figure 4.14: Two-dimensional synchrotron diffraction patterns of Pd_3Fe recorded on a CCD detector plate at (a) 298 K and (b) 786 K. (c) One-dimensional synchrotron x-ray diffraction patterns of $\text{Pd}_3^{57}\text{Fe}$ from 298 to 786 K. The black dashed lines are the locations of the 298 K diffraction peaks. The dips in intensity for 627 and 786 K are where extraneous diffraction peaks from the aluminum foil were masked.

Synchrotron Measurements

Synchrotron X-ray Diffraction

In situ synchrotron x-ray diffraction (XRD) measurements were performed at beamline 16ID-D of the Advanced Photon Source at Argonne National Laboratory using a monochromatic beam at 14.413 keV and a resistive heating furnace with a kapton window for x-ray transmission. Diffraction was measured using a Mar CCD detector plate. The two-dimensional diffraction rings on the image plate (Fig. 4.14(a) and (b)) were integrated with the FIT2D [180] program to produce diffraction patterns of intensity vs. 2θ (Fig. 4.14(c)).

For measurements above the Curie temperature, a 16 micron-thick piece of aluminum foil was placed over the kapton window to reflect the radiative heat from the furnace away from the avalanche photodiodes used in the NRIXS measurements. The aluminum foil caused the additional diffraction rings at 627 and 786 K. These extraneous rings were masked in the FIT2D program, resulting in the dips in intensity in the integrated diffraction patterns for 627 and 786 K.

The lattice parameters of the $L1_2$ -ordered Pd_3Fe were determined from synchrotron XRD to be

3.8541 Å at 298 K; 3.8546 Å at 417 K; 3.8636 Å at 459 K;
3.8661 Å at 485 K; 3.8719 Å at 627 K; 3.8854 Å at 786 K.

These results are consistent with a prior XRD measurement of the lattice parameter of Pd_3Fe with respect to temperature [175].

Nuclear Resonant Inelastic X-ray Scattering

NRIXS measurements were performed on $\text{Pd}_3^{57}\text{Fe}$ at seven temperatures from 298 to 786 K at beamline 16ID-D of the Advanced Photon Source at Argonne National Laboratory. For each temperature, the NRIXS spectrum was measured by scanning the energy transfer from -80 to $+80$ meV around the resonant energy of ^{57}Fe in several scans that were combined for final analysis. The spectra are shown in Fig. 4.15. The energy resolution of all NRIXS measurements was measured to be 2.2 meV (FWHM) at the elastic line. The instrument resolution function is also shown in Fig. 4.15.

The PHOENIX software package was used to extract the ^{57}Fe partial phonon densities of states (pDOS) from the NRIXS spectra [80]. The data reduction procedure in the PHOENIX software package involves the removal of the resonant elastic peak and the multi-phonon processes from the NRIXS spectra. The one-, two-, and three-phonon contributions to the NRIXS spectra at 298 and 786 K are shown in Fig. 4.16.

Other physical quantities were calculated from the data reduction procedure in PHOENIX. One such physical quantity is the Lamb-Mössbauer factor, plotted in Fig. 4.17. The Lamb-Mössbauer factor was also calculated from fits to the nuclear forward scattering (NFS) spectra with the CONUSS software package [173]. Due to the low counts in the nuclear forward scattering spectra, the Lamb-Mössbauer factors obtained from the NFS spectra are expected to have a greater error than those obtained from the data reduction of the NRIXS spectra.

Figure 4.18 shows previous room temperature NRIXS measurements of the $L1_2$ -ordered $\text{Pd}_3^{57}\text{Fe}$ compound in its “Ordered-I” state and the disordered fcc alloy $\text{Pd}_{0.75}^{57}\text{Fe}_{0.25}$. The ^{57}Fe pDOS for the disordered sample is considerably different from the “Ordered-I” pDOS and the pDOS from this study (“Ordered-II”).

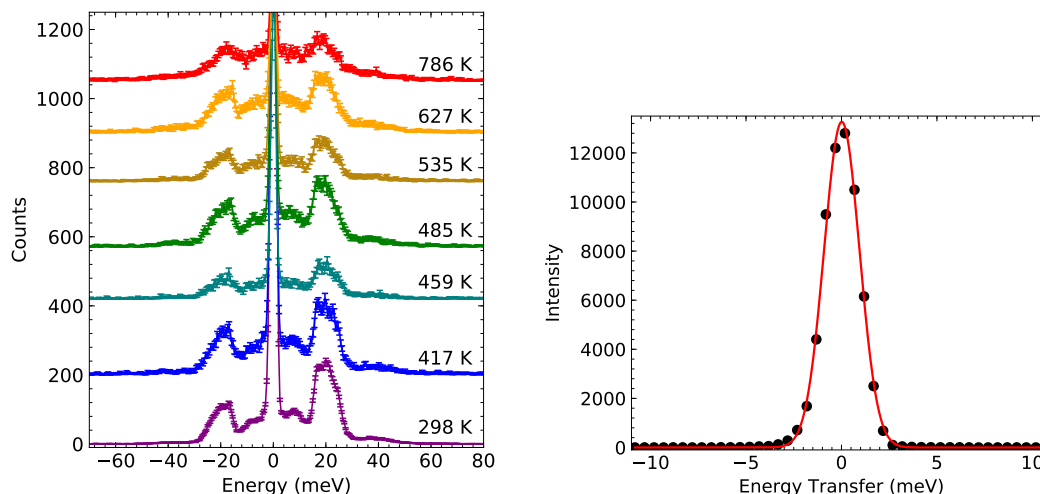


Figure 4.15: (Left) Raw NRIXS scattering spectra showing ^{57}Fe vibrational excitations in $\text{Pd}_3^{57}\text{Fe}$ as a function of scattering energy. Spectra are collected over a range of temperatures. (Right) The elastic line of the raw scattering spectrum of ^{57}Fe at room temperature, used as the instrument resolution function for the NRIXS measurements.

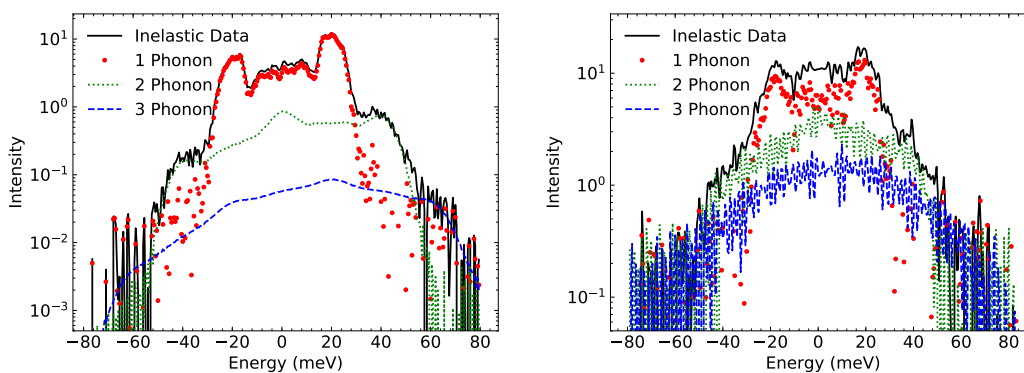


Figure 4.16: The multi-phonon components of the NRIXS spectra of $\text{Pd}_3^{57}\text{Fe}$ at (left) 298 K and (right) 786 K.

Table 4.2: The Fe partial vibrational heat capacity calculated from the integration of the ^{57}Fe phonon DOS.

Temperature (K)	Fe Partial Heat Capacity (k_B/atom)
298	2.8382 ± 0.0106
417	2.8355 ± 0.0376
459	2.9227 ± 0.0535
485	2.8686 ± 0.0385
535	2.9125 ± 0.0518
627	2.9702 ± 0.0408
786	3.0107 ± 0.0434

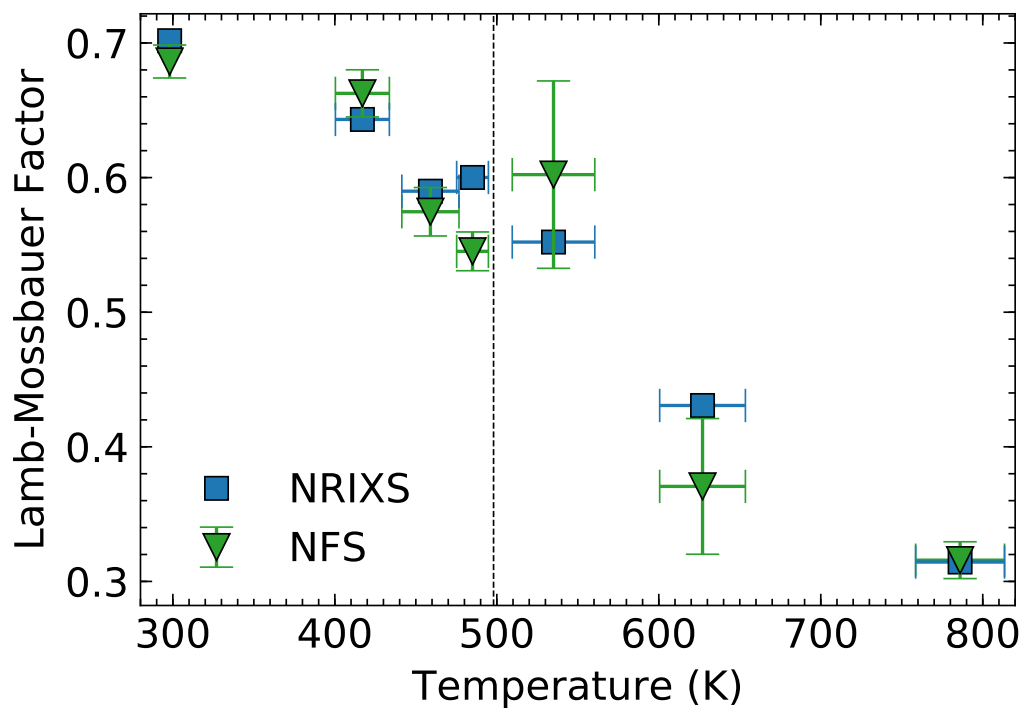


Figure 4.17: Lamb-Mössbauer factors obtained from NRIXS (blue squares) and NFS (green triangles).

Table 4.3: The vibrational kinetic energy calculated from the integration of the ^{57}Fe phonon DOS.

Temperature (K)	Kinetic Energy (meV/atom)
298	13.5647 ± 0.0603
417	19.8122 ± 0.4101
459	20.6811 ± 0.5960
485	22.0571 ± 0.4264
535	23.7510 ± 0.5040
627	28.4609 ± 0.4977
786	33.1471 ± 0.5778

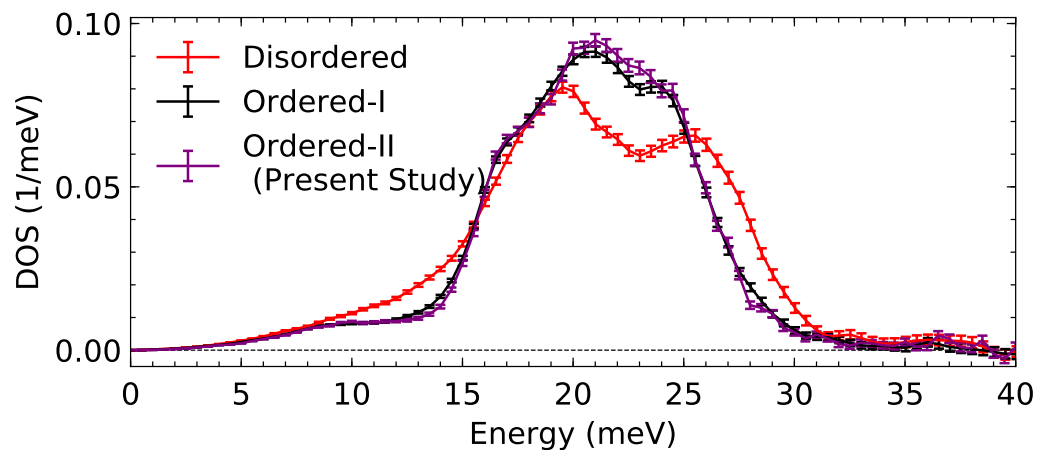


Figure 4.18: The room temperature ^{57}Fe pDOS of the $\text{Pd}_3^{57}\text{Fe}$ sample measured in this study (purple) compared with prior measurements of the room temperature ^{57}Fe pDOS of ordered $\text{Pd}_3^{57}\text{Fe}$ (black) and the disordered fcc alloy $\text{Pd}_{0.75}^{57}\text{Fe}_{0.25}$ (red).

Table 4.4: The mean force constant calculated from the integration of the ^{57}Fe phonon DOS.

Temperature (K)	Mean Force Constant (N/m)
298	2.435 ± 0.024
417	2.440 ± 0.030
459	2.421 ± 0.027
485	2.448 ± 0.043
535	2.360 ± 0.034
627	2.343 ± 0.040
786	2.340 ± 0.047

CONCLUDING REMARKS AND FUTURE DIRECTIONS

This thesis research explored the temperature dependence of adiabatic electron-phonon interactions in the metallic systems FeTi and vanadium, and the temperature dependence of magnon-phonon interactions through the Curie temperature of ferromagnetic Pd₃Fe. Our ability to study these interactions and their effects on the thermal evolution of the vibrational entropy was made possible by synchronously pushing the limits on both experimental measurements and theoretical calculations.

5.1 Electron-Phonon Interactions

First-principles computational methods ranging from the temperature dependent effective potential (TDEP) method to electronic band unfolding have provided a new perspective of the relationship between lattice dynamics and the changing electronic structure. The strength of the electronic screening of atomic vibrations is altered by the increasingly large amplitudes of atomic displacements with temperature. The electron-phonon interaction nesting features of the Fermi surface are smeared by both these displacements and the thermal excitations of electrons occupying states within the thermal layer surrounding the Fermi level. Thermal shifts in electronic bands can sometimes change the topology of the Fermi surface. If the effects of thermally-driven electronic topological transitions (ETT) overtake the effects of the thermal smearing of nesting features, these ETTs bring forth dramatic changes to the temperature dependence of adiabatic electron-phonon interactions.

We are interested in continuing this study of the temperature dependence of electron-phonon interactions and possibly thermally-driven ETTs. Studies of phonon anomalies and electron-phonon interactions in transition metal carbides (TMCs) and nitrides (TMNs) [181–183] may point to future opportunities for research. Li *et al.* have recently reported that group V TMCs display lattice thermal conductivities that are nearly independent of temperature owing to Fermi surface nesting [184]. This research direction may direct us to new insights about electronic and heat transport.

We conducted our analyses of the electron-phonon interactions in FeTi and vanadium by quantifying changes in the Fermi surface nesting features and the spanning vector densities. This in-depth analysis of the electronic structure of metals has proven to be

rich in information in comparison to analyzing only the electronic density of states. What we had not accounted for was the electron-phonon matrix element $g_{mn}^y(\mathbf{k}, \mathbf{q})$, a crucial quantity for calculating the strength of electron-phonon interactions:

$$g_{mn}^y(\mathbf{k}, \mathbf{q}) = \sqrt{\frac{\hbar}{2\omega_{\mathbf{q}v}}} \sum_{\kappa\alpha} \frac{e_{\mathbf{q}v}^{\kappa\alpha}}{\sqrt{m_\kappa}} \langle m\mathbf{k} + \mathbf{q} | \partial_{\mathbf{q}\kappa\alpha} V | n\mathbf{k} \rangle. \quad (5.1)$$

We are currently capable of calculating $g_{mn}^y(\mathbf{k}, \mathbf{q})$ for arbitrary q -points using arbitrarily dense k -grids through a variety of software packages including EPW and ABINIT [185, 186]. As we have stated in Chapter 3, however, the recent *ab initio* methods for calculating the electron-phonon matrix element are based on density functional perturbation theory, which does not adequately describe thermal effects observed at finite temperatures. Temperature dependent matrix elements $g_{mn}^y(\mathbf{k}, \mathbf{q})$ were calculated using phonon energies $\omega_{\mathbf{q}v}(T)$ and eigenvectors $\mathbf{e}_{\mathbf{q}v}(T)$ calculated with the TDEP method in a recent study by Zhou *et al.* [100]. These matrix elements were used to predict the electron mobility in SrTiO₃ between 150-300 K, which were in good agreement with experimental values. The predictive power of these calculations of temperature dependent electron-phonon matrix elements can be further optimized with *ab initio* calculations of the matrix elements $\langle m\mathbf{k} + \mathbf{q} | \partial_{\mathbf{q}\kappa\alpha} V | n\mathbf{k} \rangle$, which require calculations of the gradient of temperature-dependent potentials with respect to atomic displacements and the temperature-dependent electronic structure. This calculation still remains an open challenge to computational materials physics.

The materials physics research community is moving in the right direction towards the prediction of the matrix elements $\langle m\mathbf{k} + \mathbf{q} | \partial_{\mathbf{q}\kappa\alpha} V | n\mathbf{k} \rangle$ at finite temperatures. We have seen several recent developments towards the calculation of temperature-dependent electronic band structure ranging from methods based off of perturbation theory [118–123, 187] to nonperturbative adiabatic calculations [23, 188–193] not very different in nature from the electronic band unfolding procedure employed in Chapters 2 and 3. The research community is building towards a formalism for the *ab initio* determination of electron-phonon interaction strengths at elevated temperatures, and we hope that our work contributes to this research effort.

We had hypothesized at the end of Chapter 2 that materials with occupied or unoccupied bands that are a few $k_B T$ away from the Fermi level at low temperatures may display thermally-driven ETTs that cause rapid and abrupt changes in physical properties with temperatures. Based on this alone, we may be tempted to reduce this search for candidate materials with adiabatic EPIs impacted by thermally-

driven ETTs down to a search through 0 K electronic band structures provided in materials databases. Merely looking at 0 K electronic band structures, however, led us to predict that a thermally-driven ETT involving the disappearance of electron pockets in vanadium would contribute to the thermal phonon stiffening. We did not predict that a thermally-driven ETT that was different from what we had expected would be cancelled by the thermal smearing of the Fermi surface in vanadium. A strong understanding of the temperature evolution of both the lattice dynamics and electronic bands in materials can aid our search for these candidate materials. The ability to calculate temperature-dependent electron-phonon interaction parameters can also allow us to more quantitatively analyze thermally-driven ETTs and their novel impacts on high temperature thermodynamics.

5.2 Magnon-Phonon Interactions

We have performed an in-depth study of the lattice dynamics of the ferromagnetic Pd_3Fe with both experimental measurements and advanced theoretical calculations. By combining our experimental results with a combination of the TDEP method and magnetic special quasirandom structures (SQSs), we proposed an atomistic mechanism for the temperature-dependent magnon-phonon interaction in Pd_3Fe by linking it to the reduction of the ferromagnetic optical phonon stiffening from Fe–Fe second-nearest-neighbor interactions through the Curie transition. The computational methods performed in this study can serve as building blocks towards the accurate modeling the finite temperature lattice dynamics of magnetic materials [33, 34, 138–146]. We would ideally like to see these computational tools develop to the point where we can predict the thermodynamics of materials displaying magnetism ranging from localized magnetism to itinerant magnetism across a wide range of temperatures.

We observed that the ferromagnetic system Pd_3Fe displayed several competing contributions to the vibrational entropy. The cancellation of magnon-phonon interactions and anharmonicity have resulted in thermal trends close to quasiharmonicity. We have now observed cases where temperature-dependent magnon-phonon interactions can either have profound effects on the vibrational thermodynamics [7] or have muted effects due to competing factors [31]. If we wish to continue investigating magnon-phonon interactions at elevated temperatures, we would benefit from studying materials with significant thermal phonon anomalies arising from magnetic transitions with very little competing factors like anharmonicity.

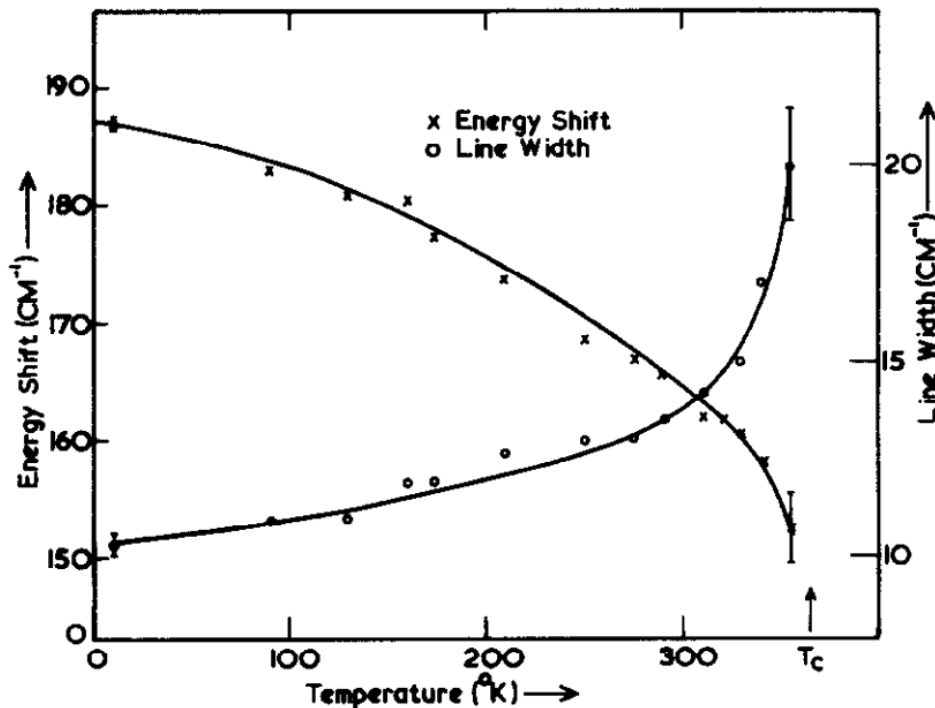


Figure 5.1: The frequency shifts and linewidth of the E_g 187 cm^{-1} Raman line versus temperature in FeF_3 , measured by Shepherd [197].

We may look to studying the temperature dependence of magnon-phonon interactions in bcc chromium with inelastic neutron scattering and first-principles calculations. Chromium displays dramatic phonon softening with temperature [194, 195] that may be related to magnetic disorder [196]. There is, however, a possibility that other factors contribute to the thermal phonon softening in chromium, including electron-phonon interactions. Significant challenges would meanwhile lie in modeling its spin-density-wave state and paramagnetic state from low to intermediate temperatures.

We may also be interested in conducting an in-depth study of the lattice dynamics of FeF_3 with first-principles calculations and scattering methods including nuclear resonant inelastic x-ray scattering (NRIXS). Shepherd had observed an anomalous temperature dependence of the E_g 187 cm^{-1} Raman peak in the vicinity of the magnetic transition, as shown in Fig. 5.1 from Ref. [197]. A study of this trigonal material may provide an opportunity for the further development of our computational methods for performing phonon calculations with diminishing magnetic order.

Finally, we can revisit the interplay between lattice dynamics and the Curie transition

in bcc α -iron through both NRIXS and first-principles calculations at elevated temperatures and pressures. Not only would this study push boundaries in the experimental measurements of phonon frequencies, we would be able to study the dependence of nonharmonic lattice dynamics on simultaneous pressure and temperature that we would not see at high pressure or high temperature alone [109, 198]. Such a study would provide us insights into the physical properties of iron-based materials at extreme conditions. We see that there are still many open questions regarding the vibrational thermodynamics of magnetic materials, and that there remains much work to be done.

Appendix A

HARMONIC MODEL

A.1 Einstein and Debye Models

In the Einstein model, the harmonic solid is treated as N oscillators with the same vibrational frequency $\omega_0 = \varepsilon_0/\hbar$, such that the phonon density of states (DOS) is a delta function $\delta(\varepsilon - \varepsilon_0)$. While this is a great simplification of lattice dynamics, the results from the Einstein model suggest the energies of lattice vibrations are quantized, and that the contribution of high-energy vibrational modes to the specific heat exponentially drops to zero as the temperature approaches 0 K.

The Debye model assumes that phonon frequencies ω obey a linear relationship with respect to the reciprocal lattice vector \mathbf{q} . This model treats the harmonic solid as a repeating lattice of N atoms that vibrates as if it were an elastic continuum. In this model, the vibrational frequencies cannot exceed a certain frequency ω_D chosen to make the total number of vibrational modes equal to the total number of classical degrees of freedom. In a three-dimensional solid, the phonon DOS behaves as ε^2 up to the cutoff energy. This assumption of linear phonon branches accurately describes the long wavelength limit (very low $|\mathbf{q}|$), and it recovers the low temperature T^3 behavior observed in measured heat capacities.

A.2 Born von Kármán Model

Phonon frequencies ω and the phonon DOS can be more accurately calculated through a normal mode analysis as presented by Born and von Kármán [5]. In a crystal with an atomic basis described by the vectors $\{\mathbf{r}_\kappa\}$, the position $\mathbf{R}_{l\kappa}$ of a vibrating atom κ in the unit cell l at time t is

$$\mathbf{R}_{l\kappa}(t) = \mathbf{r}_l + \mathbf{r}_\kappa + \mathbf{u}_{l\kappa}(t), \quad (\text{A.1})$$

where $\mathbf{u}_{l\kappa}$ is the displacement of the atom about its equilibrium position $\mathbf{r}_l + \mathbf{r}_\kappa$. The potential energy U of the crystal at any t is a function of the instantaneous positions of the atoms. We can expand the potential energy in a Taylor series of the atomic displacements about $\mathbf{u}_{l\kappa}(t) = 0$, the equilibrium positions:

$$U = U_0 + \sum_{\alpha l \kappa} \Phi_{\alpha l \kappa} u_{\alpha l \kappa} + \frac{1}{2} \sum_{\alpha l \kappa} \sum_{\alpha' l' \kappa'} \Phi_{\alpha \alpha' l l' \kappa \kappa'} u_{\alpha l \kappa} u_{\alpha' l' \kappa'} + \dots, \quad (\text{A.2})$$

where U_0 is a static potential term. We use the Cartesian components $u_{\alpha l\kappa}$ for the displacement vector, where $\alpha = \{x, y, z\}$. The coefficients of the Taylor series are derivatives of the potential with respect to the displacements evaluated in the equilibrium configuration:

$$\Phi_{\alpha l\kappa} = \left. \frac{\partial U}{\partial u_{\alpha l\kappa}} \right|_0 \quad (\text{A.3})$$

$$\Phi_{\alpha\alpha'l'l'\kappa\kappa'} = \left. \frac{\partial^2 U}{\partial u_{\alpha l\kappa} \partial u_{\alpha'l'\kappa'}} \right|_0. \quad (\text{A.4})$$

Because there is no force on any atom in equilibrium, $\Phi_{\alpha l\kappa} = 0$ for all atoms. In the harmonic model, we keep the remaining terms of the series written explicitly in Eq. A.2 while neglecting terms of higher order. We can rewrite what remains of this Taylor expansion in matrix form:

$$U = U_0 + \frac{1}{2} \sum_{l\kappa l'\kappa'} \ddot{\mathbf{u}}_{l\kappa}^T \Phi_{l\kappa l'\kappa'} \mathbf{u}_{l'\kappa'}, \quad (\text{A.5})$$

where $\Phi_{l\kappa l'\kappa'}$ is the force constant matrix defined for each atom pair $(l\kappa; l'\kappa')$.

The equations of motion for all atomic nuclei are

$$m_\kappa \mathbf{u}_{l\kappa}(t) = - \sum_{l'\kappa'} \Phi_{l\kappa l'\kappa'} \mathbf{u}_{l'\kappa'}(t) \quad \forall l, \kappa. \quad (\text{A.6})$$

With periodic boundary conditions, the solution of Eq. A.6 can be in the form of plane waves of wavevector \mathbf{q} , angular frequency $\omega_{\mathbf{q}\nu}$, and polarization $\mathbf{e}_\nu^{\mathbf{q}}$, where ν is a ‘‘branch index’’:

$$\mathbf{u}_{l\kappa\mathbf{q}\nu}(t) \propto \mathbf{e}_\nu^{\mathbf{q}} e^{i(\mathbf{q}\cdot\mathbf{r}_l - \omega_{\mathbf{q}\nu}t)}. \quad (\text{A.7})$$

The substitution of the plane wave displacements into the equations of motion is equivalent to taking Fourier transforms, reducing the problem into diagonalizing the ‘‘dynamical matrix’’ $D(\mathbf{q})$:

$$\sum_{\kappa'} D_{\kappa\kappa'}(\mathbf{q}) \mathbf{e}_\nu^{\kappa}(\mathbf{q}) = \omega_{\mathbf{q}\nu}^2 \mathbf{e}_\nu^{\kappa}(\mathbf{q}), \quad (\text{A.8})$$

where each sub-matrix $D_{\kappa\kappa'}(\mathbf{q})$ is the Fourier transform of the force constant matrix $\Phi_{l\kappa l'\kappa'}$. The dynamical matrix $D(\mathbf{q})$ is Hermitian for any \mathbf{q} , meaning the eigenvalues $\omega_{\mathbf{q}\nu}^2$ are real. The phonon DOS in this normal mode analysis is the histogram of frequencies calculated from the diagonalization of $D(\mathbf{q})$ over a large number of points covering the first Brillouin zone.

BIBLIOGRAPHY

- [1] A. White. *MRS Bull.*, 37:716, 2012.
- [2] S. Curtarolo, G. L. W. Hart, M. B. Nardelli, N. Mingo, S. Sanvito, and O. Levy. *Nat. Mater.*, 12:191, 2013.
- [3] P. M. Morse. *Thermal physics*. W. A. Benjamin, New York, 1962.
- [4] B. Fultz. *Prog. Mater. Sci.*, 55:247, 2010.
- [5] M. Born and T. von Kármán. *Z. Physik*, 13:297, 1912.
- [6] A. T. Dinsdale. *Calphad*, 15:317, 1991.
- [7] L. Mauger, M. S. Lucas, J. A. Muñoz, S. J. Tracy, M. Kresch, Y. Xiao, P. Chow, and B. Fultz. *Phys. Rev. B*, 90:064303, 2014.
- [8] E. Grüneisen. *Ann. Physik*, 344:257, 1912.
- [9] Y. Takahashi, J. I. Nakamura, and J. F. Smith. *J. Chem. Thermodynamics*, 14:977, 1982.
- [10] O. Delaire, M. Kresch, J. A. Muñoz, M. S. Lucas, J. Y. Y. Lin, and B. Fultz. *Phys. Rev. B*, 77:214112, 2008.
- [11] O. Hellman, I. A. Abrikosov, and S. I. Simak. *Phys. Rev. B*, 84:180301, 2011.
- [12] M. A. Uijtewaal, T. Hickel, J. Neugebauer, M. E. Gruner, and P. Entel. *Phys. Rev. Lett.*, 102:035702, 2009.
- [13] T. Lan, C. W. Li, O. Hellman, D. S. Kim, J. A. Muñoz, H. Smith, D. L. Abernathy, and B. Fultz. *Phys. Rev. B*, 92:054304, 2015.
- [14] N. Shulumba, O. Hellman, Z. Raza, B. Alling, J. Barrirero, F. Mücklich, I. A. Abrikosov, and M. Odén. *Phys. Rev. Lett.*, 117:205502, 2016.
- [15] J. M. Ziman. *Electrons and phonons*. Clarendon Press, Oxford, 1962.
- [16] G. Grimvall. *The Electron-Phonon Interaction in Metals*. North-Holland, Amsterdam, 1981.
- [17] J. M. Ziman. *Principles of the theory of solids*. Cambridge University Press, London, 1964.
- [18] R. C. Albers, L. Bohlin, M. Roy, and J. W. Wilkins. *Phys. Rev. B*, 13:768, 1976.
- [19] W. Kohn. *Phys. Rev. Lett.*, 2:393, 1959.

- [20] W. L. McMillan. *Phys. Rev.*, 167:331, 1968.
- [21] P. B. Allen and R. C. Dynes. *Phys. Rev. B*, 12:905, 1975.
- [22] D. C. Wallace. *Statistical physics of crystals and liquids. A guide to highly accurate equations of state*. World Scientific, Singapore, 2002.
- [23] P. B. Allen and J. C. K. Hui. *Z. Physik B*, 37:33, 1980.
- [24] N. Bock, D. Coffey, and D. C. Wallace. *Phys. Rev. B*, 72:155120, 2005.
- [25] O. Delaire, M. S. Lucas, J. A. Muñoz, M. Kresch, and B. Fultz. *Phys. Rev. Lett.*, 101:105504, 2008.
- [26] O. Delaire, K. Marty, M. B. Stone, P. R. C. Kent, M. S. Lucas, D. L. Abernathy, D. Mandrus, and B. C. Sales. *Proc. Natl. Acad. Sci. U.S.A.* 108, 108:4725, 2011.
- [27] N. Majlis. *The quantum theory of magnetism*. World Scientific, Singapore, 2007.
- [28] M. van Schilfgaarde, I. A. Abrikosov, and B. Johansson. *Nature*, 400:46, 1999.
- [29] J. Crangle and G. M. Goodman. *Proc. R. Soc. London A*, 321:477, 1971.
- [30] J. Yin, M. Eisenbach, D. M. Nicholson, and A. Rusanu. *Phys. Rev. B*, 86:214423, 2012.
- [31] L. Mauger, J. E. Herriman, O. Hellman, S. J. Tracy, M. S. Lucas, J. A. Muñoz, Y. Xiao, J. Li, and B. Fultz. *Phys. Rev. B*, 95:024308, 2017.
- [32] M. H. G. Jacobs and R. Schmid-Fetzer. *Phys. Chem. Miner.*, 37:721, 2010.
- [33] F. Körmann, B. Grabowski, B. Dutta, T. Hickel, L. Mauger, B. Fultz, and J. Neugebauer. *Phys. Rev. Lett.*, 113:165503, 2014.
- [34] I. Stockem, A. Bergman, A. Glensk, T. Hickel, F. Körmann, B. Grabowski, J. Neugebauer, and B. Alling. *Phys. Rev. Lett.*, 121:125902, 2018.
- [35] I. M. Lifshitz. *Sov. Phys. JETP*, 11:1130, 1960.
- [36] Y. M. Blanter, M. I. Kaganov, A. V. Pantsulaya, and A. A. Varlamov. *Phys. Rep.*, 4:159, 1994.
- [37] E. Bruno, B. Ginatempo, E. S. Guiliano, A. V. Ruban, and Y. K. Vekilov. *Phys. Rep.*, 249:353, 1994.
- [38] V. G. Vaks and A. V. Trefilov. *J. Phys. F: Metal Phys.*, 18:213, 1988.
- [39] V. G. Vaks and A. V. Trefilov. *J. Phys. Condens. Matter*, 3:1389, 1991.

- [40] S. L. Bud'ko, A. N. Voronovskii, A. G. Gapotechenko, and E. S. Itskevich. *Sov. Phys. JETP*, 59:454, 1984.
- [41] A. F. Goncharov and V. V. Struzhkin. *Physica C: Superconductivity*, 385:117, 2003.
- [42] A. Polian, M. Gauthier, S. M. Souza, D. M. Trichês, J. C. de Lima, and T. A. Grandi. *Phys. Rev. B*, 83:113106, 2011.
- [43] Y. Wu, N. H. Jo, M. Ochi, L. Huang, D. Mou, S. L. Bud'ko, P. C. Canfield, N. Trivedi, R. Arita, and A. Kaminski. *Phys. Rev. Lett.*, 115:166602, 2015.
- [44] J. L. Murray. *Phase Diagrams of Binary Titanium Alloys*. ASM International, 1987.
- [45] H. Ohtani, N. Hanaya, M. Hasebe, S. I. Teraoka, and M. Abe. *CALPHAD: Comput. Coupling Phase Diagrams Thermochem.*, 30:147, 2006.
- [46] L.-F. Zhu, M. Friák, A. Dick, B. Grabowski, T. Hickel, F. Liot, D. Holec, A. Schlieter, U. Kühn, J. Eckert, Z. Ebrahimi, H. Emmerich, and J. Neugebauer. *Acta Mater.*, 60:1594, 2012.
- [47] M. V. Nevitt. *J. Appl. Phys.*, 31:155, 1960.
- [48] J. J. Reilly and R. H. Wiswall. *Inorg. Chem.*, 13:218, 1974.
- [49] B. Sakintuna, F. Lamari-Darkrim, and M. Hirscher. *Int. J. Hydrogen Energ.*, 32:1121, 2007.
- [50] L. Zaluski, A. Zaluska, P. Tessier, J. O. Ström-Olsen, and R. Schulz. *J. Alloys Compd.*, 227:53, 1995.
- [51] J. Das, K. B. Kim, F. Baier, W. Löser, and J. Eckert. *Appl. Phys. Lett.*, 87:161907, 2005.
- [52] J. Das, K. B. Kim, F. Baier, W. Löser, A. Gebert, and J. Eckert. *J. Alloys Compd.*, 434:28, 2007.
- [53] S. M. Shapiro, F. Reidinger, and J. R. Lynch. *J. Phys. F: Metal Phys.*, 12:1869, 1982.
- [54] U. Buchenau, H. R. Schober, J.-M. Welter, G. Arnold, and R. Wagner. *Phys. Rev. B*, 27:955, 1983.
- [55] J. Yamashita and S. Asano. *Prog. Theor. Phys.*, 48:2129, 1972.
- [56] D. A. Papaconstantopoulos. *Phys. Rev. B*, 11:4801, 1975.
- [57] L.-F. Zhu, M. Friák, A. Udyansky, D. Ma, A. Schlieter, U. Kühn, J. Eckert, and J. Neugebauer. *Intermetallics*, 45:11, 2014.

- [58] R. Eibler, J. Redinger, and A. Neckel. *J. Phys. F: Met. Phys.*, 17:1533, 1987.
- [59] J. Y. Rhee, B.N. Harmon, and D.W. Lynch. *Phys. Rev. B*, 54:17385, 1996.
- [60] A. Kellou, Z. Nabi, A. Tadjer, N. Amrane, N. Fenineche, and H. Aourag. *Phys. Stat. Sol. (b)*, 239:389, 2003.
- [61] P. E. Blöchl. *Phys. Rev. B*, 41:5414, 1990.
- [62] G. Kresse and D. Joubert. *Phys. Rev. B*, 59:1758, 1999.
- [63] J. P. Perdew, K. Burke, and M. Ernzerhof. *Phys. Rev. Lett*, 77:3865, 1996.
- [64] W. Kohn and L. J. Sham. *Phys. Rev.*, 140:A1133, 1965.
- [65] G. Kresse and J. Furthmüller. *Phys. Rev. B*, 54:11169, 1996.
- [66] G. Kresse and J. Furthmüller. *Comput. Mat. Sci.*, 6:15, 1996.
- [67] O. Hellman, P. Steneteg, I. A. Abrikosov, and S. I. Simak. *Phys. Rev. B*, 87:104111, 2013.
- [68] M. L. Klein and G. K. Horton. *J. Low Temp. Phys.*, 9:151, 1972.
- [69] D. J. Hooton. *Edinburgh Dublin Philos. Mag. J. Sci.*, 46:422, 1955.
- [70] A. A. Maradudin and A. E. Fein. *Phys. Rev.*, 128:2589, 1962.
- [71] J. Bardeen, L. N. Cooper, and J. R. Schrieffer. *Phys. Rev.*, 108:1175, 1957.
- [72] N. Bock, D. C. Wallace, and D. Coffey. *Phys. Rev. B*, 73:075114, 2006.
- [73] S. Baroni, S. de Gironcoli, A. Dal Corso, and P. Giannozzi. *Rev. Mod. Phys.*, 73:515, 2001.
- [74] P. Giannozzi *et al.* *J. Phys.: Condens. Matter*, 21:395502, 2009.
- [75] P. V. C. Medeiros, S. Stafström, and J. Björk. *Phys. Rev. B*, 89:041407, 2014.
- [76] P. V. C. Medeiros, S. S. Tsirkin, S. Stafström, and J. Björk. *Phys. Rev. B*, 91:041116, 2015.
- [77] V. Popescu and A. Zunger. *Phys. Rev. B*, 85:085201, 2012.
- [78] R. F. Hehemann and G. D. Sandrock. *Scr. Metall.*, 5:801, 1971.
- [79] X. Huang, C. Bungaro, V. Godlevsky, and K. M. Rabe. *Phys. Rev. B*, 65:014108, 2001.
- [80] W. Sturhahn. *Hyperfine Interact.*, 125:149, 2000.
- [81] D. L. Abernathy, M. B. Stone, M. J. Loguillo, M. S. Lucas, O. Delaire, X. Tang, J. Y. Y. Lin, and B. Fultz. *Rev. Sci. Instr.*, 83:015114, 2012.

- [82] B. Fultz, T. Kelley, J. Lin, J. Lee, O. Delaire, M. Kresch, M. McKeerns, and M. Aivazis. Experimental inelastic neutron scattering: Introduction to DANSE. <http://docs.danse.us/DrChops/ExperimentalInelasticNeutronScattering.pdf>, 2009.
- [83] M. S. Lucas, J. A. Muñoz, O. Delaire, N. Markovskiy, M. B. Stone, D. Abernathy, I. Halevy, L. Mauger, B. Keith, M. L. Winterrose, Yuming Xiao, M. Lerche, and B. Fultz. *Phys. Rev. B*, 82:144306, 2010.
- [84] J. A. Muñoz, M. S. Lucas, O. Delaire, M. L. Winterrose, L. Mauger, C. W. Li, A. O. Sheets, M. B. Stone, D. L. Abernathy, Y. Xiao, P. Chow, and B. Fultz. *Phys. Rev. Lett.*, 107:115501, 2011.
- [85] J. A. Muñoz, M. S. Lucas, L. Mauger, I. Halevy, J. Horwath, S. L. Semiatin, Y. Xiao, P. Chow, M. B. Stone, D. L. Abernathy, and B. Fultz. *Phys. Rev. B*, 87:014301, 2013.
- [86] J. A. Muñoz. *Electronic structure and phonon thermodynamics of iron alloys*. PhD thesis, California Institute of Technology, 2013.
- [87] H. J. Monkhorst and J. D. Pack. *Phys. Rev. B*, 13:5188, 1976.
- [88] K. Parlinski, Z. Q. Li, and Y. Kawazoe. *Phys. Rev. Lett.*, 78:4063, 1997.
- [89] A. Togo, F. Oba, and I. Tanaka. *Phys. Rev. B*, 78:134106, 2008.
- [90] D. Vanderbilt. *Phys. Rev. B*, 41:789, 1990.
- [91] S. Nosé. *J. Chem. Phys.*, 81:511, 1984.
- [92] P. B. Allen. Handbook of superconductivity. *Academic Press, New York*, page 478, 1999.
- [93] Y. Ding, R. Ahuja, J. Shu, P. Chow, W. Luo, and H. K. Mao. *Phys. Rev. Lett.*, 98:085502, 2007.
- [94] W. Luo, R. Ahuja, Y. Ding, and H. K. Mao. *Proc. Natl. Acad. Sci. U.S.A.*, 104:16428, 2007.
- [95] M. Ishizuka, M. Iketani, and S. Endo. *Phys. Rev. Lett.*, 61:R3823(R), 2000.
- [96] A. Landa, J. Klepeis, P. Söderlind, I. Naumov, O. Velikokhatnyi, L. Vitos, and A. Ruban. *J. Phys.: Condens. Matter*, 18:5079, 2006.
- [97] E. Walker. *Solid State Commun.*, 28:587, 1978.
- [98] P. D. Bogdanoff, B. Fultz, J. L. Robertson, and L. Crow. *Phys. Rev. B*, 65:014303, 2001.
- [99] F. Giustino. *Rev. Mod. Phys.*, 89:015003, 2017.

- [100] J.J. Zhou, O. Hellman, and M. Bernardi. *Phys. Rev. Lett.*, 121:226603, 2018.
- [101] F. C. Yang, J. A. Muñoz, O. Hellman, L. Mauger, M. S. Lucas, S. J. Tracy, M. B. Stone, D. L. Abernathy, Y. Xiao, and B. Fultz. *Phys. Rev. Lett.*, 117:076402, 2016.
- [102] O. Hellman, P. Steneteg, I. A. Abrikosov, and S. I. Simak. *Phys. Rev. B*, 87:104111, 2013.
- [103] O. Hellman and I. A. Abrikosov. *Phys. Rev. B*, 88:144301, 2013.
- [104] D. West and S. K. Estreicher. *Phys. Rev. Lett.*, 96:115504, 2006.
- [105] I. Errea, M. Calandra, and F. Mauri. *Phys. Rev. B*, 89:064302, 2014.
- [106] N. Shulumba, O. Hellman, and A. J. Minnich. *Phys. Rev. B*, 95:014302, 2017.
- [107] F. C. Yang, O. Hellman, M. S. Lucas, H. L. Smith, C. N. Saunders, Y. Xiao, P. Chow, and B. Fultz. *Phys. Rev. B*, 98:024301, 2018.
- [108] H. L. Smith, Y. Shen, D. S. Kim, F. C. Yang, C. P. Adams, C. W. Li, D. L. Abernathy, M. B. Stone, and B. Fultz. *Phys. Rev. Materials*, 2:103602, 2018.
- [109] J. E. Herriman, O. Hellman, and B. Fultz. *Phys. Rev. B*, 98:214105, 2018.
- [110] D. S. Kim, O. Hellman, J. Herriman, H. L. Smith, J. Y. Y. Lin, N. Shulumba, J. L. Niedziela, C. W. Li, D. L. Abernathy, and B. Fultz. *Proc. Natl. Acad. Sci. USA*, 115:1992, 2018.
- [111] N. Shulumba, O. Hellman, and A. J. Minnich. *Phys. Rev. Lett.*, 119:185901, 2017.
- [112] P. E. Blöchl. *Phys. Rev. B*, 50:17953, 1994.
- [113] R. A. Cowley. *Rev. Prog. Phys.*, 31:123, 1968.
- [114] Y.. Zhang and L.-W. Wang. *Phys. Rev. B*, 83:165208, 2011.
- [115] P. Giannozzi *et al.* *J. Phys.: Condens. Matter*, 29:465901, 2017.
- [116] R. Colella and B. W. Batterman. *Phys. Rev. B*, 1:3913, 1970.
- [117] A. Bosak, M. Hoesch, D. Antonangeli, D. L. Farber, I. Fischer, and M. Krisch. *Phys. Rev. B*, 78:020301(R), 2008.
- [118] P. B. Allen and V. Heine. *J. Phys. C*, 9:2305, 1976.
- [119] P. B. Allen and M. Cardona. *Phys. Rev. B*, 24:7479, 1981.
- [120] P. B. Allen and M. Cardona. *Phys. Rev. B*, 27:4760, 1983.

- [121] G. Antonius, S. Poncé, P. Boulanger, M. Côté, and X. Gonze. *Phys. Rev. Lett.*, 112:215501, 2014.
- [122] G. Antonius, S. Poncé, E. Lantagne-Hurtubise, G. Auclair, X. Gonze, and M. Côté. *Phys. Rev. B*, 92:085137, 2015.
- [123] S. Poncé, Y. Gillet, J. Laflamme Janssen, A. Marini, M. Verstraete, and X. Gonze. *J. Chem. Phys.*, 143:102813, 2015.
- [124] S. D. Brorson, A. Kazeroonian, J. S. Moodera, D. W. Face, T. K. Cheng, E. P. Ippen, M. S. Dresselhaus, and G. Dresselhaus. *Phys. Rev. Lett.*, 64:2172, 1990.
- [125] D. A. Papaconstantopoulos, L. L. Boyer, B. M. Klein, A. R. Williams, V. L. Moruzzi, and J. F. Janak. *Phys. Rev. B*, 15:4221, 1977.
- [126] L. L. Boyer, D. A. Papaconstantopoulos, and B. M. Klein. *Phys. Rev. B*, 15:3685, 1977.
- [127] J. M. Coombes and J. P. Carbotte. *Phys. Rev. B*, 34:4622, 1986.
- [128] A. Al-Lehaibi, J. C. Swihart, W. H. Butler, and F. J. Pinski. *Phys. Rev. B*, 36:4103, 1987.
- [129] J. Zasadzinski, D. M. Burnell, E. L. Wolf, and G. B. Arnold. *Phys. Rev. B*, 25:1622, 1982.
- [130] R. F. Hoyt and A. C. Mota. *Solid State Commun.*, 18:139, 1976.
- [131] P. D. Desai, T. K. Chu, H. M. James, and C. Y. Ho. *J. Phys. Chem. Ref. Data*, 13:1069, 1984.
- [132] P. D. Desai, H. M. James, and C. Y. Ho. *J. Phys. Chem. Ref. Data*, 13:1097, 1984.
- [133] G. W. Webb. *Phys. Rev.*, 181:1127, 1969.
- [134] J. M. Abraham and B. Devoit. *J. Less-Common Met.*, 29:311, 1972.
- [135] V. E. Peletskii. *Teplofiz. Vyz. Temp.*, 15:209, 1977.
- [136] K. D. Maglić, N. Lj. Perović, G. S. Vuković, and Lj. P. Zeković. *Int. J. Thermophys.*, 15:963, 1994.
- [137] F. Güthoff, B. Hennion, C. Herzig, W. Petry, H. R. Schober, and J. Trampenau. *J. Phys.: Condens. Matter*, 6:6211, 1994.
- [138] I. A. Abrikosov, A. V. Ponomareva, P. Steneteg, S. A. Barannikova, and B. Alling. *Curr. Opin. Solid State Mater. Sci.*, 20:85, 2016.
- [139] P. Steneteg, B. Alling, and I. A. Abrikosov. *Phys. Rev. B*, 85:144404, 2012.

- [140] N. Shulumba, B. Alling, O. Hellman, E. Mozafari, P. Steneteg, M. Odén, and I. A. Abrikosov. *Phys. Rev. B*, 89:174108, 2014.
- [141] F. Körmann, A. Dick, B. Grabowski, T. Hickel, and J. Neugebauer. *Phys. Rev. B*, 85:125104, 2012.
- [142] F. Körmann, A. A. H. Breidi, S. L. Dudarev, N. Dupin, G. Ghosh, T. Hickel, P. Korzhavyi, J. A. Muñoz, and I. Ohnuma. *Physica Status Solidi B*, 251:53, 2014.
- [143] Y. Ikeda, F. Körmann, B. Dutta, A. Carreras, A. Seko, J. Neugebauer, and I. Tanaka. *Npj Comput. Mater.*, 4:7, 2018.
- [144] V. P. Antropov, M. I. Katsnelson, M. vanSchilfgaarde, and B. N. Harmon. *Phys. Rev. Lett.*, 75:729, 1995.
- [145] V. P. Antropov, M. I. Katsnelson, B. N. Harmon, M. vanSchilfgaarde, and D. Kusnezov. *Phys. Rev. B*, 54:1019, 1996.
- [146] B. Skubic, J. Hellsvik, L. Nordström, and O. Eriksson. *J. Phys. Condens. Matter*, 20:315203, 2008.
- [147] T. Sohmura, R. Oshima, and F. E. Fujita. *Scr. Metall.*, 14:855, 1980.
- [148] M. Sugiyama, S. Harada, and R. Oshima. *Scr. Metall.*, 19:315, 1985.
- [149] Y. Tsunoda and R. Abe. *Phys. Rev. B*, 55:11507, 1997.
- [150] R. Abe, Y. Tsunoda, M. Nishi, and K. Kakurai. *J. Phys. Condens. Matter*, 10:L79, 1998.
- [151] B. Dutta, S. Bhandary, S. Ghosh, and B. Sanyal. *Phys. Rev. B*, 86:024419, 2012.
- [152] Y. O. Kvashnin, S. Khmelevskiy, J. Kudrnovský, A. N. Yaresko, L. Genovese, and P. Bruno. *Phys. Rev. B*, 86:174429, 2012.
- [153] A. Kussmann and K. Jessen. *J. Phys. Soc. Japan Suppl.*, 17B1:136, 1962.
- [154] G. Longworth. *Phys. Rev.*, 172:572, 1968.
- [155] M. L. Winterrose, M. S. Lucas, A. F. Yue, I. Halevy, L. Mauger, J. A. Muñoz, J. Hu, M. Lerche, and B. Fultz. *Phys. Rev. Lett.*, 102:237202, 2009.
- [156] M. L. Winterrose, L. Mauger, I. Halevy, A. F. Yue, M. S. Lucas, J. A. Muñoz, H. Tan, Y. Xiao, P. Chow, W. Sturhahn, T. S. Toellner, E. E. Alp, and B. Fultz. *Phys. Rev. B*, 83:134304, 2011.
- [157] A. Chumakov and W. Sturhahn. *Hyperfine Interact.*, 123-124:781, 1999.
- [158] W. Sturhahn and V. Kohn. *Hyperfine Interact.*, 123-124:367, 1999.

- [159] W. Sturhahn and J. M. Jackson. *Geophys. Soc. Am. Special Papers*, 421:157, 2007.
- [160] S. J. Pickart and R. Nathans. *J. Appl. Phys.*, 33:1336, 1962.
- [161] V. A. Tsurin and A. Z. Men'shikov. *Phys. Met. Metallogr.*, 45:82, 1978.
- [162] A. Z. Men'shikov and V. A. Tsurin. *Phys. Met. Metallogr.*, 47:68, 1979.
- [163] A. Zunger, S.-H. Wei, L. G. Ferreira, and J. Bernard. *Phys. Rev. Lett.*, 65:353, 1990.
- [164] B. Alling, T. Marten, and I. A. Abrikosov. *Phys. Rev. B*, 82:184430, 2010.
- [165] J. Hubbard. *Phys. Rev. B*, 19:2626, 1979.
- [166] J. Hubbard. *Phys. Rev. B*, 20:4584, 1979.
- [167] J. Hubbard. *Phys. Rev. B*, 23:5974, 1981.
- [168] H. Hasegawa. *J. Phys. Soc. Jpn.*, 46:1504, 1979.
- [169] H. Hasegawa. *J. Phys. Soc. Jpn.*, 49:178, 1980.
- [170] B. L. Gyorffy, A. J. Pindor, J. Staunton, G. M. Stocks, and H. Winter. *J. Phys. F: Met. Phys.*, 15:1337, 1985.
- [171] G. Inden. *Proceedings Project Meeting CALPHAD V*, pages 1–13, 1976.
- [172] M. D. Kuz'min. *Phys. Rev. Lett.*, 94:107204, 2005.
- [173] W. Sturhahn and E. Gerdau. *Phys. Rev. B*, 49:9285, 1994.
- [174] D. C. Wallace. *Thermodynamics of Crystals*. Dover Publications, Mineola, New York, 1998.
- [175] J. Jääskeläinen and E. Suoninen. *Phys. Status Solidi A*, 63:241, 1981.
- [176] W. G. Stirling, R. A. Cowley, and M. W. Stringfellow. *J. Phys. F: Met. Phys.*, 2:421, 1972.
- [177] O. Delaire, J. Ma, K. Marty, A. F. May, M. A. McGuire, M.-H. Du, D. J. Singh, A. Podlesnyak, G. Ehlers, M. D. Lumsden, and B. C. Sales. *Nat. Mater.*, 10:614, 2011.
- [178] C. W. Li, O. Hellman, J. Ma, A. F. May, H. B. Cao, X. Chen, A. D. Christianson, G. Ehlers, D. J. Singh, B. C. Sales, and O. Delaire. *Phys. Rev. Lett.*, 112:175501, 2014.
- [179] Y. Shen, C. W. Li, X. Tang, H. L. Smith, and B. Fultz. *Phys. Rev. B*, 93:214303, 2016.

- [180] A. P. Hammersley, S. O. Svensson, M. Hanfland, A. N. Fitch, and D Häusermann. *High Pressure Res.*, 14:235, 1996.
- [181] E. I. Isaev, S. I. Simak, I. A. Abrikosov, R. Ahuja, Yu. Kh. Vekilov, M. I. Katsnelson, A. I. Lichtenstein, and B. Johansson. *J. Appl. Phys.*, 101:123519, 2007.
- [182] A. N. Christensen, O. W. Dietrich, W. Kress, and W. D. Teuchert. *Phys. Rev. B*, 19:5699, 1979.
- [183] W. Kress, P. Roedhammer, H. Bilz, W. D. Teuchert, and A. N. Christensen. *Phys. Rev. B*, 17:111, 1978.
- [184] C. Li, N. K. Ravichandran, L. Lindsay, and D. Broido. *Phys. Rev. Lett.*, 121:175901, 2018.
- [185] X. Gonze *et al.* *Comp. Phys. Comm.*, 180:2582, 2009.
- [186] X. Gonze *et al.* *Computer Physics Communications*, 205:106, 2016.
- [187] F. Karsai, M. Engel, G. Kresse, and E. Flage-Larsen. *New J. Phys.*, 20:123008, 2018.
- [188] R. D. King-Smith, R. J. Needs, V. Heine, and M. J. Hodgson. *Europhys. Lett.*, 10:569, 1989.
- [189] S. Poncé, G. Antonius, Y. Gillet, P. Boulanger, J. Laflamme Janssen, A. Marini, M. Côté, and X. Gonze. *Phys. Rev. B*, 90:214304, 2014.
- [190] C. E. Patrick and F. Giustino. *Nat. Commun.*, 4:2006, 2013.
- [191] B. Monserrat. *Phys. Rev. B*, 93:014302, 2016.
- [192] M. Zacharias and F. Giustino. *Phys. Rev. B*, 94:075125, 2016.
- [193] J. H. Lloyd-Williams and B. Monserrat. *Phys. Rev. B*, 92:184301, 2015.
- [194] J. Trampenau, W. Petry, and C. Herzig. *Phys. Rev. B*, 47:3132, 1993.
- [195] M. G. Kresch. *Temperature Dependence of Phonons in Elemental Cubic Metals Studied by Inelastic Scattering of Neutrons and X-Rays*. PhD thesis, California Institute of Technology, 2009.
- [196] G. Grimvall, J. Häglund, and A. Fernández Guillermet. *Phys. Rev. B*, 47:15338(R), 1993.
- [197] I. W. Shepherd. *Phys. Lett. A*, 43:305, 1973.
- [198] X. Tong, X. Xu, B. Fultz, H. Zhang, T. A. Strobel, and D. Y. Kim. *Phys. Rev. B*, 95:094306, 2017.